

EVALUATION OF THE NON-SUPERCELL TORNADO PARAMETER FOR THE  
GREEN BAY, WISCONSIN TORNADO EVENT OF 07 AUGUST 2013

A Thesis Presented to the Faculty of the Graduate School at the University of Missouri

In Partial Fulfillment of the Requirements for the Degree Masters of Science

by

ADAM HIRSCH

Dr. Patrick Market, Thesis Advisor

December 2016

The undersigned, appointed by the dean of the Graduate School, have examined the  
thesis entitled

EVALUATION OF THE NON-SUPERCELL TORNADO PARAMETER FOR THE  
GREEN BAY, WISCONSIN TORNADO EVENT OF 07 AUGUST 2013

Presented by Adam Hirsch,  
a candidate for the degree of master of science,  
and hereby certify that, in their opinion, it is worthy of acceptance.

---

Professor Patrick Market

---

Associate Professor Neil Fox

---

Assistant Professor Bohumil Svoma

---

Associate Professor David Vaught

## ACKNOWLEDGEMENTS

I would first to like to extend my sincerest gratitude to the four atmospheric science professors, Dr. Market, Dr. Fox, Dr. Lupo, and Dr. Svoma for instructing and guiding me on literally everything meteorology related I know. Without all of them, I wouldn't be the meteorologist that I am today and words cannot express how much they all have shaped and influenced me. Specifically, I'd like to thank Dr. Market for taking me on and having endless patience to work with me over the years and providing the humor in my day when needed. I'd also like to thank Dr. Vaught for agreeing to be on my thesis committee. I also have the thank the past and current fellow graduate students and friends I've made here at Mizzou that have made my time here worthwhile. All of you have been the support system away from home that I needed.

Finally, I would like to thank my family for the support and love they have always shown me as I worked to pursue my goals. Without their encouragement, the things I have and will achieve would never be possible.

*“Nothing worthwhile was ever accomplished without the will to start, the enthusiasm to continue and, regardless of temporary obstacles, the persistence to complete.”*

*-Waite Phillips*

# Table of Contents

Acknowledgements.....	ii
List of Figures.....	v
List of Tables.....	viii
Abstract.....	x
Chapter 1 Introduction.....	1
1.1 Purpose.....	2
1.2 Objectives.....	4
Chapter 2 Literature Review.....	5
2.1 Bow Echo Development.....	5
2.2 Mesovortex Tornadoes.....	9
2.2.1 Observational and Modeling Studies.....	10
2.2.2 Mesovortex Development Theories.....	24
2.3 Non-Supercell Tornado Parameter.....	29
2.4 Ensemble Modeling.....	35
Chapter 3 Methodology.....	38
3.1 Event Selection.....	38
3.2 Data Selection and Processing for Case Analysis.....	38
3.3 Azimuthal Shear.....	40
3.4 WRF Model Structure.....	41
Chapter 4 Case Analysis.....	44
4.1 Synoptic and Mesoscale Forecast.....	44
4.2 Radar Analysis.....	54

Chapter 5 Results and Discussion.....	72
5.1 Subjective Evaluation of NSTP.....	72
5.2 Statistical Verification of NSTP.....	81
Chapter 6 Conclusions.....	88
6.1 Summary.....	88
6.2 Future Work.....	91
References.....	92

## Table of Figures

Figure 2.1.1 Schematic evolution of low level radar reflectivity structure in a bow shaped echo convective system. Taken from Fujita (1978).....	6
Figure 2.1.2 Conceptual model of a squall line with trailing stratiform area viewed in a cross section oriented perpendicular to the convective line. Taken from Smull and Houze (1987).....	6
Figure 2.1.3. Stage four of the evolution of an idealized bow echo. A new steady state is achieved where the cold pool is balanced with the ambient vertical wind shear and elevated rear inflow jet. Taken from Weisman 1993.....	9
Figure 2.2.1 Schematic model of the life cycle of a non-supercell tornado. Taken from Wakimoto and Wilson (1989).....	11
Figure 2.2.2. Rotational cyclonic circulation (Circ) tracks identified for each bowing line segment (storm). Black dots along the tracks represent 5–6-min interval circulation locations with beginning and ending times (in UTC) indicated. The 100-km (54 nmi) range ring from the KLVX WSR-88D (+ sign) is shown. Taken from Funk et al. (1999).....	14
Figure 2.2.3 Composite vertical profiles of $V_r$ for all tornadic (solid line) and nontornadic (dashed line) mesovortices. Error bars represent 1 std dev for all data points at the respective level. Taken from Atkins et al. (2004).....	19
Figure 2.2.4. Diagram for mesovortex genesis with horizontal crosswise vorticity. Taken from Trapp and Weisman (2003).....	26
Figure 2.2.5. Diagram of mesovortex couplet diagram. Taken from Wakimoto et al. (2006).....	27
Figure 2.2.6. Schematic of cyclonic only mesovortex genesis. Taken from Atkins and Laurent (2009b).....	28
Figure 2.3.1. Composite example by Davies (2003) depicting a typical setting that can support nonmesocyclone tornadoes. Red dots denote surface heating axis of steep lapse rates and the area enclosed in green denotes 0-3 km MLCAPE $> 40 \text{ J kg}^{-1}$ . Taken from Caruso and Davies (2005).....	32
Figure 2.3.2. 1800 UTC 16 June 2004 LAPS NST image (red 1-2, magenta $>2$ ). Solid white line indicates the stationary boundary at 1800 UTC and “X” indicates NST maxima not associated with a linear boundary. Taken from Baumgardt and Cook (2006).....	35

Figure 3.1. Map projection domain of the unnested 13-km WRF Model Run used with the center point denoted.....	42
Figure 4.1 Surface map of CONUS from 07 August 2013 for 0000 UTC.....	45
Figure 4.2a. Radar image of the northern plains on 06 August 2013 at 2353 UTC.....	46
Figure 4.2b. Radar image of the northern plains on 07 August 2013 at 0223 UTC.....	46
Figure 4.2c. Radar image of the northern plains on 07 August 2013 at 0456 UTC.....	47
Figure 4.3. 850 hPa analysis at 0000 UTC on 07 August 2013. Green lines are pressure (hPa), red solid/dashed lines are positive/negative omega ( $\mu\text{b s}^{-1}$ ), and blue lines are 850 hPa relative humidity with values over 70% shaded in green .....	48
Figure 4.4. 500 hPa map at 0000 UTC on 07 August 2013. Plotted is pressure (hPa) in green, wind (knots) is plotted in yellow, and absolute vorticity is shaded in green and blue.....	49
Figure 4.5. 200 hPa upper air map at 0000 UTC on 07 August 2013. Depicted is pressure (red line), divergence in yellow ( $10^{-5} \text{ s}^{-1}$ ), and isotachs (knots).....	49
Figure 4.6. Observed radiosonde from KGRB at 0000 UTC on 07 August 2013.....	51
Figure 4.7. Non-Supercell tornado parameter over the KGRB at 0500 UTC on 7 August 2013. a. CAPE (top left) b. Lapse Rate (top right) c. CIN (middle left) d. Shear (middle right) e. Vorticity (bottom left) f. NSTP composite value (bottom right).....	53
Figure 4.8. Composite of tornadic tracks from 07 August 2013. Taken from Green Bay WFO event page.....	55
Figure 4.9. KGRB scan at 0.5° radar scan at 0522 UTC on 07 August 2013. Circled areas are tornado locations. Top left a.) Radar reflectivity. Top right b.) Storm Relative Velocity. Bottom left c.) Correlation coefficient. Bottom right d.) Differential Reflectivity.....	55
Figure 4.10. Same as Figure 4.9 but at 0527 UTC on 07 August 2013.....	58
Figure 4.11. Same as Figure 4.9 but at 0531 UTC on 07 August 2013.....	58
Figure 4.12. Convergence from KGRB at 0532 UTC on 07 August 2013 at 0.5° tilt. The circle area is the tornadic location.....	60
Figure 4.13. Azimuthal Shear from KGRB at 0532 UTC at 07 August 2013 at 0.5° tilt. The circle area is the tornadic location.....	61
Figure 4.14. Same as Figure 4.9 but at 0541 UTC on 07 August 2013.....	63

Figure 4.15. Same as Figure 4.13 but at 0541 UTC on 07 August 2013.....	63
Figure 4.16. Same as Figure 4.9 but at 0546 UTC on 07 August 2013.....	64
Figure 4.17. Same as Figure 4.13 but at 0546 UTC on 07 August 2013.....	64
Figure 4.18. Same as Figure 4.9 but at 0550 UTC on 07 August 2013.....	66
Figure 4.19. Same as Figure 4.13 but at 0550 UTC on 07 August 2013.....	66
Figure 4.20. Same as Figure 4.9 but at 0559 UTC on 07 August 2013.....	68
Figure 4.21. Same as Figure 4.13 but at 0600 UTC on 07 August 2013.....	68
Figure 4.22. Same as Figure 4.9 but at 0604 UTC on 07 August 2013.....	70
Figure 4.23. Same as Figure 4.13 but at 0604 UTC on 07 August 2013.....	70
Figure 4.24. Same as Figure 4.9 but at 0609 UTC on 07 August 2013.....	71
Figure 4.25. Same as Figure 4.13 but at 0609 UTC on 07 August 2013.....	71
Figure 5.1. Ensemble of WRF output model solutions at 16 hours out from the model run initialized on 06 August 2013 at 1200 UTC, which relates to 07 August 2013 at 0400 UTC. Values of 0.5 NSTP are contoured. The cumulus parameterization scheme are broken down as followed: red is Kain-Fritsch scheme, green is Betts-Miller-Janjic scheme, blue is Simplified Arakawa-Schubert scheme, and brown is Grell 3d scheme. The microphysical schemes are: solid line is Lin scheme, short dash is WRF Single Moment 5 Class, medium dashed are Ferrier scheme, a long dash and 3 short dashes is WRF Single Moment 6 Class scheme, long dash dot is the Goddard scheme, and long dash three dots is Milbrandt and Yau scheme.....	74
Figure 5.2. Same as 5.1 but at 17 hours out from the model run initialized on 06 August 2013 at 1200 UTC.....	75
Figure 5.3. Same as 5.1 but at 18 hours out from the model run initialized on 06 August 2013 at 1200 UTC.....	77
Figure 5.4. WRF output for the Betts-Miller-Janjic cumulus parameterization scheme and Goddard combination at 16 hours from the model run on 06 August 2013 at 1200 UTC, which relates to 07 August 2013 at 0400 UTC with NSTP values of 0.5 contoured. This is an example of a hit for one model solution.....	80
Figure 5.5. WRF output for the Betts-Miller-Janjic cumulus parameterization scheme and WRF Single Moment 6 Class microphysical scheme combination at 16 hours from the model run on 06 August 2013 at 1200 UTC, which relates to 07 August 2013 at 0600 UTC with NSTP values of 0.5 contoured. This is an example of a miss for one model solution. ....	81

## List of Tables

Table 3.1. Layout of the combination of model configurations used with cumulus parameterization schemes on the left and microphysical schemes on top with the associated model run number in the center. The microphysical schemes are denoted with superscripts for brevity and are as follows: a is the Lin et al. scheme, b is the WRF Single Moment 5 Class scheme, c is the Ferrier (Eta) scheme, d is the WRF Single Moment 6 Class scheme, e is the Goddard Scheme, and f is the Milbrandt-Yau Double Moment 7 Class scheme.....	43
Table 5.1. Total number of hits and misses from 15 hours out to 20 hour from the 1200 UTC 06 August 2013.....	81
Table 5.2a. Kain Fritsch cumulus scheme results categorized into the 6 microphysical schemes at 0400 UTC on 07 August 2013 from the 1200 UTC 06 August 2013 model run 16 hours out.....	82
Table 5.2b. Betts-Miller-Janjic cumulus scheme results categorized into the 6 microphysical schemes at 0400 UTC on 07 August 2013 from the 1200 UTC 06 August 2013 model run 16 hours out.....	82
Table 5.2c. Simplified Arakawa-Schubert cumulus scheme results categorized into the 6 microphysical schemes at 0400 UTC on 07 August 2013 from the 1200 UTC 06 August 2013 model run 16 hours out.....	82
Table 5.2d. Grell 3D cumulus scheme results categorized into the 6 microphysical schemes at 0400 UTC on 07 August 2013 from the 1200 UTC 06 August 2013 model run 16 hours out.....	82
Table 5.3a. Kain Fritsch cumulus scheme results categorized into the 6 microphysical schemes at 0500 UTC on 07 August 2013 from the 1200 UTC 06 August 2013 model run 17 hours out.....	84
Table 5.3b. Betts-Miller-Janjic cumulus scheme results categorized into the 6 microphysical schemes at 0500 UTC on 07 August 2013 from the 1200 UTC 06 August 2013 model run 17 hours out.....	84
Table 5.3c. Simplified Arakawa-Schubert cumulus scheme results categorized into the 6 microphysical schemes at 0500 UTC on 07 August 2013 from the 1200 UTC 06 August 2013 model run 17 hours out.....	84
Table 5.3d. Grell 3D cumulus scheme results categorized into the 6 microphysical schemes at 0500 UTC on 07 August 2013 from the 1200 UTC 06 August 2013 model run 17 hours out.....	84

Table 5.4a. Kain Fritsch cumulus scheme results categorized into the 6 microphysical schemes at 0600 UTC on 07 August 2013 from the 1200 UTC 06 August 2013 model run 18 hours out.....	86
Table 5.4b. Betts-Miller-Janjic cumulus scheme results categorized into the 6 microphysical schemes at 0600 UTC on 07 August 2013 from the 1200 UTC 06 August 2013 model run 18 hours out.....	86
Table 5.4c. Simplified Arakawa cumulus scheme results categorized into the 6 microphysical schemes at 0600 UTC on 07 August 2013 from the 1200 UTC 06 August 2013 model run 18 hours out.....	86
Table 5.4d. Grell 3D cumulus scheme results categorized into the 6 microphysical schemes at 0600 UTC on 07 August 2013 from the 1200 UTC 06 August 2013 model run 18 hours out.....	86

## **Abstract**

The difficulty of detecting and forecasting the development of non-supercell tornadoes (NST) is well documented. The rapid, low level development of NSTs decreases the warning time as they often develop in minutes and can last only a short amount of time. Even though most NSTs are relatively weak, EF0-EF2, they still cause damage. Research for non-supercell tornadoes has been focused on the amount of CAPE, CIN, shear, vorticity, and low-level lapse of non-supercell tornadoes. These five variables were compiled into the Non-Supercell Tornado Parameter (NSTP) by Baumgardt and Cook (2006) and is currently in use by the Storm Prediction Center.

The research presented focused on the evaluation of this parameter using 24 different experimental runs of the Weather and Research Forecasting (WRF) model. Here, a case study of an event on 07 August 2013 that passed through the Green Bay, WI area, between 0400 UTC and 0600 UTC which produced 6 NSTs was conducted. The predictability of the event was analyzed by using different WRF simulations with varying cumulus parameterizations and microphysical schemes at a 13-km scale. A detailed synoptic and radar analysis was conducted to further increase the understanding of NST environments and radar features. The research found that the 0000 UTC RUC initial fields could accurately forecast the tornadic event. In addition, dual-polarization radar products were used to aid in NST detection. The WRF model solutions highlighted areas of potential NST development that matched the RUC initial field when using an ensemble model approach while statistical results showed little skill. NSTs are difficult to forecast and the results here show that the NSTP can aid in situational awareness for forecasters when looking at ensemble model output.

## Chapter 1

Meteorologists strive to have the most accurate predictions possible, but despite their best efforts, forecasting can prove challenging. In addition, when dealing with severe weather, the National Weather Service (NWS) uses reports from citizens to verify events, so if an event occurs in the evening time, severe weather can be missed. One event that was a difficult forecast was a bow echo that moved through the Green Bay, WI area on 06-07 August 2013. This event produced 6 tornadoes, numerous damaging wind reports, and left various amounts of damage around the state. The tornadoes that form during these types of events are relatively weak but develop rapidly and last only a short amount of time. Various methods have been developed to try to understand and forecast these types of tornadoes.

The term “bow echo” was coined by Fujita in 1978. At the time, Fujita (1978) introduced the concept of the area of strongest winds occurring in the apex of the bowing segment. Research by Smull and Houze (1987) detailed the existence of the rear-inflow jet and found that stronger rear-inflow jets tended to be associated with stronger systems. Weisman and Trapp (2003) concluded that the damage created was not only associated with winds, but with tornadoes as well. Trapp et al. (2005) further expounded upon this research by concluding that 18% of all tornadoes were produced by Quasi-Linear Convective Systems (QLCS). This meant that some of the damage that was originally associated with winds in the past, could have been due to tornadoes associated with the systems.

The tornadoes often associated with QLCSs are non-mesocyclone or non-supercell tornadoes (Wakimoto and Wilson 1989). The development of these tornadoes

is different than supercell tornadoes and they are typically weaker, but can still be powerful under certain circumstances (Trapp and Weisman 2003; Atkins and Laurent 2009a). Non-mesocyclone tornadoes evolve due to the low-level circulations associated with shear instability (Wakimoto and Wilson 1989; Weisman and Trapp 2003). With these tornadic circulations near the surface, they can be hard to detect far away from the radar (Trapp et al. 2005).

The ability to accurately forecast for tornadic development in any case is something that to this day meteorologists still struggle with. There are many tools and parameters at the disposal of a forecaster to help further diagnose, evaluate, and forecast. One of the newer forecasting parameters in use by the Storm Prediction Center (SPC) is the Non-Supercell Tornadic Parameter (NSTP) developed by Baumgardt and Cook (2006). The NSTP helps guide the forecaster to areas of potential development of non-supercell tornadoes. The extensive length of a QLCS can make it difficult to pinpoint favorable areas for development. The NST parameter looks at lapse rate, Convective Available Potential Energy (CAPE), vorticity, shear, and Convective Inhibition (CIN), basic ingredients of severe weather (Baumgardt and Cook 2006). The NST is relatively new and does not have much research supporting it, but with its use at SPC, it carries some forecasting merit.

## **1.1 Purpose**

The purpose of this research is to help gain a deeper understanding of non-mesocyclone tornadoes and provide guidance on the NST parameter developed by Baumgardt and Cook (2006) to potentially aid in mesoscale forecasting. The NST

parameter and the usefulness it provides will be evaluated through a two-step process. The first process will be to take a tornadic case that has an embedded non-mesocyclone structure and analyze the environment and evolution of the system. A case study was done in the Green Bay area for a QLCS that moved through during the overnight hours of 06-07 August, 2013. This event produced multiple non-mesocyclone tornadoes across the region. The fact that the event occurred overnight is another problem. Tornadoes tend to occur more often during the night, and with greater frequency when associated with QLCSs, than any other weather system (Trapp et al. 2005). Nighttime tornadoes also account for 40% of all tornado-related casualties (Kis and Straka 2010). The issue of effective communication is a goal in the meteorological community and by giving citizens knowledge beforehand, forecasters can do a better job of warning people in advance. Using applicable forecasting techniques and radar analysis, the full extent of the case will be explored.

Being able to forecast in advance is part two of the research presented. To evaluate the NST parameter, several different cumulus and microphysical schemes were run in the Weather and Research Forecasting model (WRF). Through the analysis of the ensemble of model runs, we will be able to compare and also determine the effectiveness of the parameter for predicting non-mesocyclone tornadoes and determine which configuration might be best used for forecasting in the scheme in the WRF to best represent the real case.

## 1.2 Objectives

To achieve the purpose previously mentioned, the following objectives were identified and carried out:

- Analyze the environment associated with the system using archived online data and evaluate the forecast in meteorological software using model output to see what the models predicted and understand why the forecast evolved the way it did.
- Obtain radar data for the event from the Green Bay WFO allowing for a detailed analysis of the evolution of the QLCS using reflectivity, velocity, and other Dual-Pol products.
- Run a WRF model simulation with different cumulus parameterizations and different microphysics schemes to create an ensemble model approach. From there, determine the skill of the models in the prediction of the NSTs.

## **Chapter 2 Literature Review**

To establish a deep understanding of the research presented here on nonsupercell tornadoes, an extensive literature review was conducted. The literature review is broken up into four sections. Section 2.1 is about bow echo and mesoscale convective system (MCS) development, which addresses the environment that nonsupercell tornadoes occur. Section 2.2 looks at nonsupercell tornadoes in both an observational and modeling approach. A subsection of section 2.2 looks at the theories that currently exist for mesovortex development. Section 2.3 is a detailed look at the nonsupercell tornado parameter and the research conducted on it. Section 2.4 is an overview of ensemble modeling and how it has continued to grow in the meteorological community.

### **Section 2.1 Bow Echo Development**

The evolution, structure, and movement of bow echoes is well documented. Fujita (1978) was the first to identify and show the evolution of a bow echo. The general structure and evolution of a bow echo is shown in Fig 2.1.1. A bow echo is typically oriented north-south with a comma head or bookend vortex at one or both ends and a bowing center (Smull and Houze 1987; Rotunno et al. 1988; Weisman 1992; Weisman 1993). The different stages in Figure 2.1.1 show the center of the downburst (DB) in every time step. This area is where the strongest winds often occur and where tornadogenesis is possible. The structure of a line-type MCS is shown in Figure 2.1.2. Figure 2.1.2 shows an area of strong reflectivity along the leading edge with a broader, weaker transition zone behind the leading edge. The leading meso-low and trailing

**Figure 2.1.1. Schematic evolution of low level radar reflectivity structure in a bow shaped echo convective system. Taken from Fujita (1978).**

**Figure 2.1.2. Conceptual model of a squall line with trailing stratiform area viewed in a cross section oriented perpendicular to the convective line. Taken from Smull and Houze (1987).**

meso-high encourage convection where the two air flow patterns meet, helping to sustain and regenerate the system (Smull and Houze 1987). The system is sustained by having the cold surface outflow of an old cell lift the environmental boundary-layer air to its level of free convection (LFC) which is enhanced by low level shear (Rotunno et al. 1988). Rotunno et al. (1988) concluded that the cold pool interacts with shear and helps maintain the development of the system.

Figure 2.1.2 also depicts the movements of the environmental wind as being from front-to-rear. However, the figure also depicts a rear-to-front inflow. This rear inflow is

known as the rear-inflow jet (RIJ). The development of the rear inflow is first proposed by Rotunno et al. (1988), known as the Rotunno-Klemp-Weisman theory (RKW), but the idea was furthered by Weisman (1992; 1993). The RIJ development is based on the balance that the cold pool has with the system itself. This balance is expressed in equation 1 from Weisman (1992):

$$C^2 = 2 \int_0^H (-B) dz \quad (1)$$

where C is the strength of the cold pool, H is the depth of the cold pool, and B represents the buoyancy which is defined by

$$B \equiv g \left[ \frac{\theta'}{\theta} + 0.61(q_v - \overline{q_v}) - q_c - q_r \right] \quad (2)$$

and where  $\theta$  is the potential temperature,  $q_v$  is the mixing ratio of water vapor,  $q_c$  is cloud water mixing ratio, and  $q_r$  is the rainwater. Whenever  $C < 1$ , the vertical shear overwhelms the cold pool circulations causing the system to tilt downstream, inhibiting development until maturity (Weisman 1992). When  $C > 1$ , the system tilts upshear, cutting off the systems flow by allowing the RIJ to descend towards the surface, ceasing upward motion (Weisman 1992). The longevity of the bow echo is maintained when C is close to 1 as it allows storms to remain upright as the buoyancy, cold pool, and shear are all in balance (Weisman 1992).

Figure 2.1.3 shows the mature stage of a bow echo and the associated rear inflow jet. In the figure, the ambient shear, cold pool, and buoyancy are all in balance with one another and the system can continue moving for an additional six hours (Weisman 1993). The buoyancy in the system is the amount of Convective Available Potential Energy

(CAPE) present in the atmosphere. Since the amount of CAPE controls the potential temperature excess that is within a parcel of rising air, a value of CAPE above  $1700 \text{ J kg}^{-1}$  can generate enough lift to maintain the bow echo (Weisman 1993). The rear inflow jet is analyzed with the horizontal vorticity equation (3) for inviscid Boussinesq flow:

$$\frac{d\eta}{dt} = -\frac{\partial B}{\partial x} \quad (3)$$

where

$$\eta = \frac{\partial u}{\partial z} - \frac{\partial w}{\partial x} \quad (4)$$

where B is buoyancy. This equation accounts for the horizontal gradients of buoyancy by allowing it to develop from the buoyancy field (Weisman 1993).

The maximum amount of development as shown by Weisman (1993) comes during the 120 to 180-minute period from the start of the in the model simulations. During this time, the winds grew from  $5 \text{ m s}^{-1}$  to  $20 \text{ m s}^{-1}$ . After the 180-minute mark, if the systems do not maintain balance as described in the RKW theory, due to upshear tilting or an advancing cold pool, the system collapses on itself. However, the cold pool is not the only thing that contributes to the development and maintenance of the bow echo. The existence of a bookend vortex can contribute upwards of 50% of the strength of the observed rear-inflow jet (Weisman 1993). With a cyclonic flow at the comma head, as seen in Figure 2.1.1, the wind is maximized at the bowing section of the system. This can be enhanced even further if there is a southern vortex as well but a northern comma head is more common and better documented (Weisman 1993). When the system has especially strong winds, a rear inflow notch can be present. The notch occurs on the back side of the leading edge where the stratiform precipitation occurs and appears as a slight backwards V shape on radar where there is a decrease in reflectivity (Przybylinski

**Figure 2.1.3. Stage four of the evolution of an idealized bow echo. A new steady state is achieved where the cold pool is balanced with the ambient vertical wind shear and elevated rear inflow jet. Taken from Weisman (1993).**

1995). This is due to dry air being brought in on the back side, reducing entrainment, allowing for maximum wind speeds. The faster wind speeds can also be seen on radar velocity images as they will appear faster than the surrounding air and typically occur at the apex of the bowing segment (Przybylinski 1995). In addition to the enhanced vorticity at this region, the wind helps generate a faster rotating column of air which can affect mesocyclone development (Wakimoto and Wilson 1989).

## **Section 2.2 Mesovortex Tornadoes**

A complete understanding of mesovortices and their development is needed to fully understand the research presented here. The following section is divided into the following two aspects of mesovortices: observational and modeling studies, and development theories.

## 2.2.1 Observational and Modeling Studies

### *a. Observational Studies*

Wakimoto and Wilson (1989) were among the first to explore in detail the development of non-supercell tornadoes. The focus area of the research was near the Denver Convergence Zone, where these types of tornadoes occur frequently. Wakimoto and Wilson (1989) found 27 vortices that were not associated with supercells during the Convection Initiation and Downburst Experiment (CINDE) through the analysis of photographs and radar data. Their research concluded that, by looking at the lowest two kilometers in the radar scan, if the development location was no further than 40 km away from the radar site, then these types of tornadoes could be detected. At maximum strength, the reflectivity and velocity signature was reminiscent of a supercell tornado.

Overall, Wakimoto and Wilson (1989) managed to find differences between non-supercell tornadoes and supercell tornadoes and proposed a development theory. The average environment that Wakimoto and Wilson (1989) found contained low to moderate instability associated with weak wind shear. Further studies would give a better understanding of the environment necessary over the other parts of the country away from the Denver Convergence Zone that is more widely applicable. In addition to the environment, Wakimoto and Wilson (1989) also found that there were often boundary convergences that aided in the development of these tornadoes. The development, as hypothesized by Wakimoto and Wilson (1989), is depicted in Fig. 2.2.1. The horizontal shear on a convergence boundary creates areas of instability while clouds grow from the uplift. Eventually, the clouds move over one of the propagating areas of instability and, due to vortex stretching, develop into a tornado, as seen in vortex C.

**Figure 2.2.1. Schematic model of the life cycle of a non-supercell tornado. Taken from Wakimoto and Wilson (1989).**

With the use of the Weather Surveillance Radar 88 Doppler (WSR-88D), the detection of mesovortices has increased. Przybylinski (1995) used the radar technology and prior research to show how these events could be detected. Upon summarizing what observation and modeled research had been conducted prior to that time, Przybylinski (1995) presented two case studies. One event produced strong winds and hail while the other event produced wind, hail, and F1 damage. In both cases, the rear-inflow notch was present at the apex of the bowing segment, however, for the second case, the event was a type 3 bow echo, according to Johns and Hirt (1987). This type of bow echo often displays supercell characteristics at the bowing segment, has a pronounced bowing segment, a strong reflectivity gradient along the leading edge, and has a single rear inflow notch. The environment of case two that Przybylinski (1995) analyzed had CAPE values in excess of  $2100 \text{ J kg}^{-1}$  at Huron, South Dakota, but had values around  $3400 \text{ J kg}^{-1}$  in Bismarck, North Dakota. In addition, the sounding from both locations had weak wind shear associated indicating that supercells most likely would not develop. The bowing system had a 20-minute time frame during which multiple nonsupercell tornadoes occurred along with strong wind damage. The rapid development and appearance of these nonsupercell tornadoes is similar to what Wakimoto and Wilson (1989) found.

Przybylinski (1995) hypothesized that it was along the leading edge on the northern bowing apex that mesovortices formed, with the RIJ enhancing the strength of the convection along the leading edge. Przybylinski's (1995) analysis in this case showed how radars and previous knowledge would help forecasters in establishing an understanding of predictability and radar signatures of nonsupercell tornadoes.

Trapp et al. (1999) investigated the detectability of tornadic vortex signatures (TVS) using the WSR-88D. Trapp et al. (1999) evaluated 52 events from different locations and environments to establish if a tornado was a descending or nondescending tornado. Of the 52 events analyzed, 45 were supercells, while seven were associated with a QLCS. Typically, a descending tornado can be detected in radar scan altitudes between 2-7 km with strong rotational winds and with the maximum peak around 5-km, while a nondescending tornado signature only extends up to 3-km and has either little wind shear or has unidirectional shear. Using this information, a tornadic signature was classified as descending if the shear was greater than  $2.25 \text{ m s}^{-1} \text{ km}^{-1}$  and peak volume scan altitude was greater than 3 km.

Overall, Trapp et al. (1999) found in their study that only 52% of the TVS had a descending signature. In addition, the height of these storms was slightly above the threshold peak altitude for the volume scan, 3.4 km. There were often about five volume scans that detected the TVS before tornadogenesis occurred, leaving enough time for detection and a warning. When compared to the nondescending TVS, the velocity is weaker, the height of the peaks is much lower, and the number of value scans is also fewer. For the nondescending TVS on a QLCS, the typical number of scans completed was only one with a height of the peak at 1-km. This indicates low detectability as the

development is rapid and close to the surface, as hypothesized in Wakimoto and Wilson (1989). When looking at the seven QLCS cases individually, only one had a descending TVS. These findings support the idea that the TVS algorithms in a QLCS have little utility. In addition, Trapp et al. (1999) stresses that just because a TVS is nondescending does not indicate that it is experiencing nonsupercell tornadogenesis. Not only does this relate to findings in the QLCS data, but also to supercell systems analyzed, since nearly half of the events analyzed had a nondescending TVS yet still produced a tornado.

The frequent activity and difficulty in forecasting QLCS is documented in Funk et al. (1999) where the authors gave a detailed case analysis of a complex squall line that produced multiple tornadoes and swaths of wind damage. The event analyzed was a serial bow echo that developed in an atmosphere with moderate instability ( $2400 \text{ J kg}^{-1}$ ) and two overlying jet streaks at 300 hPa ahead of a moisture rich area over central Kentucky. By the time the system reached the area of interest (1400 UTC), the squall line had grown into a sizeable event with seven trackable bowing segments. In each of these bowing segments, there was an identifiable cyclonic vortex. However, only three of the vortices of the seven segments produced a tornado while the other four were associated with straight line wind damage at the apex of the bow. In the three storms that did produce tornadoes, there were multiple tornadoes produced and damage ranged from F0-F2. These were storm 1, 2, and 3 in Figure 2.2.2. As established in prior research, the tornadoes occurred near or around the apex of the bowing segments.

**Figure 2.2.2. Rotational cyclonic circulation (Circ) tracks identified for each bowing line segment (storm). Black dots along the tracks represent 5–6-min interval circulation locations with beginning and ending times (in UTC) indicated. The 100-km (54 nmi) range ring from the KLVX WSR-88D (+ sign) is shown. Taken from Funk et al. (1999).**

Of the three stronger circulations that were analyzed by Funk et al. (1999), one circulation stood out in particular. During a roughly two-hour time frame, storm 1 produced a total of seven circulations and exhibited different storm characteristics. For the first four circulations, it produced features typically seen on a QLCS. The first two circulations of storm 1 produced tornadoes and developed north of the bowing apex with strong rotational velocity values ( $\sim 23 \text{ m s}^{-1}$ ). It was at this peak velocity values that the strongest damage occurred and both of these tornadic cells were identifiable at low levels on the radar. Circulations 3 and 4 on storm 1 were along a low-level cyclonic convergence zone on the apex. These two circulations were much broader in their radar signatures. The existence of these multiple circulations, as noted by Funk et al. (1999), is due to the idea that there is convergence among the RIJ and the inflow ahead of the storm. Where these opposite flows meet, there is vertical stretching in the updraft,

allowing for vortex development. The size and strength of the event could support multiple vortices, even with a small distance between the circulations. These multiple circulations that existed during this time frame had a shorter duration than Circulation 1.

Circulation 5 on storm 1 at 1526 UTC started to transition to a cell that exhibited high-precipitation (HP) supercell characteristics. These characteristics were identifiable due to the rotating updraft detectable at multiple higher radar scans. In addition, the precipitation had been shifted to right over the strongest velocity rotation. The higher elevation scans also depicted a weak echo region, something normally seen in supercells. The vortex managed to extend up to 7-km and produced a tornado of F1 damage rating. These findings show that within a bow echo, typical supercell characteristics can be identified.

Once the system evolved past HP supercell characteristics, it transitioned to a standard rotating comma-head bow echo. During this phase, Circulations 6 and 7 occurred from storm 1. These circulations did not produce a tornado but did produce areas of strong wind damage. In the analysis of the data, Funk et al. (1999) found that these areas of strong wind were collocated along the bowing apex. The two circulations of note here were much broader compared to the prior ones in the same storm system. In addition, they were much weaker in terms of circulation at the higher elevation scans. This rotation aloft was weaker and broader at the lower scans as well, indicating that the strength had decreased throughout its depth. Both issues could be related to the radar sampling issues that Funk et al. (1999) ran into during the analysis. However, the radar did depict a RIJ associated with the strong winds. Storm 1 was a complex multicellular event that showed the stages that a bow echo could potentially go through. While Funk

et al. (1999) studied other storms, as seen in Figure 2.2.2, they were not as analyzed as thoroughly and confirmed what prior research had shown regarding multicellular bow echo storms.

Atkins et al. (2004) built upon the work that Funk et al. (1999) put forth, but also found the detectability and general life cycle over which tornadic and non-tornadic structures exhibited. Atkins et al. (2004) conducted their research on a bow echo that produced 13 mesovortices with seven circulations producing F0-F1 rated damage through the Davenport, Iowa and Lincoln, Illinois WFOs. The synoptic environment that the system evolved from was one that was consistent with a “progressive” derecho environment (Pryzbylinski 1995). There was strong southerly flow that allowed for plenty of warm air advection (WAA) and moisture to be along the leading edge of the front, which became the initiation point for the cells. The Skew-T from Lincoln, IL showed strong CAPE ( $3698 \text{ J kg}^{-1}$ ) and moderate 0-2.5-km shear ( $18 \text{ ms}^{-1}$ ). At 1615 UTC, there was moisture convergence along the stationary front associated with remnant convection from storms in Minnesota. Within two hours, discrete supercells in a squall line appearance formed. As the line moved eastward, it eventually developed into a bow echo with a defined bowing apex and had taken on a comma shaped echo structure. At the bowing segment, a  $40 \text{ m s}^{-1}$  RIJ was present and was detected by the Lincoln, IL radar. In addition, contrary to the findings in Funk et al. (1999), Atkins et al. (2004) found three meso- $\gamma$  scale vortices south of the bowing segment, with one of them being tornadic. This was one of the first observational studies to show this. There were three vortices that occurred at this scale, but dealt with the location within the system that had not been seen. Not only did it contradict Funk et al. (1999), but also supported Weisman

and Trapp (2003) where they concluded that all of the simulated bow echoes in their research formed north of the apex. Atkins et al. (2004) did not produce a hypothesis as to why this happened.

With an understanding of the environment and observational component of Atkins et al. (2004), the characteristics of the mesovortices will be discussed. When analyzing the scale that the mesovortices developed on, they were all noted as occurring near a boundary intersection. The primary intersection point was between the convective line and an east-west-oriented boundary. This region is a place that would be favorable for convergence, helping to lift and create vertical vorticity stretched into the vertical direction from the surface. The diameter of the mesovortices ranged from 0.5 to 9-km, which is consistent with prior findings (Wakimoto and Wilson 1989; Funk et al. 1999). Some of the vortices were less than two kilometers wide at the start of the life cycle, and even though the locations were close to the Davenport, IA and Lincoln, IL radar, the detectability of the tornadoes was lessened. During the lifetime of these vortices, they did not grow upscale or show a noticeable decrease in the number of them as simulated in Weisman and Trapp (2003). While some vortices did grow larger, they remained firmly in the meso- $\gamma$  scale and did not become a part of the bookend vortex that was observed.

The vortices that formed during the storm, except for one, formed after the system became a bow echo (Atkins et al. 2004). This helps continue the idea that the leading edge of bow echo is a favorable place for mesovortex genesis. The one vortex that formed prior to the bow echo existed longer than the rest (160 min) and was noticeably larger than the others at a diameter of 19-km (Atkins et al. 2004) The reason for this was not discussed in the paper. When looking at all the vortices, tornadic and nontornadic,

the average lifetime was 56 min. When separating them into their respective categories, the average lifetime of a nontornadic circulation was 32 minutes and the lifetime of a tornadic case was 61 minutes when removing the anomalous circulation (Atkins et al. 2004). If a forecaster knows that a tornado has been detected and can determine the kind of cellular structure that the cell exhibits, forecasters can use this information to know how long they should track a reported tornado. This can help to focus their attention to these areas of greatest concern.

The last thing that Atkins et al. (2004) looked at was mesovortex strength, specifically through average radial velocity,  $V_r$ . They found that the tornadic vortices had stronger rotation than nontornadic. They also found that they occurred at low levels in the atmosphere which, according to Trapp et al. (1999), makes these vortices nondescending. Atkins et al. (2004) found that the nontornadic vortices had a  $V_r$  less than  $20 \text{ m s}^{-1}$  and tornadic vortices had a  $V_r$  around  $25 \text{ m s}^{-1}$ . The distribution of the  $V_r$  in the vertical is seen in Figure 2.2.3. The findings from Atkins et al. (2004) indicate that a tornadic vortex can be distinguished from a nontornadic vortex through the size, lifetime, and strength of the vortex observed. Figure 2.2.3 indicates that having radar data as close as possible to the radar is best for detection, but this is not always possible.

**Figure 2.2.3. Composite vertical profiles of  $V_r$  for all tornadic (solid line) and nontornadic (dashed line) mesovortices. Error bars represent 1 std dev for all data points at the respective level. Taken from Atkins et al. (2004).**

Atkins et al. (2005) further expanded upon Atkins et al. (2004). The case analyzed here was a bow echo that moved through the St. Louis WFO during the Bow Echoes and Mesoscale Convective Vortices Experiment (BAMEX) experiment on June 10, 2003 in which 11 vortices occurred where five tornadoes were reported along with multiple wind damage areas with one being over 50-km long. The event was analyzed by the BAMEX team and corroborated along with the radar data as a part of the experiment. Through the BAMEX study, Atkins et al. (2005) identified a potential trigger for the damaging wind areas. Atkins et al. (2005) found that along the leading edge of the bow echo, there appeared to be a descending RIJ with radial velocities in excess of  $30 \text{ m}^{-1}$  with damage occurring north of the bowing apex. This area of damage was collocated with a radar detected mesovortex. This occurred with two vortices that were documented at these locations, having F0 wind damage. These locations were closely related to the

area of tornadogenesis. The mesovortices that did produce a tornado were observed to develop concurrently or within an hour from the initial formation of the RIJ. As the system continued to evolve, the bow echo eventually developed a comma head and a weak-echo channel. Atkins et al. (2005) found that it was on the northern side of the weak-echo channel that the wind damage was reported, similar to the conceptual model from Fujita (1979).

In addition to wind damage analysis, Atkins et al. (2005) further tested the generalizations made about mesovortices in Atkins et al. (2004). For the most part, the findings in Atkins et al. (2004) were verified, but further research is needed before definitive conclusions can be made. The average lifetime of the tornadic mesovortices in Atkins et al. (2005) were 56 minutes, the time before tornadogenesis was 12 minutes, and the average tornado lifetime was 5.5 minutes. The nontornadic mesovortices had a shorter lifetime, 19 minutes, and were weaker than the tornadic circulations by about  $4 \text{ m s}^{-1}$ . This is consistent with the findings in Atkins et al. (2004). In addition, the vortices observed formed in the lowest 3-km, indicating that being closer to the radar could be better for detection. With the mesovortices near the radar, Atkins et al. (2005) documented the evolution of the vortices. In the tornadic vortices, the lowest 2-km were important for detecting and differentiating between the two types. The tornadic vortices strengthened prior to tornadogenesis with the strongest  $V_r$  being at the surface and strengthening with increasing altitude over time, as found in prior research (Wakimoto and Wilson 1989; Trapp et al. 1999; Atkins et al. 2004). The  $V_r$  values observed were in excess of  $16 \text{ m s}^{-1}$ . Due to the increase in  $V_r$ , the azimuthal shear values also increased just prior to tornadogenesis. When compared to the nontornadic vortices, they were

much shallower and weaker when looking at  $V_r$  with values not exceeding  $12 \text{ m s}^{-1}$  which in turn, created weaker azimuthal shear values.

### *b. Modeling Studies*

With the increased capabilities and power of computers, the ability to model and show the dynamic interactions and evolutions has allowed meteorologists to better understand these meso- $\gamma$  scale events. With a solid understanding of the development and movement of the bow echo on the large scale, much of the simulations have focused on the shear and vorticity of mesovortices. Weisman and Trapp (2003) investigated the relationship and dependence that shear had on the development of mesovortices in various wind regimes. Using prior observational events to establish shear baseline categories from  $10$  to  $30 \text{ m s}^{-1}$  over  $2.5$ ,  $5.0$ , and  $7.5$ -km (Weisman 1993; Weisman and Davis 1998; Trapp et al. 1999; Funk et al. 1999), the experiment was run on a free slip boundary with the Klemp and Wilhelmson cloud model with Kessler warm rain physics with  $1$ -km grid spacing.

The simulations of Weisman and Trapp (2003) had the convective systems growing similarly as in Weisman (1992), where they all evolved from an environment that was initially downshear tilted before growing upshear as the cold pool gained strength and deepened. Depending on the shear strength and the depth of the atmosphere, the systems were categorized as weak and disorganized, tilted upshear, organized bow echo, or supercellular. In general, Weisman and Trapp (2003) found that simulations with shear at  $15 \text{ m s}^{-1}$  were not as likely to develop strong and deep mesovortices. Part of this may be due to the RIJ not remaining elevated but rather descending towards the

surface. This would create an environment that is not as supportive for the vertical growth necessary for vortices. In addition, the weaker shear studies had more disorganized cells along the leading edge rather than a sustained area of convection. The stronger shear values of  $30 \text{ m s}^{-1}$  produced results that resembled supercells and were not analyzed closely.

At the moderate shear values of  $20 \text{ m s}^{-1}$ , Weisman and Trapp (2003) produced an idealized convective bow echo. The model produced strong convection along the entirety of the line with a bowed shape and a convective gust front. In addition, the mesovortices produced were deeper and stronger than the  $15 \text{ m s}^{-1}$  vortices and developed along the leading edge of the cold pool. This coincides with the findings from Atkins et al. (2004; 2005). However, Weisman and Trapp (2003) also found in their model that the vortices were located underneath a midlevel updraft, which would allow for additional vortex stretching.

Weisman and Trapp (2003) also did a comparison between the environment and development of supercell and nonsupercell tornadoes to highlight structural differences. Weisman and Trapp (2003) found that the nonsupercell tornadoes are not dependent on a pre-existing rotation in the mid- and upper- levels of the storm. Rather, through the analysis of buoyant forcing, Weisman and Trapp (2003) found that there existed stronger convergence and low-level rotation related to the shear variable at the leading edge of the cold pool, typically the leading edge of a QLCS. There was less dynamic forcing at the surface, indicating that nonsupercell tornadoes are strictly a low-level feature. The lack of dynamic forcing led Weisman and Trapp (2003) to hypothesize that streamwise vorticity is not important to the development and this is further explored in Trapp and

Weisman (2003), discussed in detail in section 2.2.2. They also found that the nonsupercell rotations can last longer than individual supercells, similar to the results by Atkins et al. (2004; 2005), but is shown through a modeled simulation rather than an observation approach.

Atkins and Laurent (2009a) also studied the relationship between low-level shear and mesovortex strength. Their research was conducted using the Advanced Research WRF (ARW-WRF) over a 6-hour simulation. The environment used was from 1800 UTC on June 10<sup>th</sup>, 2003 from Springfield, MO and is the same event in Atkins et al. (2005). The model was run with a 750-m horizontal grid spacing, open lateral boundary condition, Rayleigh damping layer above 12-km, and a free slip lateral boundary condition. The sounding used was “quasi-idealized” when compared to the Weisman and Trapp (2003) sounding. The Springfield sounding had weaker and less shear than the idealized sounding, but did contain more CAPE.

Atkins and Laurent (2009a) found that the strength of the mesovortex was dependent on both the cold pool (eq. 1) and the low-level shear, similar to Weisman and Trapp (2003). The simulated event reproduced was close to the actual event, but the amount of shear in the environment was changed. In their findings, the system was in balance when the shear was at  $30 \text{ m s}^{-1}$  and this produced the strongest and most well defined mesovortices. This is in contrast with Weisman and Trapp (2003) in which shear values at this threshold produced supercell events. This was attributed due to the limited and idealized nature of the Weisman and Trapp (2003) model.

The balance of the cold pool with the shear resulted in upright, deep updrafts and stronger vortex stretching than the control and  $10 \text{ m s}^{-1}$  run. If the cold pool was less

dominant, the updraft tilted downshear or if the cold pool was too dominant, the updraft tilted upshear, as shown in Rotunno et al. (1988). It was during the  $30 \text{ m s}^{-1}$  simulations that the vertical vorticity was the strongest. Atkins and Laurent (2009a) also found that the strength of the Coriolis forcing played a role in the number of mesovortices simulated. If the Coriolis force was stronger than the control,  $1 \times 10^{-4} \text{ s}^{-1}$ , than there were stronger and more mesovortices after the 4-hour mark in the simulation. The opposite was true for a weaker Coriolis forces. The reason that the Coriolis force affects the mesovortex is that the stretching of the vorticity contributes to the amplification of the mesovortices helping to create some initial rotation. Atkins and Laurent (2009a) showed that Coriolis force is an important factor by setting the Coriolis force to zero, which resulted in the least amount of mesovortices being observed.

In addition, Atkins and Laurent (2009a) showed in their model that the strongest surface winds observed were at the bowing apex of the QLCS, as shown in multiple studies (Przybylinski 1995; Atkins et al. 2005). It was found that the strongest surface winds occurred on the southern side of the bowing apex while the mesovortex formed on the northern portion of the apex. There was a direct relationship between how strong the mesovortex was versus the strength of the surface winds. As the RIJ descends towards the surface, the strongest winds occur and this is the time most likely for mesovortex development. The reasons for this are discussed in the next section.

### **2.2.2 Mesovortex Development Theories**

There are three primary theories put forth that deal with the development of mesovortices. The first two theories by Trapp and Wesiman (2003) and Atkins and Laurent (2009b) hypothesize that the development is related to the horizontal baroclinic

vorticity, but differ on the mechanisms of development. The third theory by Xu et al. (2015), unlike the prior two theories, discusses how surface friction impacts the development of mesovortices. Each theory will be discussed as no one theory is the most correct but rather may be situationally based.

*a. Downward vortex line tilting*

Trapp and Weisman (2003) is a continuation of Weisman and Trapp (2003) but with a focus on the genesis of mesovortices using the same experimental methodology. When plotting the horizontal and vertical vorticity of the system simulated with a backwards trajectory, Trapp and Weisman (2003) found that one mechanism of mesovortex generation was the tilting of crosswise horizontal vorticity in the downdraft, as seen in Figure 2.2.4. Two things that can affect this tilting of the horizontal vorticity are the RIJ in a mature QLCS or the cool outflow of a rainy downdraft in a still developing QLCS. During both stages, there are both northern and southern vorticity locations, as shown in Weisman and Trapp (2003), but due to Coriolis forcing as the system develops, vorticity moves to a more northern component. This indicates that the vertical stretching of the vorticity at the surface directly enhances the cyclonic vortex north of the bowing apex and diminishes the anticyclonic vortex due to the Coriolis force. As the RIJ or downdraft pushes down on the horizontal vorticity line, it converts it to a vertical component.

**Figure 2.2.4. Diagram for mesovortex genesis with horizontal crosswise vorticity. Taken from Trapp and Weisman (2003).**

Instances of this type of development were observed in Wakimoto et al. (2006) in which a bow echo from Omaha, NE was analyzed using airborne dual-Doppler radar. This event produced a tornado with F1 damage. In the analysis, Wakimoto et al. (2006) found that there was a vortex couplet that developed, however, unlike what was proposed by Trapp and Weisman (2003), it formed in a region absent of precipitation. This means that the development of the mesovortex is not necessarily related to downdrafts and that the RIJ and mechanically compensating downdrafts at the edge of the system could be responsible for depressing the horizontal vortex lines. An example of this process is seen in Figure 2.2.5. The downward vortex line is still along the leading edge of the cold pool. The compensating downdrafts on the edge observed in the QLCS do not form until the system has reached maturity and the gust front has advanced far enough ahead.

**Figure 2.2.5. Diagram of mesovortex couplet diagram. Taken from Wakimoto et al. (2006).**

*b. Upward vortex line tilting*

Atkins and Laurent (2009b) was an extension of their paper and focused on the development of mesovortices based on Atkins and Laurent (2009a), similar to the Weisman and Trapp two-part study. Using a WRF free slip, Lin microphysics scheme model, they found a different genesis for mesovortex development than Trapp and Weisman (2003). Rather than a mesovortex developing from crosswise vorticity, mesovortices form rather from streamwise vorticity. In this type of vorticity, only northern, cyclonic vortices were identified. An outline of this development is shown in Figure 2.2.6. By analyzing the vertical vorticity equation, Atkins and Laurent (2009b) found that as these parcels descended in a downdraft, they gained horizontal vorticity due to solenoids being present and are generated by the baroclinic zone along the leading edge of the cold pool. This downdraft was present at the early stages as the cells were starting to organize or when the system was well defined and an RIJ was present at the lower levels. As the newly enhanced vorticity parcels encounter an updraft, they help

**Figure 2.2.6. Schematic of cyclonic only mesovortex genesis. Taken from Atkins and Laurent (2009b).**

amplify the stretching of the vorticity into the vertical. This concept of stretching is consistent with prior studies as established earlier.

*c. Inclusion of surface friction*

In both theories of the prior two subsections, the models were run on a slip free boundary. No reason was given for this omission. In order to see if surface friction did impact mesovortex genesis, Xu et al. (2015) completed a simulation of the 2009 May 8<sup>th</sup> “Super Derecho” event in the WRF on a 0.8-km grid spaced model. The results were then broken down and analyzed through circulation and trajectory analysis. In their study, they acknowledged that baroclinicity is a main contributor to the development of mesovortices, but that surface friction does play a role in intensification of mesovortices. The intensification was found to take place in the last few minutes of vortex

strengthening. Xu et al. (2015) found that that the vorticity was both influenced in the streamwise and crosswise vorticity components, but found that the crosswise was generally stronger. This adds support to the findings of Trapp and Weisman (2003), but the existence and influence of streamwise vorticity is important in the development of the vortices as well, also supporting Atkins and Laurent (2009b). The fact that both Trapp and Weisman (2003) and Atkins and Laurent (2009b) managed to produce simulated mesovortices shows that friction is not necessary, but can help create a more realistic environment for simulations. More research is needed to determine how much of a factor surface friction plays in tornadogenesis, especially since it only affected the lowest 300 m in the event simulated by Xu et al. (2015).

### **Section 2.3 Non-Supercell Tornado Parameter**

As discussed in the prior two sections, there is a fair amount that is unknown about nonsupercell environments and the factors for forecasting them. The time scale and rapid development makes forecasting nonsupercell tornadoes more difficult than regular tornadoes. In addition, with the tornadoes being potentially embedded in a QLCS or occurring at night, forecasting is made even more difficult. Work by Lee and Wilhelmson (2000) and Caruso and Davies (2005) documented environments that are favorable for NST development. This environmental understanding for NST provided the foundation for the development and use of the non-supercell tornadic parameter (NSTP) by Baumgardt and Cook (2006).

Lee and Wilhelmson (2000) used a modeling approach to determine how much of a role CAPE, vortex sheet strength, and boundary layer vertical shear affected the

development of NST. The model used was a three-dimensional, non-hydrostatic, quasi-compressible, finite-difference cloud model with 60-m horizontal grid spacing. Each of the three factors looked at in the study were looked at individually with a different set of initial conditions. There were six different CAPE simulations, five different vortex sheet simulations, and seven different vertical shear simulations.

Lee and Wilhelmson (2000) were able to draw a few conclusions on each parameter analyzed. For CAPE, they found a strong, direct relationship between the amount of CAPE in the environment and the strength of mesovortices. CAPE values over  $1100 \text{ J kg}^{-1}$  were found to be the most likely to produce NSTs and that stronger CAPE values created stronger mesovortices. The reason for this vortex strength increase is that stronger CAPE values caused the vortex to contract more leading to stronger vortex stretching. Due to the energy related factor, low CAPE values were not as much of a threat. Stronger CAPE values also created a pressure deficit at the surface, about 10 mb, which created a spot for stronger convergence, helping to aid in updraft forcing. This was one factor that Lee and Wilhelmson (2000) looked at.

The second parameter that Lee and Wilhelmson (2000) researched was vortex sheets. Vortex sheets are the layers of vorticity that exist within convection and as a force, such as a convergence boundary or an updraft, occur, the sheets roll up into a vertically extending spiral (Markowski and Richardson 2014). An example of this type of curl that occurs is a Kelvin-Helmholtz wave. Lee and Wilhelmson (2000) found that as the strength of the vorticity increased, the concentration of vorticity increased, indicating a strengthening sheet and tighter spiral. This would create another area of convergence that would further interact with the updrafts at the leading edge of the

system, where NSTs are common. Values over  $10 \text{ m s}^{-1}$  are more favorable for NST formation. There is literature supporting vortex sheets in supercell tornadoes, but the function of them in nonsupercell storms is not as well documented, leading to a lack of true understanding of their influence in a NST environment.

The last parameter looked at was boundary layer shear. As shown in Atkins et al. (2004; 2005), Weisman (1992), and Weisman and Trapp (2003), shear is an important factor for mesovortex development. Lee and Wilhelmson (2000) found that an ambient vertical shear of 80-120% relative to the boundary shear was necessary for development. These findings related to the balance of the cold pool and how upstream or downstream tilting is not conducive to a strong long-lasting QLCS (Rotunno et al. 1988). The work by Lee and Wilhelmson (2000) was a part of the foundation of the NSTP parameter.

The environmental conditions researched in Caruso and Davies (2005) provide a realistic synoptic overview of what forecasters should look for. Caruso and Davies looked at three types of NST events as a part of the investigation into a favorable environment for development. An ideal surface synoptic environment is shown in Figure 2.3.1. The figure depicts a slow moving or stationary surface boundary. The image does not have wind barbs on it, but the wind change associated with the boundary is assumed and creates an area of convergence of preexisting shear and vertical vorticity. Figure 2.3.1 also shows warm surface temperatures at the boundary of the fronts, which aid in steep low-level (0-3 km) lapse rates. The lapse rates, coupled with an overlying moderate CAPE region ( $1500 \text{ J kg}^{-1}$ ), is generally an indicator of tornadic development in supercells (Rasmussen 2003) and work in NST environments as well (Funk et al. 1999;

**Figure 2.3.1. Composite example by Davies (2003) depicting a typical setting that can support nonmesocyclone tornadoes. Red dots denote surface heating axis of steep lapse rates and the area enclosed in green denotes 0-3 km MLCAPE > 40 J kg<sup>-1</sup>. Taken from Caruso and Davies (2005).**

Atkins 2004). If there is CIN lacking in the environment, rapid vertical stretching can occur, leading to NST development.

In the three cases investigated by Caruso and Davies (2005), tornadogenesis occurred during the early portion of the updraft cycle when a front or outflow boundary interacted with the main frontal zone. Unlike the simulations in Weisman and Trapp (2003) and Atkins and Laurent (2009a), there was no well-developed QLCS but rather discrete cells forming along a slow-moving boundary. In further contrast with Weisman and Trapp (2003), weak shear was seen in two of the cases of analyzed showing even though weak shear is not preferred, NSTs can still form. The results looked similar to the

weak shear cases ( $10 \text{ m s}^{-1}$ ) seen in Weisman and Trapp (2003). Caruso and Davies (2005) stressed that a mesoanalysis of the environment and identification of NST features is still needed as the situation can change rapidly.

With a basic environment analyzed, Baumgardt and Cook (2006) used this to develop the nonsupercell tornado parameter. The parameter is as follows:

$$\text{NSTP} = \left(\frac{LR_{0-1}}{9}\right) \left(\frac{MLCAPE_3}{100}\right) \left(\frac{225 - MLCIN}{200}\right) \left(\frac{18 - Shear_6}{5}\right) \left(\frac{\zeta_r}{8}\right) \quad (5)$$

where  $LR_{0-1}$  is the 0-1 km temperature lapse rate in  $^{\circ}\text{C km}^{-1}$ ,  $MLCAPE_3$  is the convective available potential energy for a 0-1 km mixed-layer parcel lifted to 3 km in  $\text{J Kg}^{-1}$ ,  $MLCIN$  is the convective inhibition for a 0-1 km mixed-layer parcel ( $\text{J Kg}^{-1}$ ),  $Shear_6$  is the 0-6 km Bulk Shear ( $\text{m s}^{-1}$ ) and  $\zeta_r$  is the surface relative vorticity ( $1 \times 10^{-5} \text{ s}^{-1}$ ). Based on the equation, it was determined that values in excess of 1 indicated areas at a higher risk of NST development. Equation 4 targets high lapse rates ( $\geq 9 \text{ }^{\circ}\text{C km}^{-1}$ ),  $MLCAPE \geq 100 \text{ J Kg}^{-1}$ , low  $MLCIN (\leq 25 \text{ J kg}^{-1})$ ,  $shear \leq 13 \text{ ms}^{-1}$  (26 knots), and vorticity greater than or equal to  $8 \times 10^{-5} \text{ s}^{-1}$ . The weaker shear values are to avoid shear values that are normally associated with stronger, discrete supercells. However, when compared to the simulated outcome by Trapp and Weisman (2003), the parameter may not work for a faster moving QLCS, even though NSTs are documented to occur within them (Funk et al. 1999).

The NSTP was developed and used on the 13-km RUC model. It was used in six WFOs where it was locally initialized on the Local Analysis and Prediction System (LAPS) in AWIPS. Events that occurred were documented and qualitatively assessed by Baumgardt and Cook (2006) to determine the effectiveness of the parameter.

In the three cases analyzed, the parameter did show skill in helping highlight areas of potential NST development. An example of the output is seen in Figure 2.3.2. The

line in white indicates where the boundary was, and just to the south of boundary line, there was a NSTP in excess of 2. At this location, a tornado did occur, meaning the parameter did help from a forecasting standpoint. Figure 2.3.2 however highlights other areas of NSTP values in excess of 1. In their analysis, Baumgardt and Cook (2006) found that false alarm rates (FAR) could be high depending on grid resolution and if there are anomalously high factors from one of the components of the parameter itself. However, the use of the parameter does help forecasters take notice that the environment is favorable for NST development. This is just one tool that they can use to forecast. Rather than being reactionary, this would allow forecasters to rely on their skill and knowledge to truly assess the situation as it evolves. If the NSTP value indicates that an environment is capable of producing a nonsupercell tornado, a forecaster can more promptly and accurately react to the situation. The parameter, while still relatively new, is currently in use by SPC, helping to bring credence to its utility in forecasting. However, Baumgardt and Cook (2006) is the one and only paper on the parameter so more research the NSTP is strongly needed.

**Figure 2.3.2. 1800 UTC 16 June 2004 LAPS NST image (red 1-2, magenta>2). Solid white line indicates the stationary boundary at 1800 UTC and “X” indicates NST maxima not associated with a linear boundary. Taken from Baumgardt and Cook (2006).**

## **Section 2.4 Ensemble Modeling**

Computers are a key factor in forecasting and have come to the forefront in predictability and understanding of the atmosphere. Numerical weather predictions however always need to be assessed with a subjective view as they rely on sensitive dependence with initial conditions as subtle changes can create different forecast results (Lorenz 1969). As computer power continues to increase, fine-scale resolutions can be run on these processes allowing for better accuracy. There are a variety of different models and approaches in how to accurately represent the forecast. One way to forecast is based on the idea of ensemble modeling. The goal of ensemble modeling is to give a spread of a forecast as to best capture all the potential probabilities (Stensrud et al. 2000). With this approach, a probability distribution function is created to show a spread. An example of an output of what this looks like is the Short-Range Ensemble Forecast

(SREF) system used by SPC currently. Within an ensemble model, forecast variability, error, spread, bias, and other features can both be seen and calculated. The difference in the model outputs is determined based on the model setup. The setup can range from the different parameterizations used, initial conditions, and scale of forecast. Stensrud et al. (2000) used both a single model and a multimodel approach. In a single model, the parameterization is the same but the initial observations and conditions are changed while a multimodal approach has the same initial conditions but the parameterization and physics between the two models is different. Stensrud et al. (2000) found that the multimodel approach with varied physical and parametrization conditions resulted in a better forecast. This was because the model could capture the uncertainty, especially in a short-range forecast. Both approaches had errors, but after 6 hours, the errors became steadier and were not as varied.

The multimodel approach was also used in Tapiador et al. (2012). They ran models with both different initial conditions on top of the varied model physics. By using this approach, Tapiador et al. (2012) found that using a multiphysical parametrization ensemble model was more skillful than an individual model approach. This approach allows for a variety of different outcomes based on the assumption that each model does something better in one aspect when compared to another model. This approach used by Tapiador et al. (2012) and the use of perturbed initial conditions is used at NCEP.

As computers gained power, smaller grid resolutions were possible. Kong et al. (2006) used a nested ensemble grid model of 24-km and 6-km with different cumulus parametrizations and compared the results to a 3-km ensemble model with explicit

convection, explicit cloud microphysics, and assimilated radar data over the south central United States. The 3-km model was treated as truth. While the nested grid model did a decent job of simulating the convection in the model, the 3-km model outperformed the other one. The use of ensemble data was better than a single deterministic forecast for both models. The 3-km model was especially helpful as it highlighted areas of convection better than the gridded model (Kong et al. 2006).

Even though the NSTP has not been used in a model to test predictability to the author's knowledge, the supercell tornado parameter (STP) has been tested in a WRF model in Wheatley et al. (2012). The supercell tornado parameter was created by Thompson et al. (2002) and is used to find areas of potentially strong tornadoes (F2 or greater). The parameter uses CAPE, low level shear, storm relative helicity, CIN, and the LCL. Just like the NSTP, areas with values greater than 1 have a higher likelihood of tornadic development according to the STP. Twenty-eight different tornadic events were selected and run through the WRF with different microphysics, cumulus, and PBL schemes. While the events selected for the study were stronger tornado events, the results still show the model being able to simulate the events well. Since the parameter is in use by SPC, Wheatley et al. (2012) used a 6-hour short-range forecast to compare the results. They found that the ensemble approach was better able to focus on the area of highest tornadic probability than the approach without data assimilation.

## **Chapter 3 Methodology**

### **3.1 Event Selection**

The event used for this research was a tornadic QLCS case from 07 August 2013 that affected the Green Bay, Wisconsin Weather Forecast Office. The event analyzed affected the area after 0500 UTC. This case analysis was suggested by the late Ron Pryzbylinski. This case proved interesting and was thought to be a good example of QLCS predictability and issues often associated with them, specifically tornado predictability. With this approach in mind, the Nonsupercell Tornado Parameter was identified as a potential to aid in forecasting as the parameter is currently in use at SPC.

### **3.2 Data Selection and Processing for Case Analysis**

Model data for analysis were obtained from the NOAA Operational Model Archive and Distribution System (NOMADS). The model data used for the case analysis were the forecast fields from the 13-km 0000 UTC Rapid Update Cycle (RUC) from 7 August 2013. The General Meteorology Package (GEMPAK) at the University of Missouri Weather and Visualization Lab was employed for analysis. The files contain all the data necessary to do a case analysis from the event, such as Skew-T and other model data for each major level. The data does not, however, contain all the data necessary to compute the NTSP. In order to achieve this, the \*.gem files had to be manipulated to account for the u and v component of wind at 10 m to find the shear needed. In addition, the CAPE and CIN had to be allowed to be computed at every level. Finally, a script was written to allow for the actual NST parameter to be computed. Each value was calculated individually in the script per the Baumgardt and Cook (2006) equation and once the

components were found, the final multiplication step was calculated to get the composite NSTP value. This method showed how the RUC model at the time would have predicted that event, but only for the window of time from 0400 to 0600 UTC, as the start time was the 0000 UTC model forecast. This allowed for the ability to determine the skill of the forecast. The SPC Mesoanalysis archive was used for short term forecasting products that the RUC files did not contain such as bulk shear. Storm damage information came directly from the Green Bay, Wisconsin weather event archive.

NEXRAD Radar Level-II data was downloaded from NCDC for the Green Bay radar site, KGRB. Since the storm system took place over many hours and in many different locations, only the area of study was downloaded. Any general radar overview analysis of the event used came from online archive databases. The data once retrieved was run through the Warning Decision Support System-Integrated Information (WDSSII). The data software program allows for a multitude of additional products to be analyzed from the initial reflectivity and velocity. In this research, WDSSII was primarily used to gather azimuthal shear and convergence and divergence output. In addition to WDSSII radar application, GR2Analyst was also used. This program also allowed for a radar analysis of the event but is much more user-friendly and displayed key features of tornado detection in a 4-panel window, allowing for easier assessment and evaluation of tornado detection. The primary 4-panel window consisted of reflectivity, storm relative velocity, correlation coefficient, and differential reflectivity ( $Z_{DR}$ ). These 4 features are often used in real time to confirm the existence of tornadoes (Romine et al. 2008).

### 3.3 Azimuthal Shear

One component used to establish the exist and strength of the NST during the duration of the event is the azimuthal shear and is available even without dual-pol capability. Azimuthal shear is essentially the rotation divided by the diameter of the circulation in  $s^{-1}$  and is found by applying a Linear Least Squares Derivate method, established by Smith and Elmore (2004). The azimuthal shear is used to measure the strength of the radar-observed rotation in mesocyclones. The radial velocity data taken from radars is placed in a 3x3 median filter box to reduce noise. From the radar scan, the velocity data is placed on a 2-D plane and smoothed to give one continuous image and only areas with reflectivity values with greater than or equal to 20 dBZ are kept while, the others are removed (WDTB, 2016). This helps to add additional quality control. After this step, the maximum value for each angle scan is calculated and blended with the prior image scan to determine a gradient of the velocity in that azimuthal direction.

Using azimuthal shear has shown to help aid in the detection of mesocyclones and tornadoes when used along with other radar products. Research from Davis and Parker (2014) showed that values over  $0.01 s^{-1}$  are indicators of mesocyclones. In addition, azimuthal shear is the most useful at the lowest elevation of radar scans, and closer to the radar, as used in Atkins et al. (2004). As the sample gets further away from the radar, the kernel size of the shear become less accurate and allows for larger values to exist artificially. The use of azimuthal shear is also capable to be used post analysis to determine rotational tracks (WDTB, 2016).

### 3.4 WRF Model Structure

The Weather Research and Forecast (WRF) model was used to conduct the model runs used to evaluate the research presented here. The version used was the Advanced Research (ARW-WRF).

The model was initialized using North American Regional Reanalysis (NARR) data from the initialization time of 06 August 2013 at 1200 UTC. The domain area used is shown in Figure 3.1 and is located over the border where Minnesota, Wisconsin and Iowa intersect. The location of the non-nested model is set to include the entirety of the event area with Green Bay, Wisconsin close to the center. The domain was designed to avoid the terrain effects on the western edge from the Rocky Mountains and the influence they might have on the development of the system. NARR data is 32-km, but was downscaled to 13-km to match the same scale that Baumgardt and Cook (2006) conducted his initial tests of NSTP. The WRF downscales by using lateral boundary conditions from the global model and interprets them with the conditions put forth by the model designer and interpolates data where needed (Dulière et al. 2011). The model ran from 1200 UTC on 6 August 2013 till 1800 UTC on 7 August 2013. By starting the model run more than 12 hours in advance of the event, the potential spin-up problems that are usually associated with model starts are avoided. In addition, the time allowed for the entirety of the event to occur from start to finish.

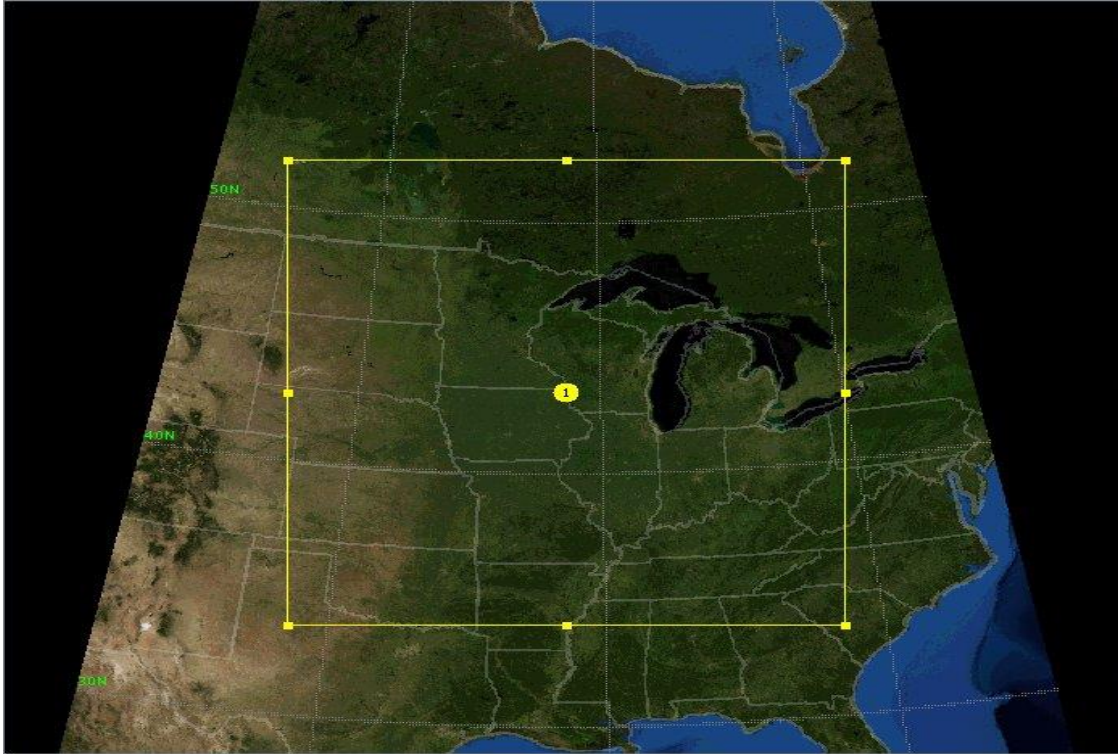


**Figure 3.1. Map projection domain of the unnested 13-km WRF Model Run used with the center point denoted.**

Once the domain wizard was initialized, 24 separate model runs were conducted to establish an ensemble modeling approach. Within the model set up, the only change between each run was the model microphysics and/or the cumulus parameterization. There was a total of four different cumulus parameterizations used and six microphysical schemes. Table 3.1 shows the configuration of these schemes for each model run.

**Table 3.1. Layout of the combination of model configurations used with cumulus parameterization on the left and microphysics on top with associated model run number in the center. The microphysical schemes are denoted with superscripts for brevity and are as follows: a is the Lin et al. scheme, b is the WRF Single Moment 5 Class scheme, c is the Ferrier (Eta) scheme, d is the WRF Single Moment 6 Class scheme, e is the Goddard Scheme, and f is the Milbrandt-Yau Double Moment 7 Class scheme.**

Cumulus Parameterization	Microphysical Scheme					
	Lin <sup>a</sup>	WRF5 <sup>b</sup>	Ferrier <sup>c</sup>	WRF6 <sup>d</sup>	Goddard <sup>e</sup>	MY <sup>f</sup>
Kain-Fritsch	1	2	3	4	5	6
Betts-Miller-Janjic	7	8	9	10	11	12
Simplified Arakawa-Schubert	13	14	15	16	17	18
Grell 3D	19	20	21	22	23	24

The only option that changed for each model was to match one of the 24 combinations shown in Table 3.1, otherwise all model runs were consistently the same. All the models ran for the same amount of time, on the exact same grid, with the same grid spacing and resolution. In addition to grid spacing, other settings that were kept the same in all model runs were: to remain in a non-hydrostatic space, gravity was turned on since the spacing was greater than 10 km; the planetary boundary layer used was the Mellor-Yamada-Nakanishi scheme; and a NOAH (National Centers for Environmental Prediction, Oregon State University, Air Force, Hydrology Lab) Land Surface model was used. The model simulations, once ran, were converted to \*.gem file for use and analysis in GEMPAK with the model data files set to output for every time in the model run. The same steps to get the NSTP script to work in the RUC were also ran in model as the same issues existed.

## **Chapter 4 Case Analysis**

The case analysis is broken into multiple sections. The first section looks at the synoptic and mesoscale model output for the system as it moved through Green Bay, Wisconsin to analyze the data for comparison later with the RUC. The second section covers the radar analysis of the systems.

### **4.1. Synoptic and Mesoscale Forecast**

At 0000 UTC, the surface map (Figure 4.1) depicted a stationary front on the western edge of Wisconsin associated with a weak surface low. Temperatures out ahead of the front were in the middle 60 ° Fs in northern Wisconsin with dew points in the lower 60 ° Fs. Moisture was advected from the Gulf of Mexico partially due to the southern winds ahead of the front. At Green Bay, Wisconsin however, the temperature and dew point were 81° F and 63° F respectively. This area was not as rich with moisture, but the current radar image at 2353 UTC on 6 August 2013 already showed clusters of storms in central Minnesota (Figure 4.2a).

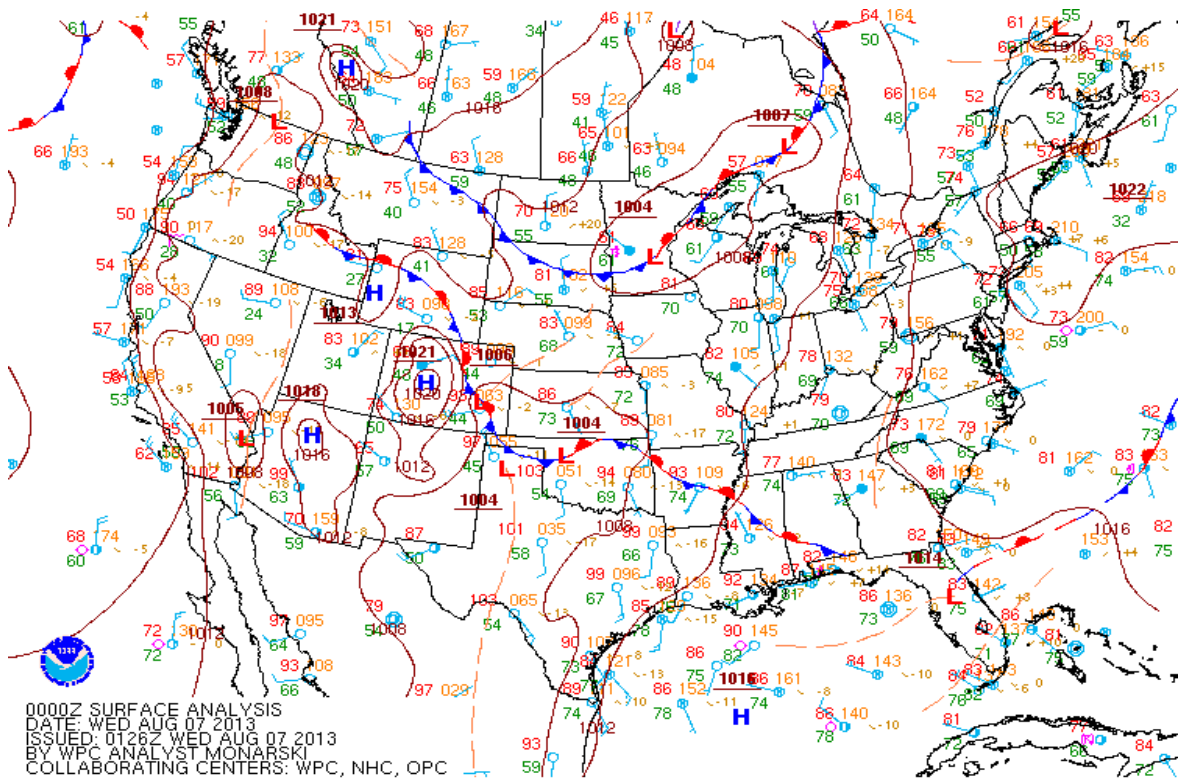


**Figure 4.1. Surface map of CONUS from 07 August 2013 for 0000 UTC.**

These storms initially formed over the eastern edge of the Dakotas and had previously produced hail and damaging wind along with one reported tornado. The storms continued to move into a region of the atmosphere that had yet to utilize the energy from the day, which allowed for conditions to persist. As the storms continued to move to the east, they eventually formed three large, distinct clusters by 0223 UTC on 07 August 2013 (Figure 4.2b.) At 0453 UTC (Figure 4.2c), about 30 minutes before the first tornado report, the cells merged into a linear system with two distinct areas of strong reflectivity. A meso-low was located in central Minnesota and could be identified where the reflectivity region had a bend and it was the southern half of this line below the meso-low that produced the reported tornadoes while the northern half produced only rain.

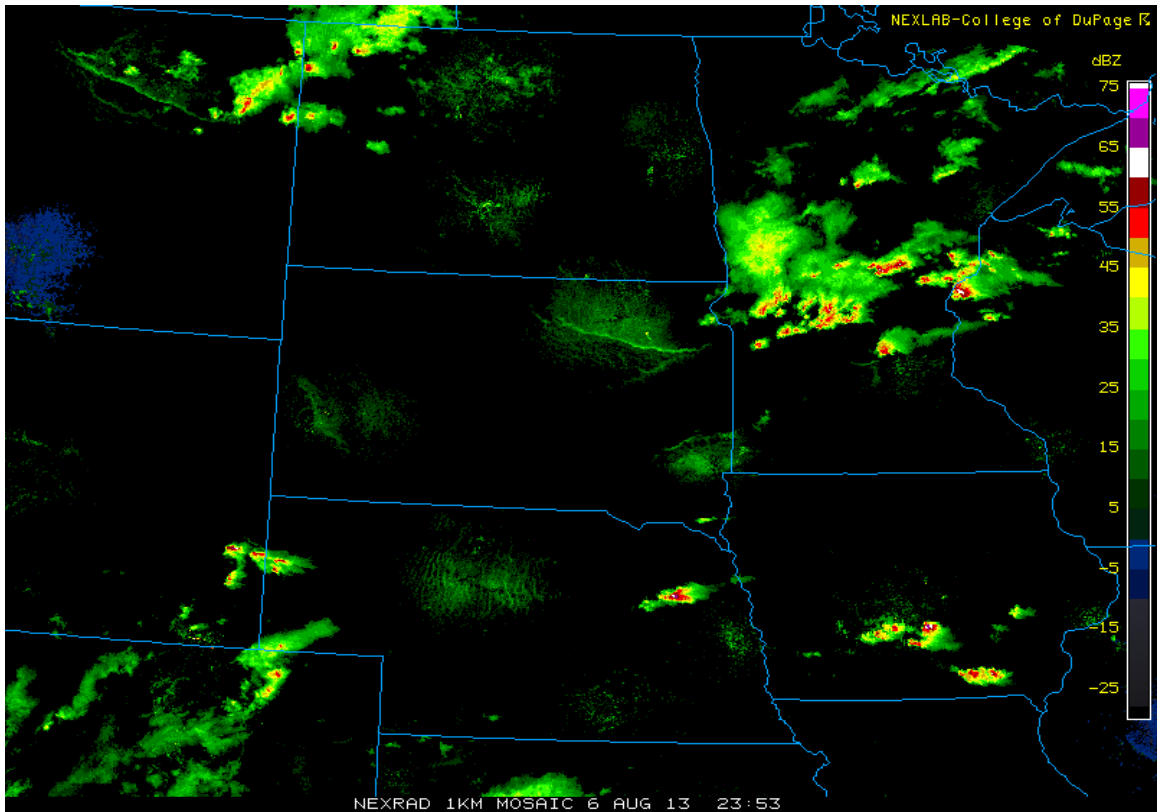


Figure 4.2a. Radar image of the northern plains on 06 August 2013 at 2353 UTC.

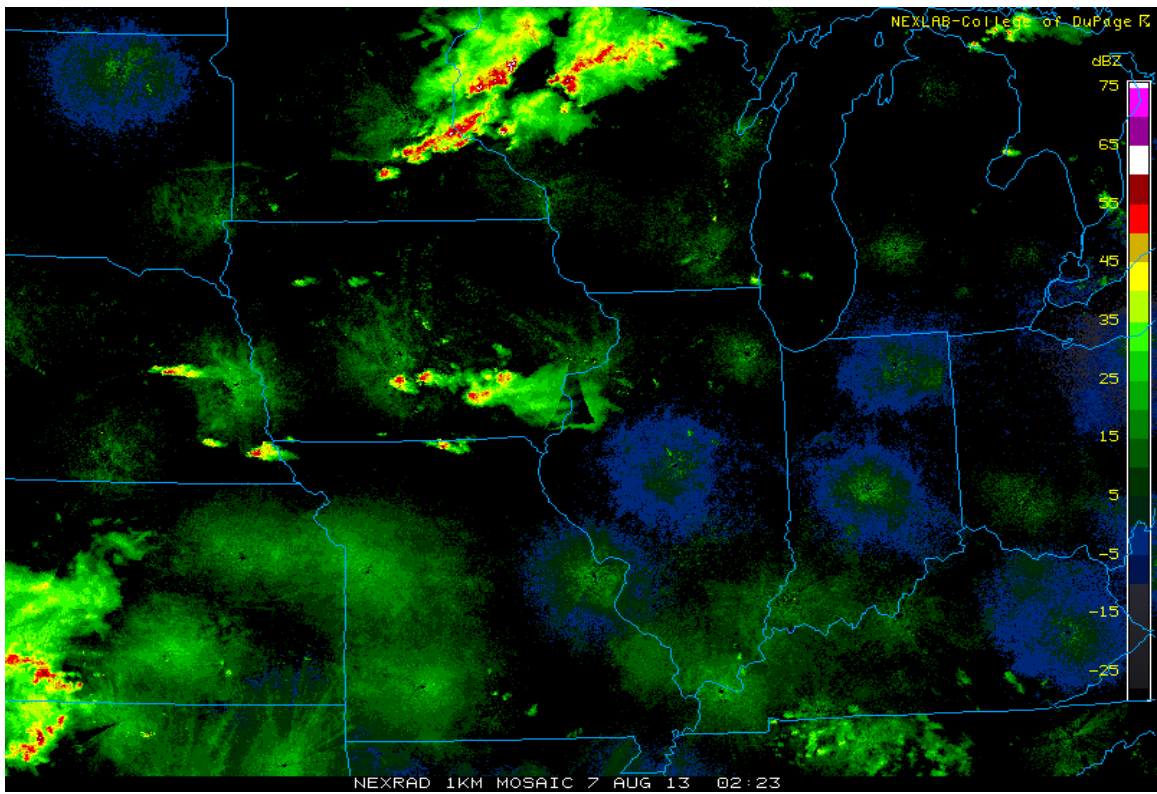


Figure 4.2b. Radar image of the northern plains on 07 August 2013 at 0223 UTC.

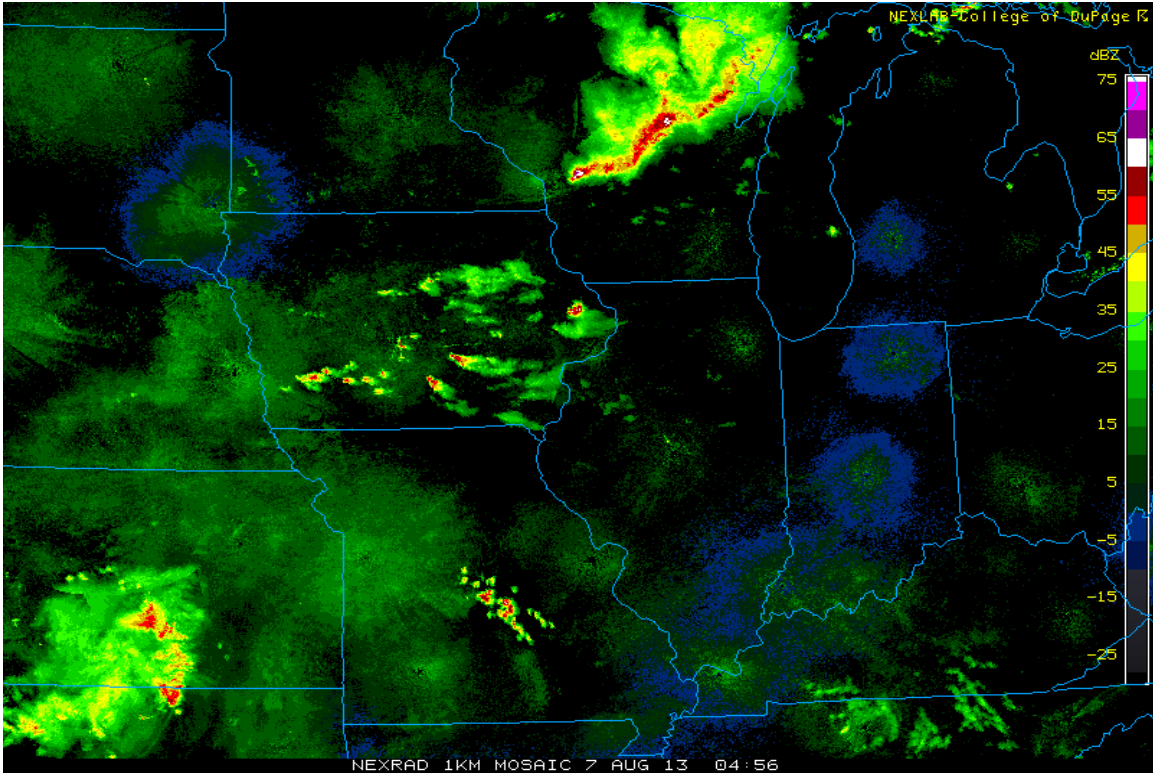


Figure 4.2c. Radar image of the northern plains on 07 August 2013 at 0456 UTC.

Further analysis of current conditions at the upper levels showed the greatest amount of moisture over Green Bay at 850 hPa, as seen in Figure 4.3. There was a cutoff low in central Canada associated with the larger features of the surface the weather pattern. The winds at this level had a more westerly component, but below the influence of the low, there was southerly flow that brought additional moisture to the region. There was a slight moisture ridge in the central MN/WI border region, which helped the system maintain moisture. At the location of the storms, there was strong lift with omega values greater than  $-10 \mu\text{b s}^{-1}$  in central Minnesota. Out ahead of the storms were weak values ranging from  $-2$  to  $2 \mu\text{b s}^{-1}$ . At 500 hPa, the upper-level flow had zonal flow over the upper portion of the US (Figure 4.4). Additionally, at 500 hPa there was a jet streak of more than 50 kts across central MN and WI which helped to drive the storms forward. This continued to progress with the system as it moved. The jet streak was maximized

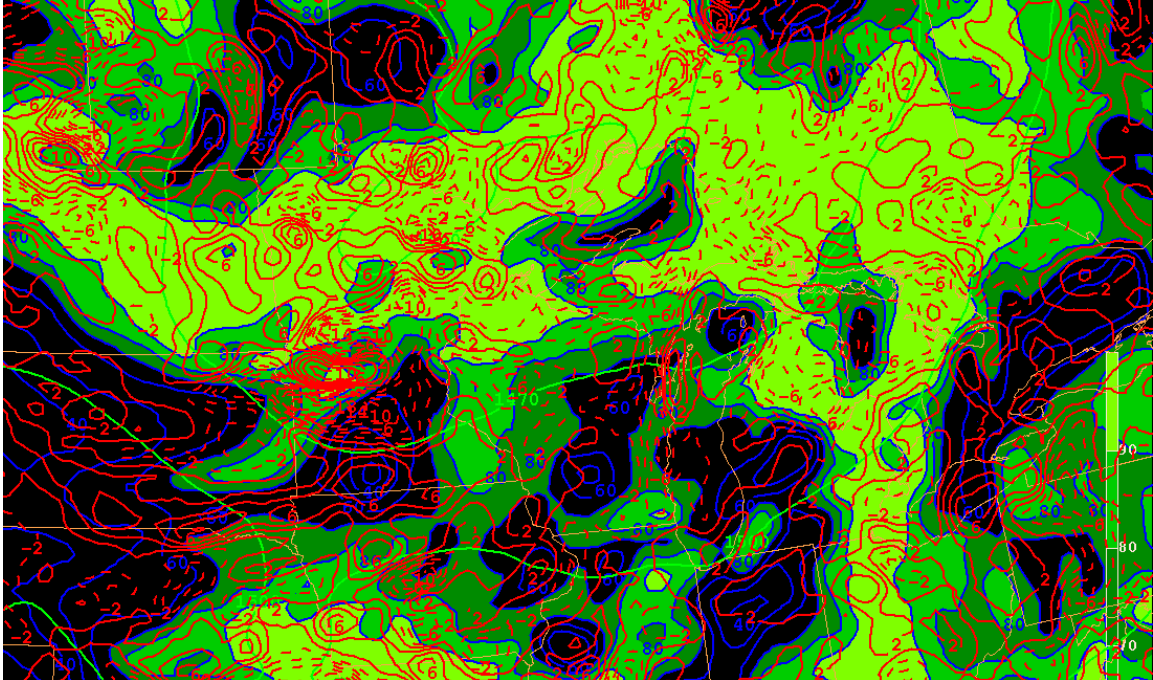


Figure 4.3. 850 hPa analysis at 0000 UTC on 07 August 2013. Green lines are pressure (hPa), red solid/dashed lines are positive/negative omega ( $\mu\text{b s}^{-1}$ ), and blue lines are 850 hPa relative humidity with values over 70% shaded in green.

over this region at 200 hPa with over 80 knots in the area with the same westerly flow as the lower levels. The streamlines also depict an area of confluence over the upper central plains where divergence is also maximized at this region with values in excess of  $3 \times 10^{-5} \text{ s}^{-1}$  (Figure 4.5). The greatest divergence was located in the upper central portion of the jet streak at 200 hPa. This is one thing that aided the development of the system from the discrete cell earlier in the day to the linear event.

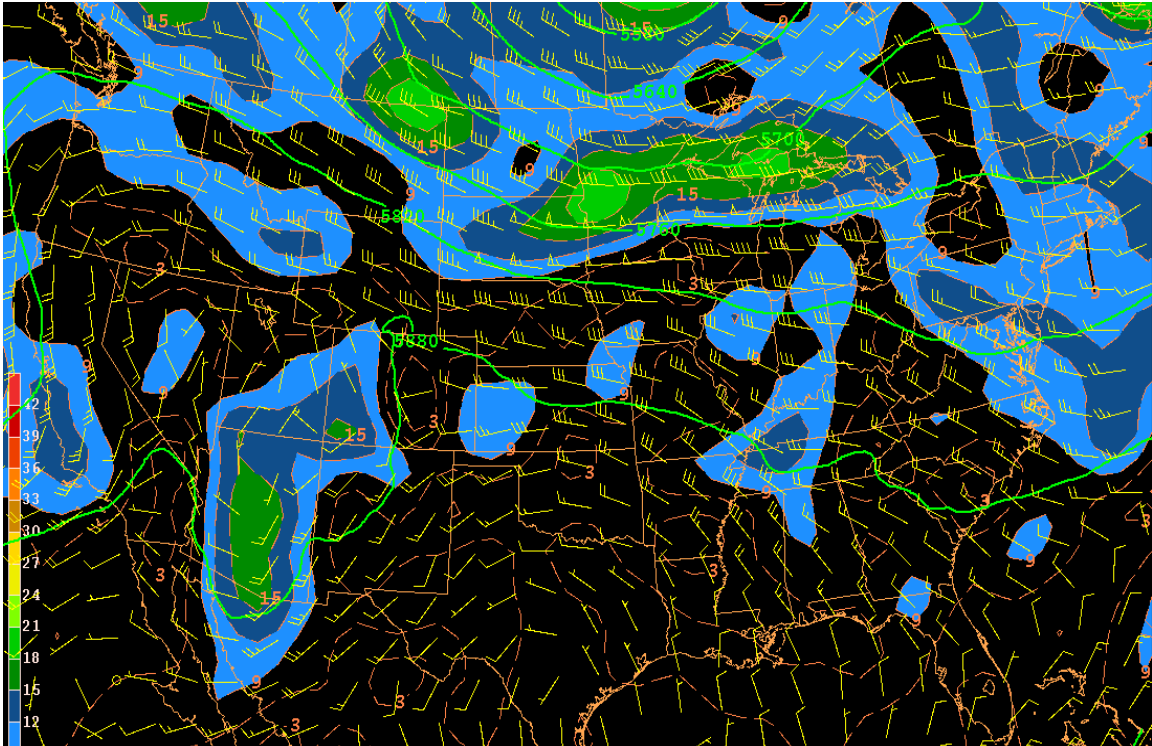


Figure 4.4. 500 hPa map at 0000 UTC on 07 August 2013. Plotted is pressure (hPa) in green, wind (knots) is plotted in yellow, and absolute vorticity is shaded in green and blue.

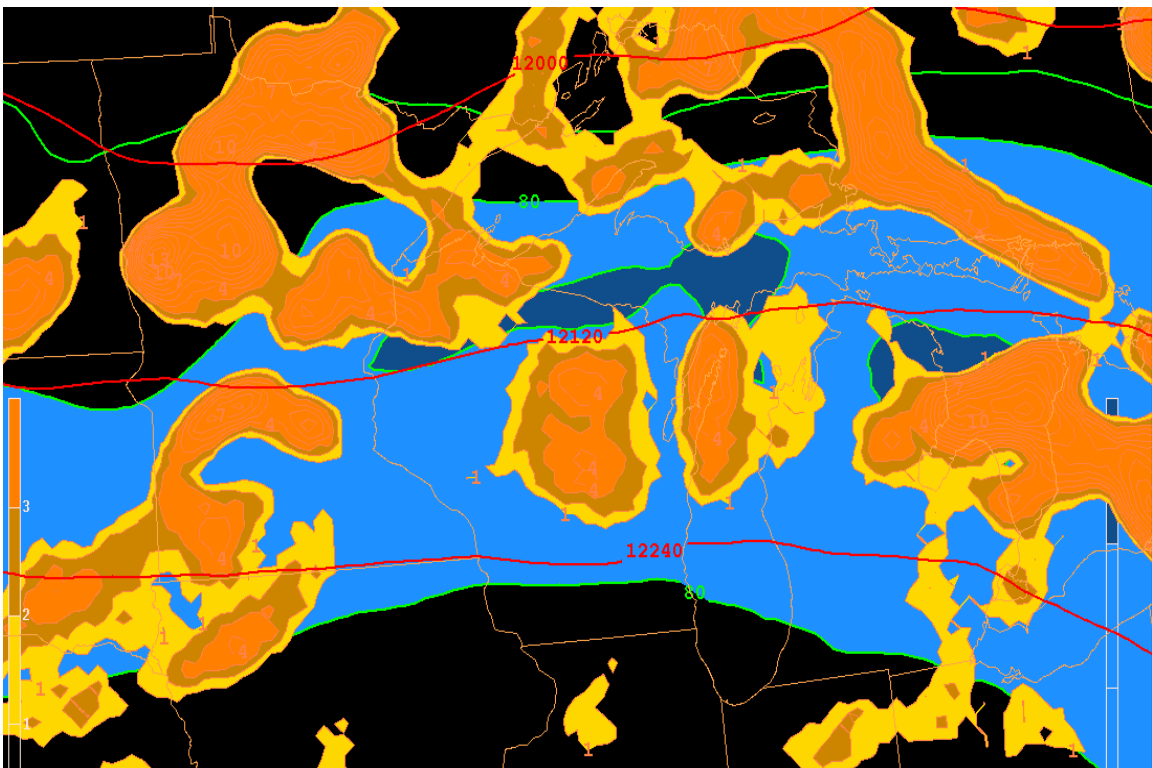


Figure 4.5. 200 hPa upper air map at 0000 UTC on 07 August 2013. Depicted is pressure (red line), divergence in yellow ( $10^{-5} \text{ s}^{-1}$ ), and isotachs (knots).

Analysis of the Green Bay, Wisconsin sounding at 0000 UTC on August 7<sup>th</sup> shows the type of environment that the storms would be moving into. The sounding is shown in Figure 4.6. The sounding shows a dry, but well-mixed layer at the surface in the lowest 100 hPa but has more moisture between 900 hPa to 800 hPa. The LCL and LFC are both at the same level, 870 hPa, which would allow for deep convection, which already existed, allowing for any convection to continue. Most Unstable CAPE was only  $1379 \text{ J kg}^{-1}$ , but little CIN existed in the atmosphere allowing for any storms that developed to do so freely. The sounding showed very little directional shear and only weak to moderate speed shear. However, surface-to-3-km lapse rates were on the higher end of conditionally unstable, with the value at  $8.2 \text{ }^\circ\text{C km}^{-1}$ . Overall, even though the atmosphere near Green Bay was not primed for discrete supercells, it is conducive to the maintenance of a system if it were to move through, as is what happened.

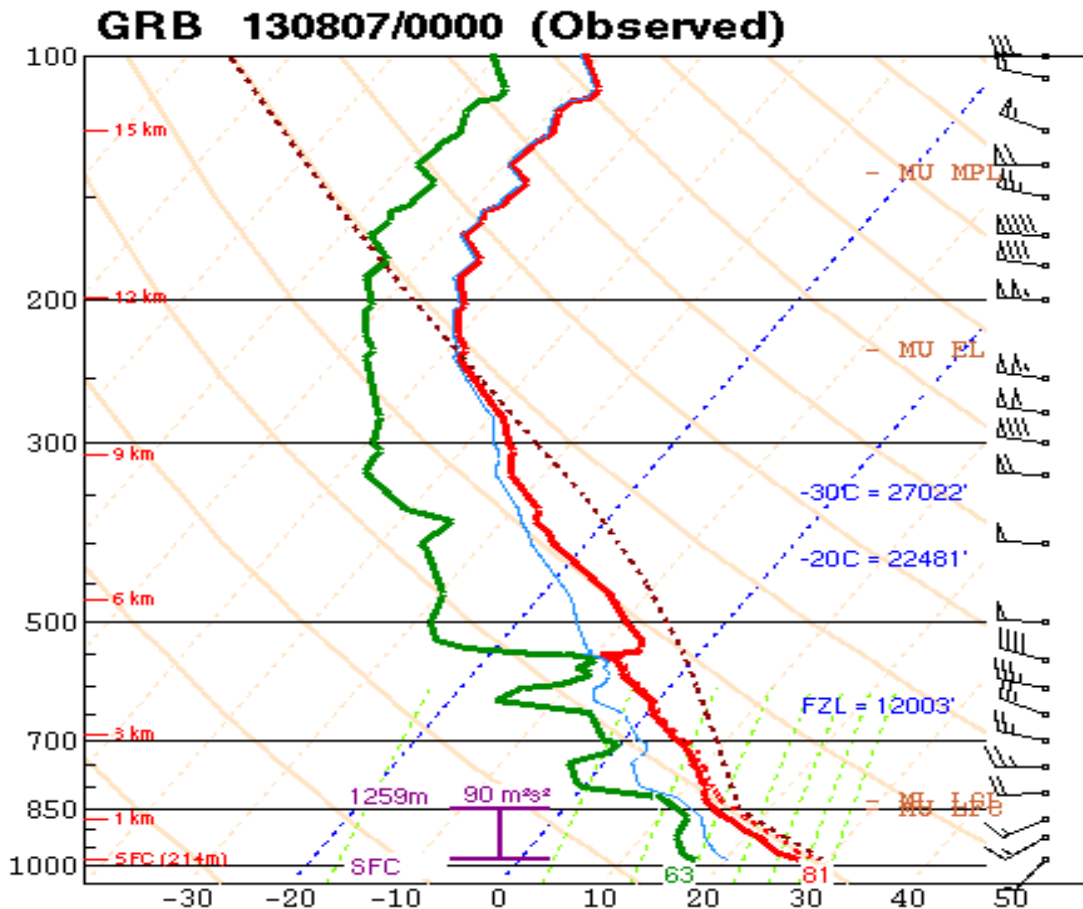
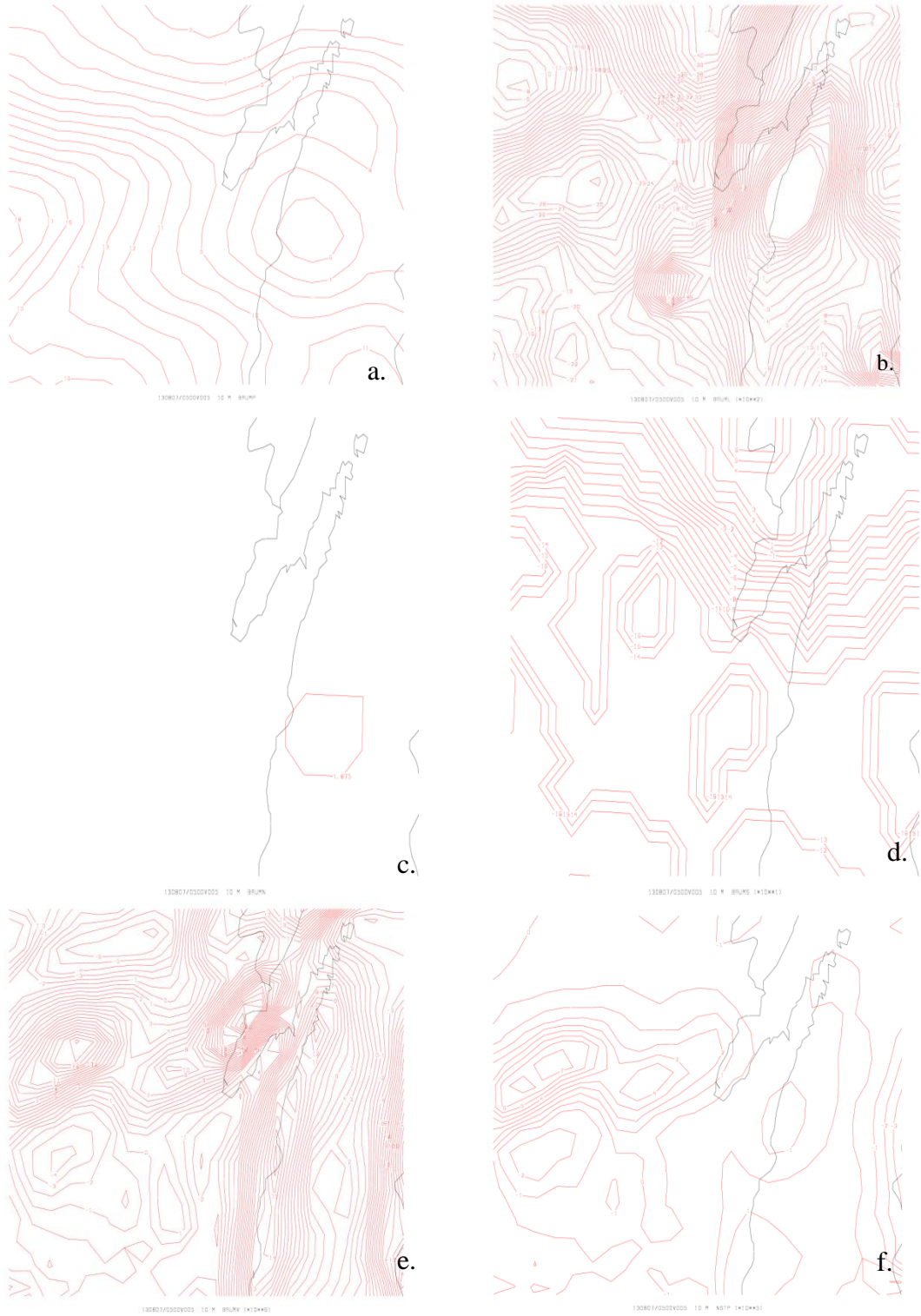


Figure 4.6. Observed radiosonde from KGRB at 0000 UTC on 07 August 2013.

Figure 4.7 (a-f) is the output from the RUC model showing the forecast for the Green Bay area at 0500 UTC on 7 August 2013. This time step is 22 minutes before the first reported tornado event. The maximum CAPE (Figure 4.7a), lapse rate (Figure 4.7b) and CIN (Figure 4.7c) are both ahead of the event while the shear (Figure 4.7d) is at the location that tornadoes occur, but a bit further south than the actual location. The vorticity (Figure 4.7e), however, lags from these components and was located in central Wisconsin which also happens to be the area of lowest shear values. Due to the relationship that vorticity has with the genesis of non-supercell tornadoes, this might influence the NST parameter and the individual components that make up the parameter. If

one value is not as strong as the other, another variable may influence the location, as noted in Baumgardt and Cook (2006). Even though the equation has no weights assigned to each value, this finding may suggest that may be needed. The final output of the NST parameter (Figure 4.7f) placed the event too far to the west of the actual events but did show values greater than 1. These results, while the timing was off, show that the RUC would have been helpful in identifying that the environment was capable of producing nonsupercell tornadoes.



**Figure 4.7. Non-Supercell tornado parameter over the KGRB at 0500 UTC on 07 August 2013. a. CAPE (top left) b. Lapse Rate (top right) c. CIN (middle left) d. Shear (middle right) e. Vorticity (bottom left) f. NSTP composite value (bottom right)**

## 4.2. Radar Analysis

The Green Bay radar as seen in Figure 4.2c depicted a line echo wave pattern associated with the approaching QLCS. The northern portion had weakened significantly since its development, while the southern half strengthened significantly with the strongest portion being near the mesolow that developed. This was the area of greatest concern and is the area associated with the severe weather analyzed. The area ahead of the southern half of the QLCS was placed under a severe thunderstorm watch at 0345 UTC 07 August 2013, indicating to local forecasters that there was the potential for severe weather, as had been previously associated with the system earlier that day. A display of the tornado tracks is shown in Figure 4.8.

The 0508 UTC radar scan showed small convective cells that developed ahead of the main line and persisted until the 0522 UTC scan when they merged with the main line just west of Fremont and New London, WI. The convective cells that formed ahead of the front indicated that the cold pool has advanced slightly ahead of the main convective line. In addition, these convective nudges, once they join with the main line, are a sign of potential nonmesocyclonic tornadic development (Przybylinski et al. 2013). By this point, after the cell merger, the first two tornadoes touched down as depicted in the 0522 UTC radar scan (Figure 4.9). The cell mergers can be seen in the reflectivity near New London and just to the immediate south of it (Figure 4.9a.).

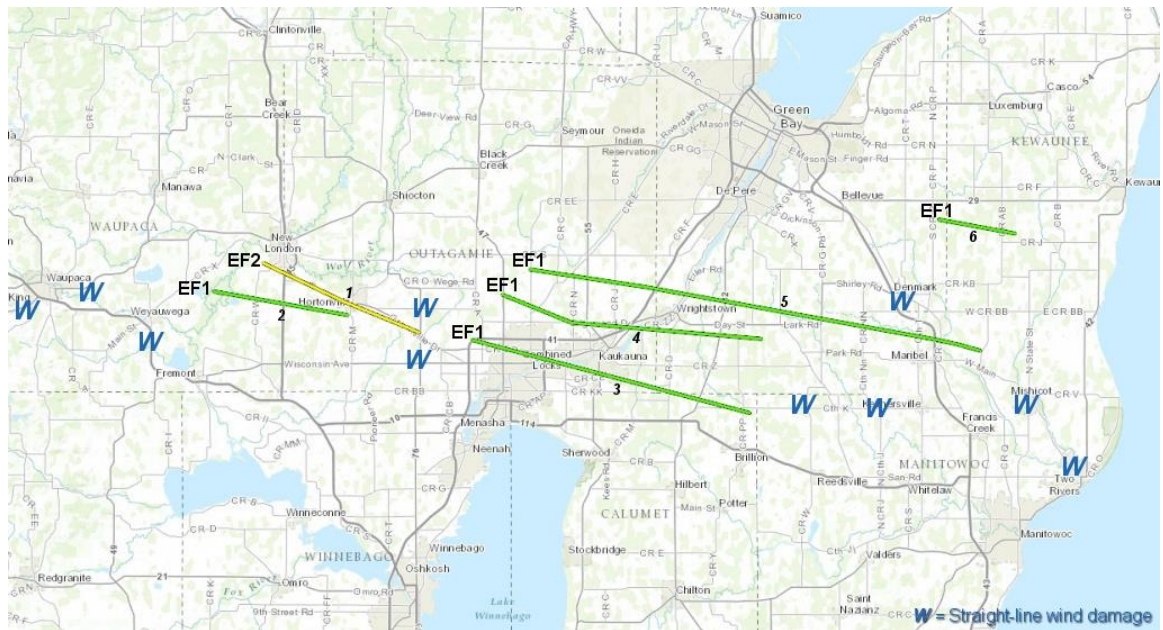


Figure 4.8. Composite of tornadic tracks from 07 August 2013. Taken from Green Bay WFO event page.

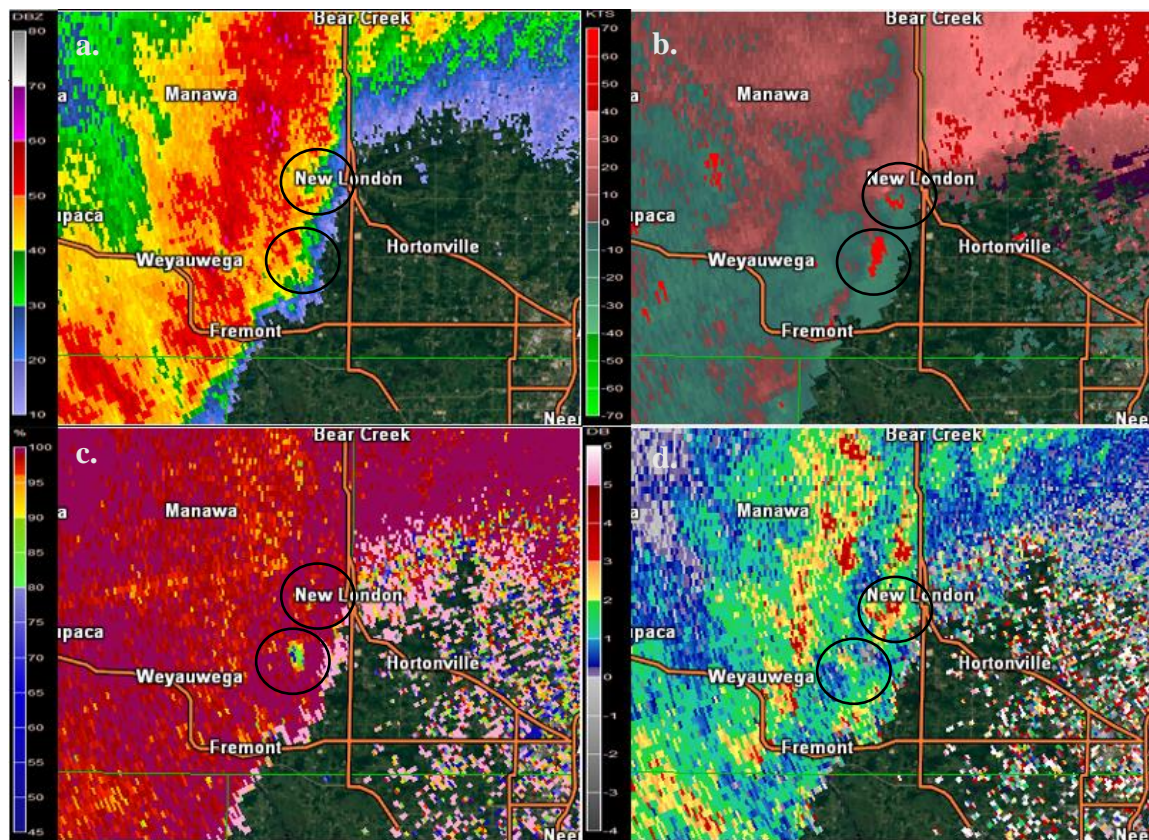


Figure 4.9. KGRB scan at 0.5° radar scan at 0522 UTC on 07 August 2013. Circled areas are tornado locations. Top left a.) Radar reflectivity. Top right b.) Storm Relative Velocity. Bottom left c.) Correlation coefficient. Bottom right d.) Differential Reflectivity.

Figure 4.9a shows a small but clear hook that developed just west of New London, WI where the cells merged. There also appears a small, but less defined hook, at the other cell merger point, halfway between New London and Freemont. This radar scan was 2 minutes before the reported touchdown of the first EF1 and only EF2 reported by the Green Bay, WI office, as seen in Figure 4.8. Both of these tornadoes were along the leading edge of the systems, an area of frequent NST development (Funk et al., 1999; Atkins et al., 2004). In addition, there was radar indicated broad rotation at the two reported locations. Storm relative velocity was based on the thunderstorm warning for the event and kept the same for the entirety of the analysis, 281 degrees at 55 knots. The rotation at both locations went from -20 to 70 knots in a short distance (Figure 4.9b). The velocity and radar image both show a lack of a gust front but there is an incoming/outgoing wind shift at the leading edge associated with the reflectivity hook, indicating that a potential start of a tornado.

The development of the tornado at 0522 UTC is also seen in the correlation coefficient (CC) (Figure 4.9c) and in the differential reflectivity ( $Z_{DR}$ ) (Figure 4.9d). In both figures, there are low values of CC and low values of  $Z_{DR}$  which can be an indicator of a tornado. The location of these low values coincides with the reported locations as seen in Figure 4.8. The CC and  $Z_{DR}$  values for the tornado southwest of New London, WI is clearer than the EF2 tornado near New London, WI. This corresponds with the reported time of the EF1 in this area as it was already occurring. The Green Bay office officially documented this tornado to be on the ground at 0522 UTC and Figure 4.9a-d supports this conclusion. However, by the next radar scan, the EF2 showed up clearly and was officially determined to be on the ground by 0524 UTC.

Unfortunately, during the duration of these two tornadoes, the WDSSII products such as azimuthal shear and convergence/divergence had data errors gaps. As such, they were not used for the tornadoes for the 0522 UTC and 0527 UTC radar scans. This error existed at the  $0.5^\circ$  and  $0.9^\circ$  scan and using higher level scans is not useful with NSTs as they are low level tornadoes.

The reflectivity image became a bit more muddled at the 0527 UTC radar scan (Figure 4.10a). The EF2 was more easily identifiable because there was an inflow notch that could be seen between New London and Hortonville, WI. The EF1 was not very easy to identify in reflectivity but was easier to depict in the other radar products. The storm relative velocity (Figure 4.10b) shows two circulations that were collocated with the two areas of low CC (Figure 4.10c). The CC shows that the two tornadoes are very close to each other. Figure 4.10c depicts potential debris as the values are below 0.8 in the center of the two locations.  $Z_{DR}$  at the EF2 is a smaller area of 0 dB than the EF1 and could be misconstrued as noise when compared to the EF1 tornado. With both tornadoes having been at the leading edge, they could have easily been misinterpreted.

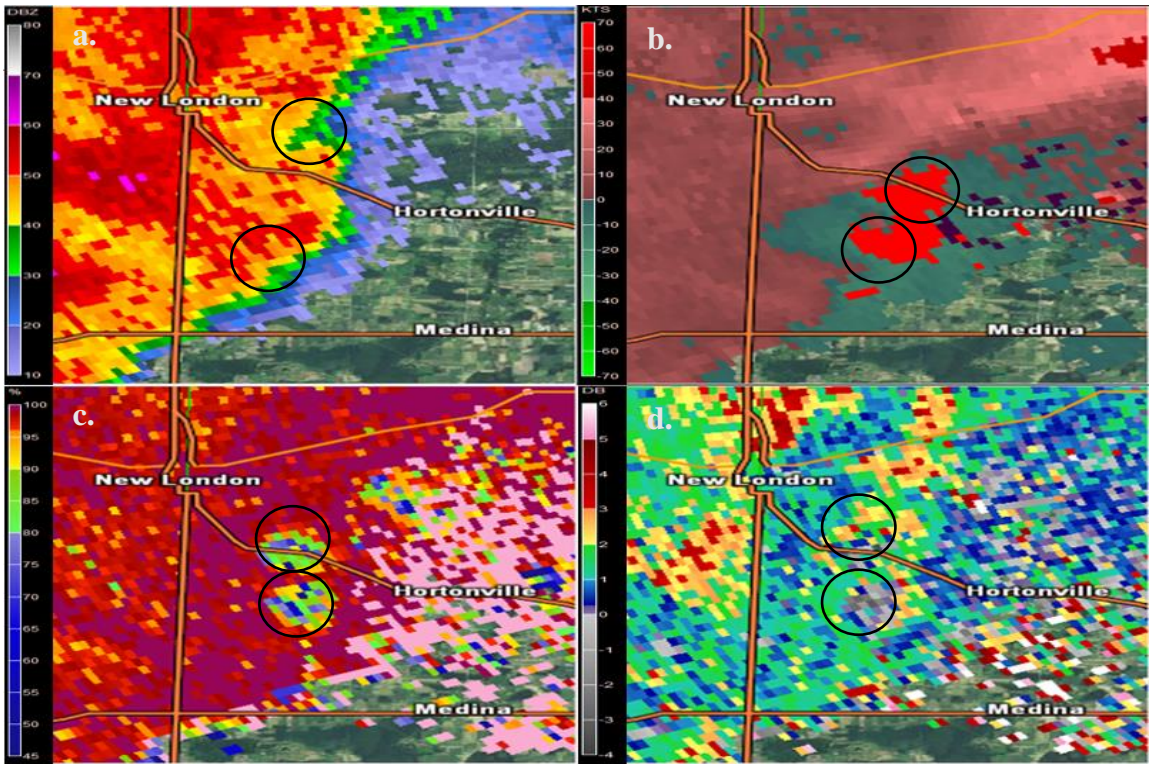


Figure 4.10. Same as Figure 4.9 but at 0527 UTC on 07 August 2013.

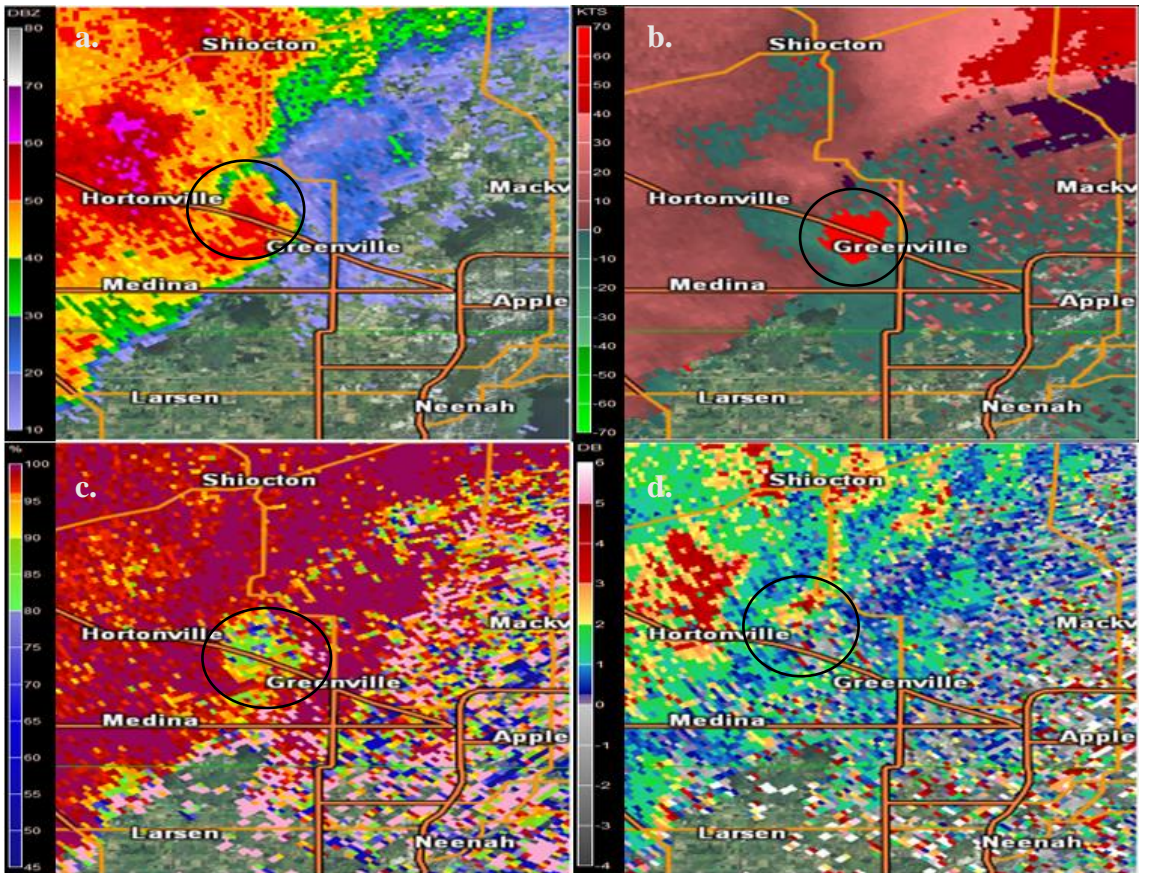
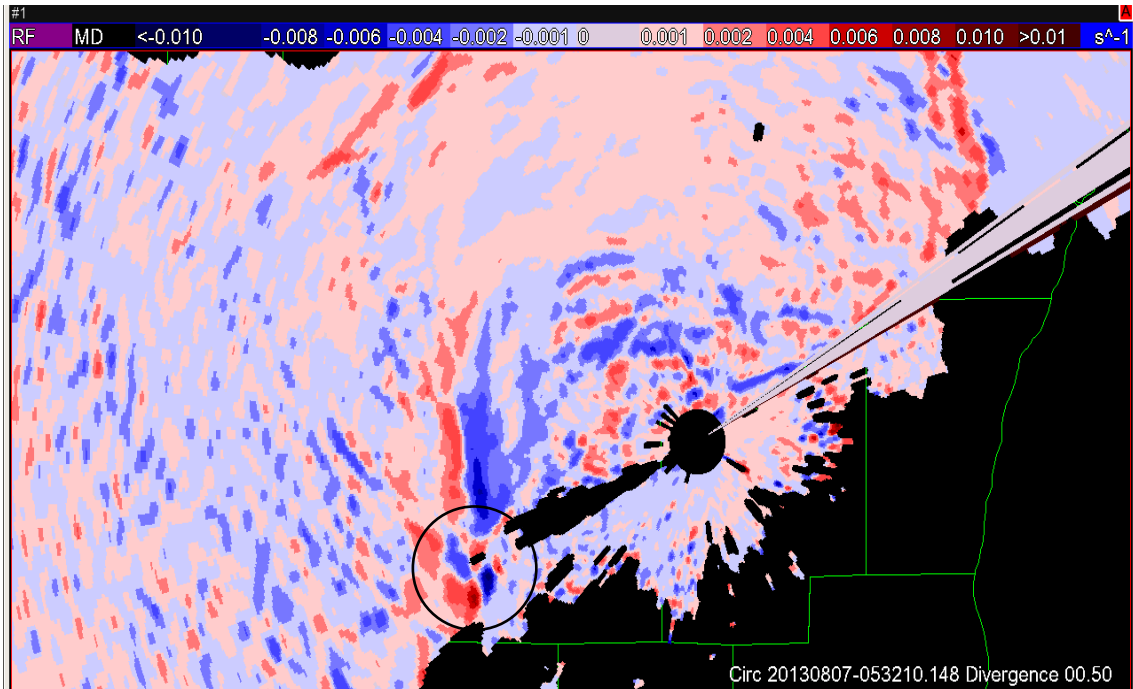


Figure 4.11 Same as Figure 4.9 but at 0531 UTC on 07 August 2013.

The EF1 that formed first only lasted until 0530 UTC, while the EF2 continued to persist for 3 more minutes and ended at 0533 UTC. Radar at 0531 UTC confirmed that the EF1 had dissipated (Figure 4.11). Reflectivity indicated an inflow notch still existed at the leading edge of the system, collocated with where the tornado was supposed to be (Figure 4.11a). Based on the motion of system and the tornadic signals of Figure 4.10, this could have been a potential debris ball that the radar depicted. With the estimated tornadic strength of an EF2, the potential for debris existed. This possibility is only further believed to have been more likely as CC and  $Z_{DR}$  continued to show the low values that are often associated with debris signatures (Figure 4.11c, Figure 4.11d). The main area associated with tornadic activity was just to the east of Hortonville and lines up the tornado track from KGRB (Figure 4.8). Use of the convergence and divergence product from WDSSII also shows the location of the circulation (Figure 4.12). Even though the cities are not depicted, the red/blue quadrant on the southern leading edge showed the circulation as well. The azimuthal shear still had data issues at this time step and was not used. While not included, a zoomed out radar image of reflectivity and velocity showed a developing rear inflow jet. This was noted by the decreased reflectivity at the bowing segment and bowing apex that formed. The analysis of the event took place north of the bowing area which, as shown from prior research, is an area that often favorable for tornadic development due to the circulations at the leading edge (Przybylinski, 1995).



**Figure 4.12** Convergence from KGRB at 0532 UTC on 07 August 2013 at 0.5° tilt. The circle area is the tornadic location.

By the time the EF2 ended at 0533 UTC, the radar showed no distinct signs of any activity occurring other than heavy rain. There is no identifiable inflow notch, no tight velocity circulation, the CC contained high consistent values and the  $Z_{DR}$  lacked low values. While the rest of the radars tools used at this time showed no tornado presence, the azimuthal shear was a clear signal at this time (Figure 4.13). There was a strong difference of rotational velocity at the location of the prior tornado with values above the maximum threshold of greater than  $0.01 \text{ s}^{-1}$ . Throughout the rest of the case analysis, the tornadoes were easily identifiable in the lower levels with this tool. The leading edge of the system was noted as lines in red in the azimuthal shear product. There were other couplets seen similar to the tornadic ones in the northern half of the image, but these were smaller and not associated with severe weather. As such, azimuthal shear is only one component used to determine potential tornado strength and location.

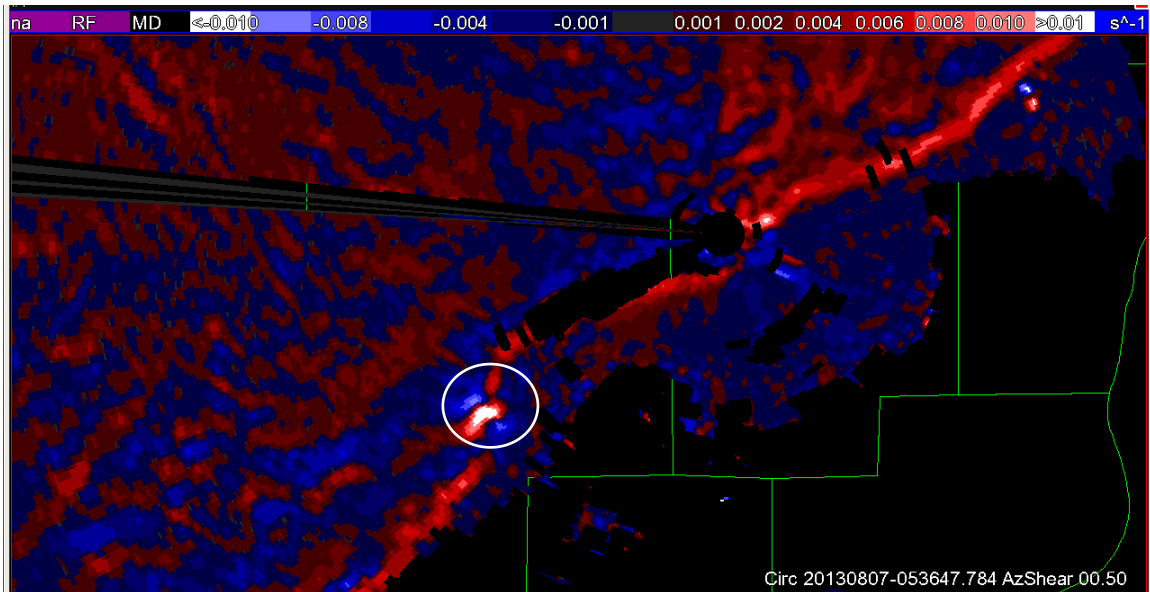


**Figure 4.13. Azimuthal Shear from KGRB at 0532 UTC at 07 August 2013 at the 0.5° tilt. The circle area is the tornadic location.**

Between the 0536 UTC and 0541 UTC radar scan, three more additional tornadoes developed. They are marked as 3, 4, and 5 on Figure 4.8 and all of them were rated EF1. Both tornado 3 and 4 was estimated to have formed at 0538 UTC while tornado 5 formed at 0540 UTC. The tornado start and end times were estimated by the Green Bay, WI WFO. Due to the weak nature of these tornadoes, they were hard to pick out in reflectivity (Figure 4.14a), and only tornado 5 was easy to identify in the velocity scan (Figure 4.14b). In Figure 4.14a, there were three distinct but subtle indentations along the leading line. These indentations correlated with the velocity radar scan (Figure 4.14b) and was a potential inflow area. The correlation coefficient was not helpful in identifying the tornadoes but the radar scan did show tornado 5 a bit more clearly than the other two (Figure 4.14c).  $Z_{DR}$  showed no clear areas of low values (Figure 4.14d). While most of Figure 4.14 made it hard to identify where the tornadoes were occurring, prior knowledge of reported tornadoes would have been useful for forecasters. None of the

first five tornadoes were tornado warned, but were severe thunderstorm warned which, per NWS definition, does include a chance of tornadoes. The use of azimuthal shear would have proved useful for the Green Bay office as it showed three distinct areas of strong rotational shear (Figure 4.15). There was one spot in the middle of map where the shear line was bent. This could be interpreted as an area of rotation, but as seen in the reflectivity and velocity (Figure 4.14 a and b), this was where the QLCS was taking on a LEWP structure. Rather, the three strongest areas lined up with where the velocity image showed rotation (Figure 4.15).

While the signatures of these tornadoes were relatively weak during the first radar scan, the next radar scan at 0546 UTC showed a bit more detail about their location and strength. Tornado 5 showed a clear v inflow notch in the reflectivity (Figure 4.16a) and was collocated with the circulation couplet in the velocity scan (Figure 4.16b). Tornado 3 also showed a reflectivity inflow, albeit smaller than tornado 5, whereas tornado 4 did not develop an inflow notch. This relationship also existed in the velocity scan at the time. The velocity circulation for tornado 4 was very small when compared to that of tornado 5 and tornado 3. Correlation coefficient continued to show the location of tornado 5 while tornado 3 and 4 were much harder to decipher (Figure 4.16c). The strength of tornado 5 may relate to the fact that while it was weak on the Enhanced Fujita scale, it lasted an addition 17 minutes longer than tornado 3 and 4. Azimuthal shear (Figure 17) showed tornado 3 and 5 as being much stronger and more intense than tornado 4. Tornado 4 had values that did not exceed the maximum threshold of being greater than  $0.01 \text{ s}^{-1}$  while tornadoes 3 and 5 did not quite reach the threshold.

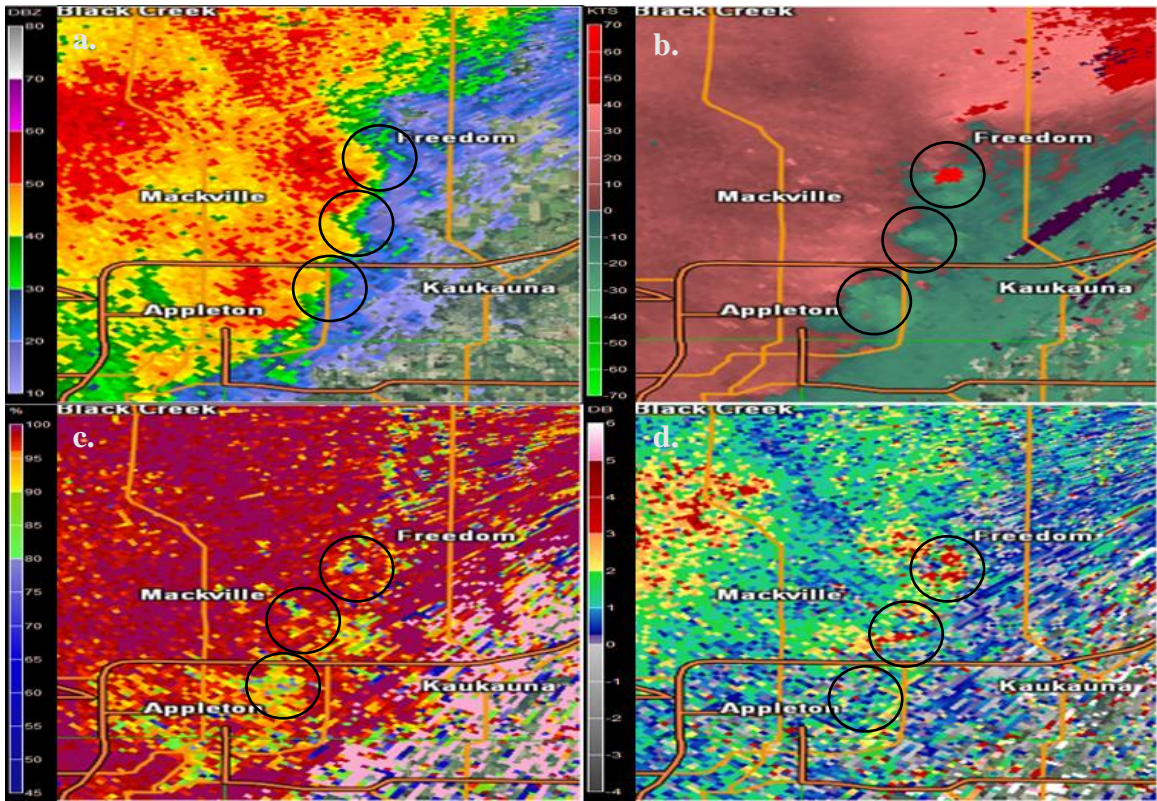


Figure 4.14. Same as Figure 4.9 but at 0541 UTC on 07 August 2013.

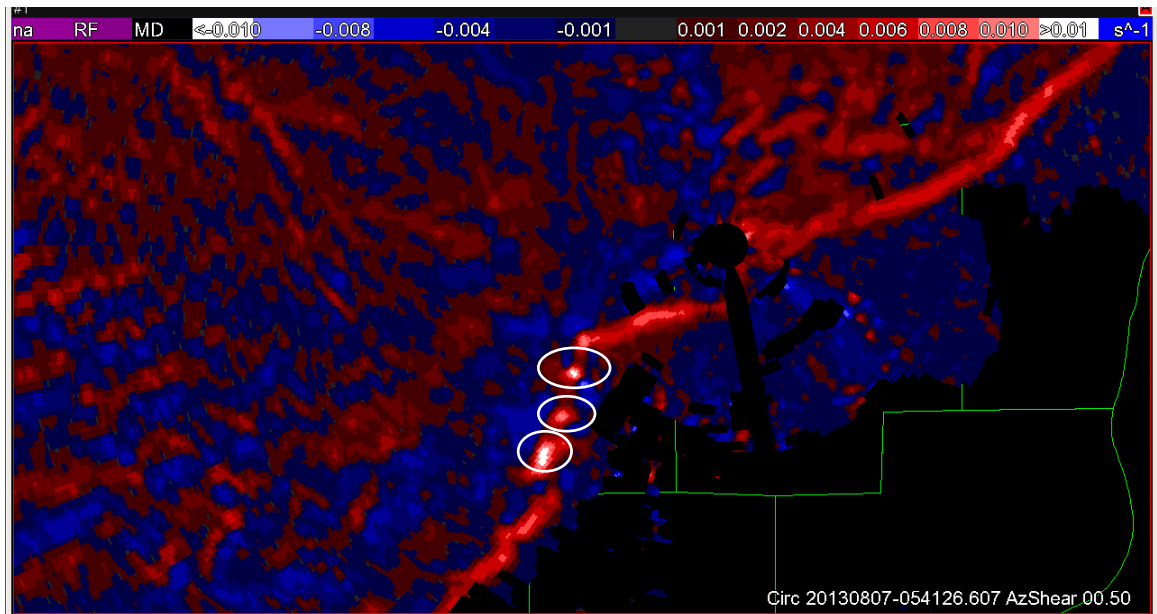


Figure 4.15. Same as Figure 4.13 but at 0541 UTC on 07 August 2013.

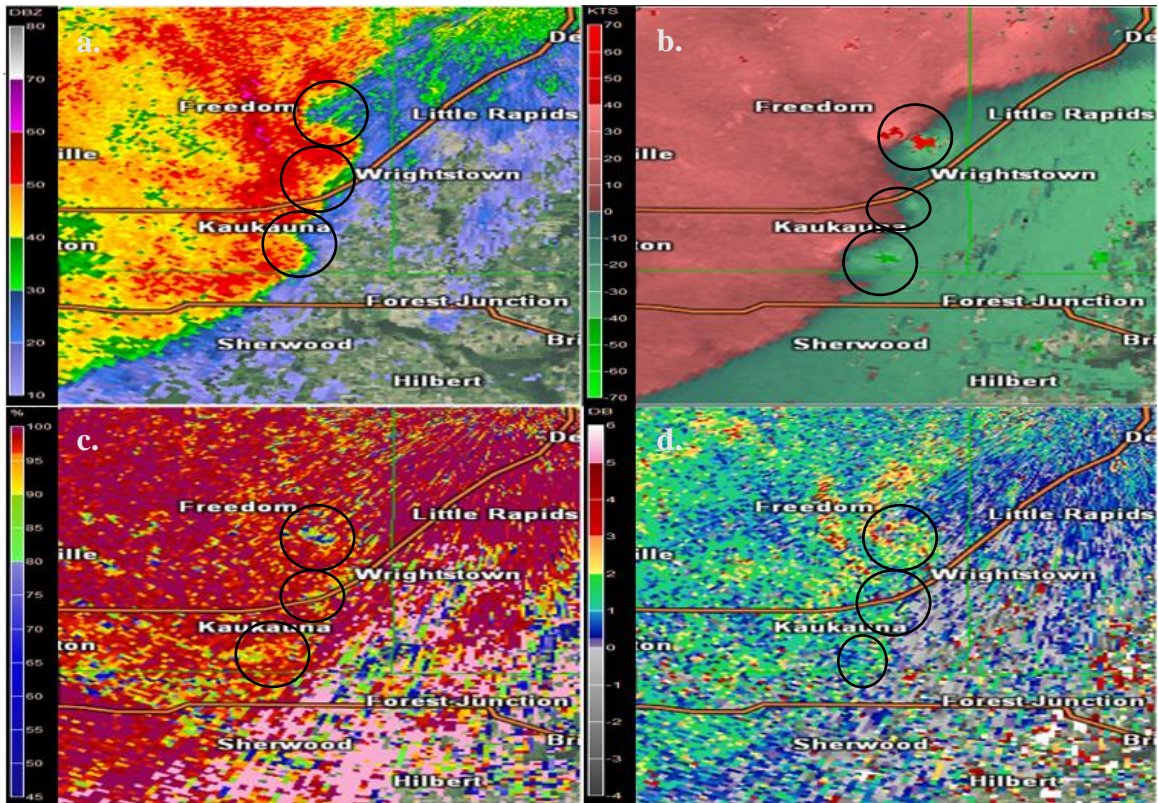


Figure 4.16. Same as Figure 4.9 but at 0546 UTC on 07 August 2013.

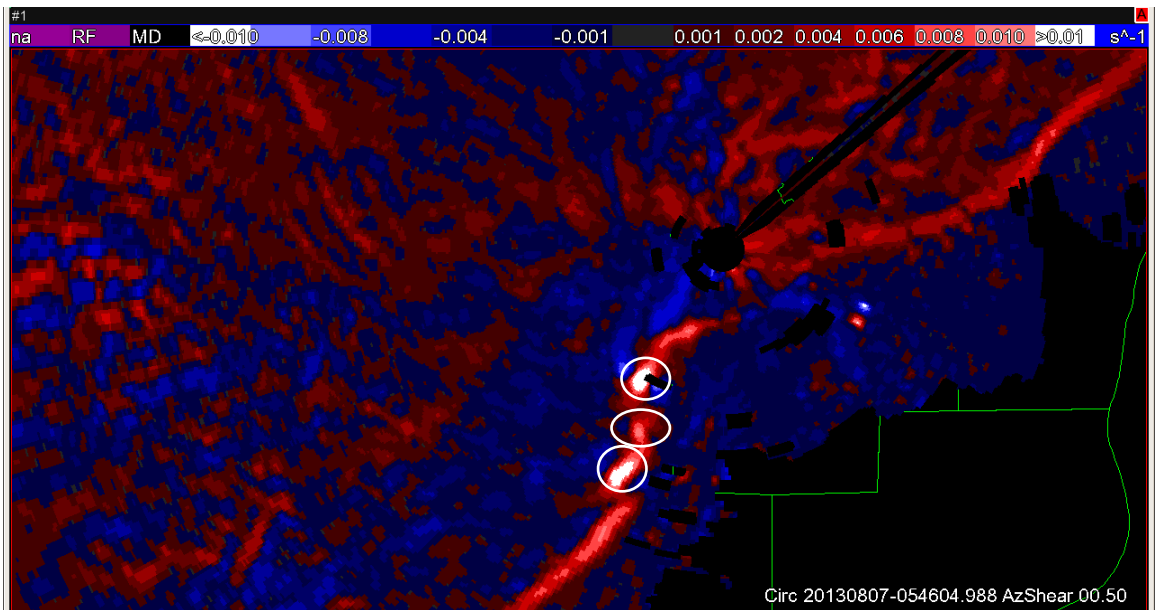


Figure 4.17. Same as Figure 4.13 but at 0546 UTC on 07 August 2013.

The 0550 UTC scan showed a weakening of both tornado 3 and 4 as the reflectivity became more disorganized (Figure 4.18a) and no strong circulation existed at the lowest level (Figure 4.18b). In addition, at this point, the leading edge and the tornadoes were directly parallel with that of the radar beam and only tornado 5 shows up with any real clarity. The issue with tornado 5 is that the location of the tornado is just outside the clutter created near the radar. This is shown in the pixelated reflectivity just north of tornado 5. However, correlation coefficient proved to be useful in this radar scan as it had an area of low to moderate CC, indicating which objects were meteorological and which were non-meteorological objects (Figure 4.18c). The  $Z_{DR}$  in addition showed values near zero at the spot of tornado 5 (Figure 4.18d). Azimuthal shear also showed a strong rotational component that was associated with tornado 5 and tornado 4, while tornado 3 weakened when compared to prior scans (Figure 4.19).

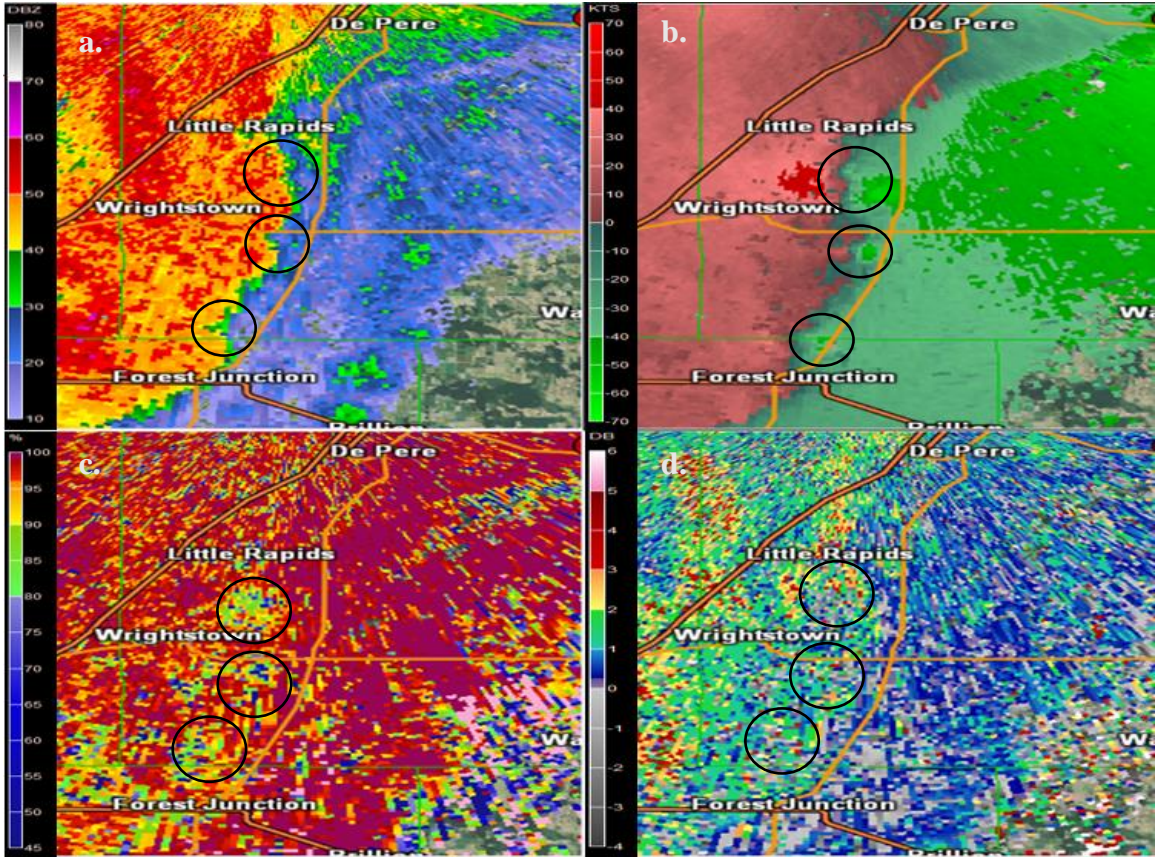


Figure 4.18. Same as Figure 4.9 but at 0550 UTC on 07 August 2013.

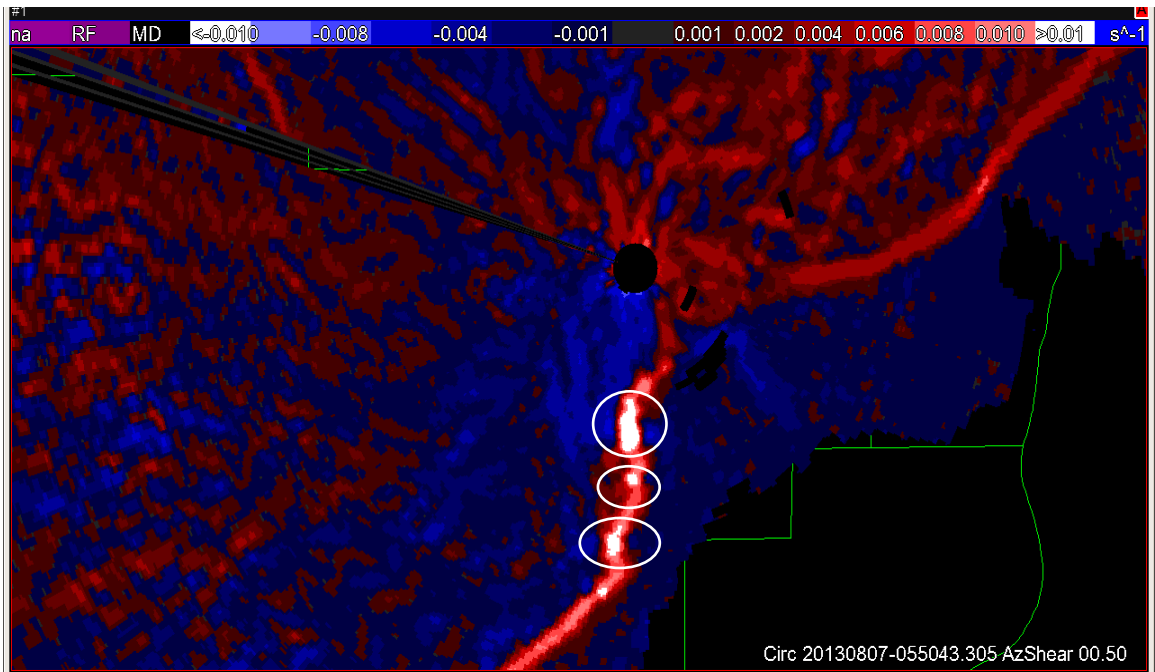


Figure 4.19. Same as Figure 4.13 but at 0550 UTC on 07 August 2013.

Radar scans at 0555 UTC provided little in ways of identifying the location of tornadoes or revealing any new information and have not been included. The scan at 0559 UTC however did reveal some information about the detection and location of the tornadoes. At 0559 UTC, only tornado 5 existed and was severe thunderstorm warned. One thing to note in the reflectivity scan, was that there was a reflectivity ball and inflow flow present that did not exist in the previous scan, evidence that the system may have been cycling (Figure 4.20a). Another thing of note was that just to the north of Langes Corners, WI there was a small reflectivity bulge on the radar. This was a subtle feature seen in the reflectivity, but in storm relative velocity, there existed a weak couplet that could be seen at the same location as the reflectivity location (Figure 4.20b). This is the location of tornado 6 that formed according to the Green Bay WFO. Tornado 6 only lasted for 11 minutes and was rated as an EF1 and was never once warned upon, most likely due to lack of strong tornadic signatures. The location of a potential debris ball for tornado 5 could have been seen in the correlation coefficient as the entire reflectivity ball has lower values than the surrounding area (Figure 4.20c). Even though the radar signatures lacked strong evidence of tornado 6, the azimuthal shear did show the existence of it, like with the prior tornadoes. Just north of tornado 5 was a small area of strong values (Figure 4.21) which was exactly where the tornado occurred. Azimuthal shear also showed for rotational velocities where tornado 3 was, but there was little evidence of this in other radar products and probably was the location of reported straight line wind damage in the area as shown in Figure 4.8.

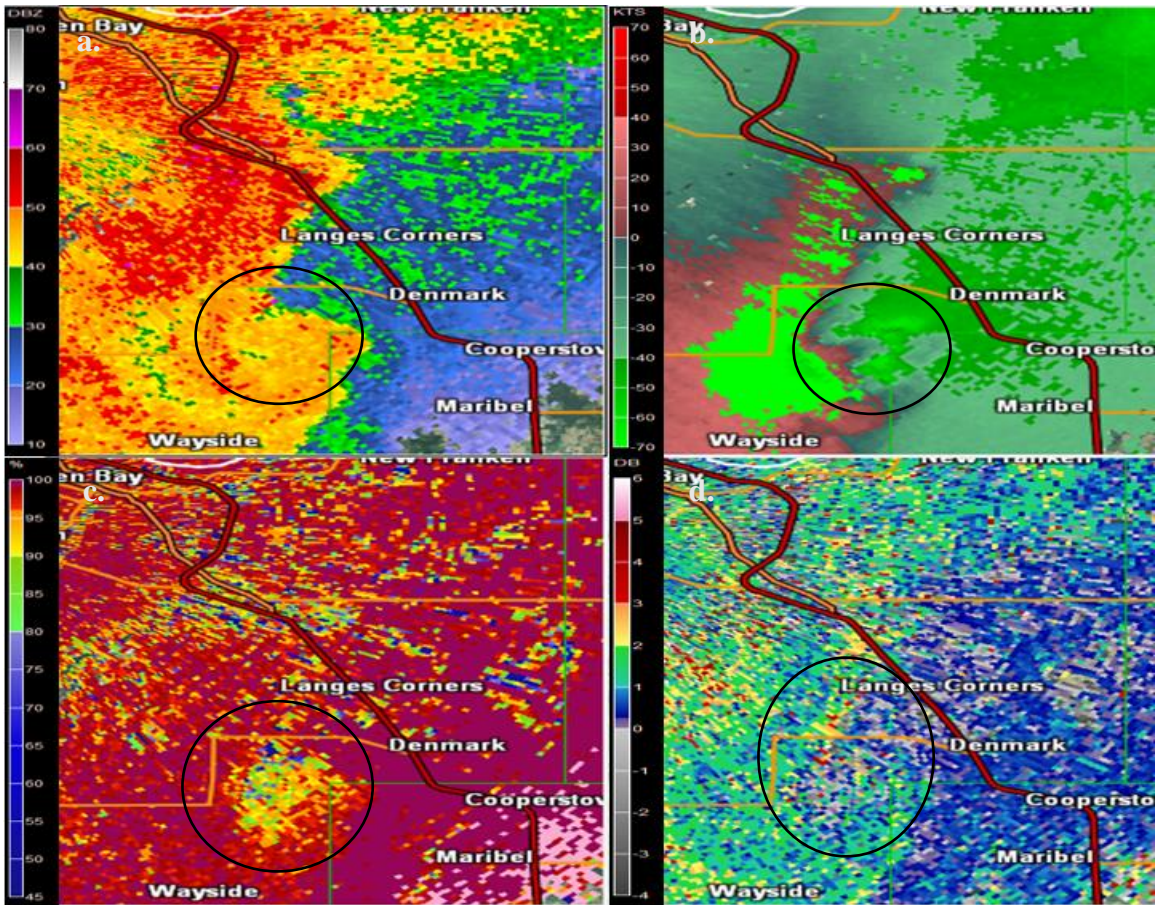


Figure 4.20. Same as Figure 4.9 but at 0559 UTC on 07 August 2013.

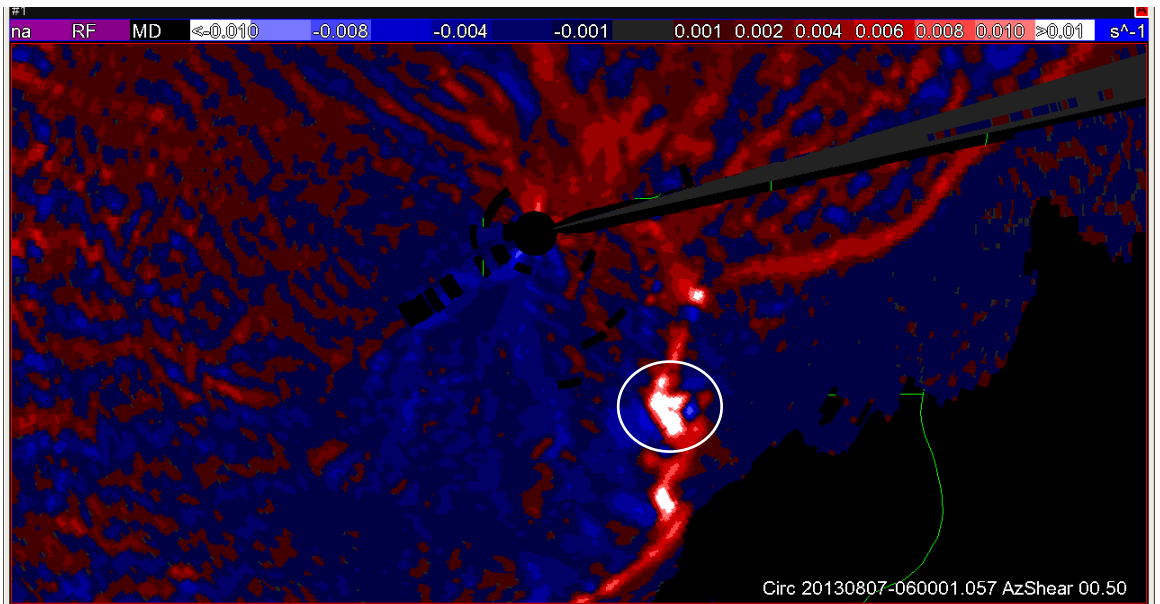


Figure 4.21. Same as Figure 4.13 but at 0600 UTC on 07 August 2013.

Figure 4.22 further shows the motion and movement of the system at 0604 UTC. The debris-like signature continued to be evident in the reflectivity (Figure 4.22a) and in the correlation coefficient (Figure 4.22c) but only for tornado 5. Tornado 6 shows no noticeable differences in the velocity (Figure 4.22b) or correlation scan. The reflectivity scan did show some small inflow region. At the location of tornado 5, values near 0 dB  $Z_{DR}$  existed which might indicate debris. Azimuthal shear continued to be a key aspect in the identification of these area of rotations with stronger signatures than there was seen in the velocity (Figure 4.23). At 0604 UTC, a tornado warning was issued by the Green Bay office over the location of the tornado 5 stating that there was radar indicated rotation. By this time, the tornado had almost completed a 30-mile trek across the CWA. A reason for this late warning may have been due to the timing of the event. Normally, during the day, there would have been people to report these tornadoes but at night, it is much harder to see the tornado. In addition, with multiple wind reports and strong property damage, any reports received might have been attributed to this damage.

In the final radar scan of this event, two distinct inflows appear in reflectivity where these tornadoes were occurring (Figure 4.24a). A lack of vortex coupling in the velocity scan indicated weakening of the system (Figure 4.24b). The sharp definitions of the tornadic signatures were less evident from this time forward. Even CC (Figure 4.24c) and  $Z_{DR}$  showed little in the way of tornadic support (Figure 4.24d). The azimuthal shear (Figure 4.25) still provided evidence of the location of tornado 5 and 6, but also showed the multiple locations of straight line wind that were reported at this, giving azimuthal shear another potential use. Once the system moved out, only stratiform rain remained for a few hours overnight.

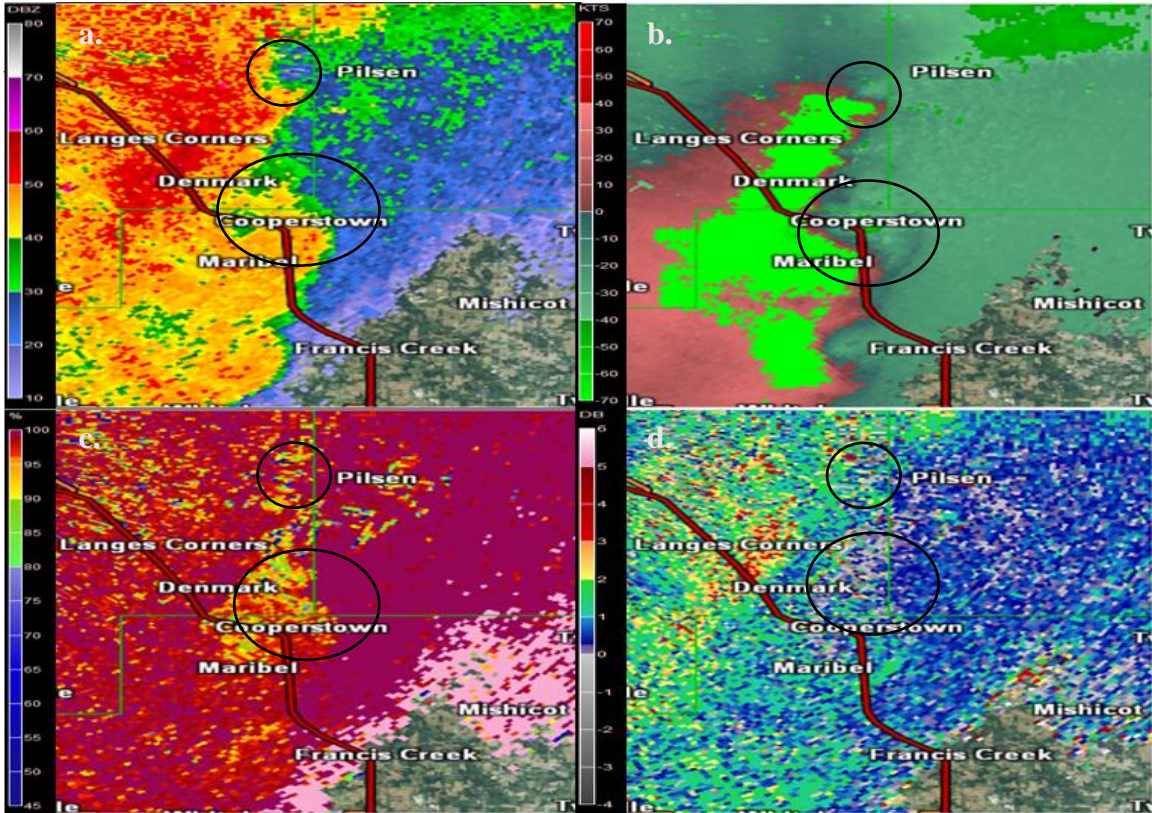


Figure 4.22. Same as Figure 4.9 but at 0604 UTC on 07 August 2013.

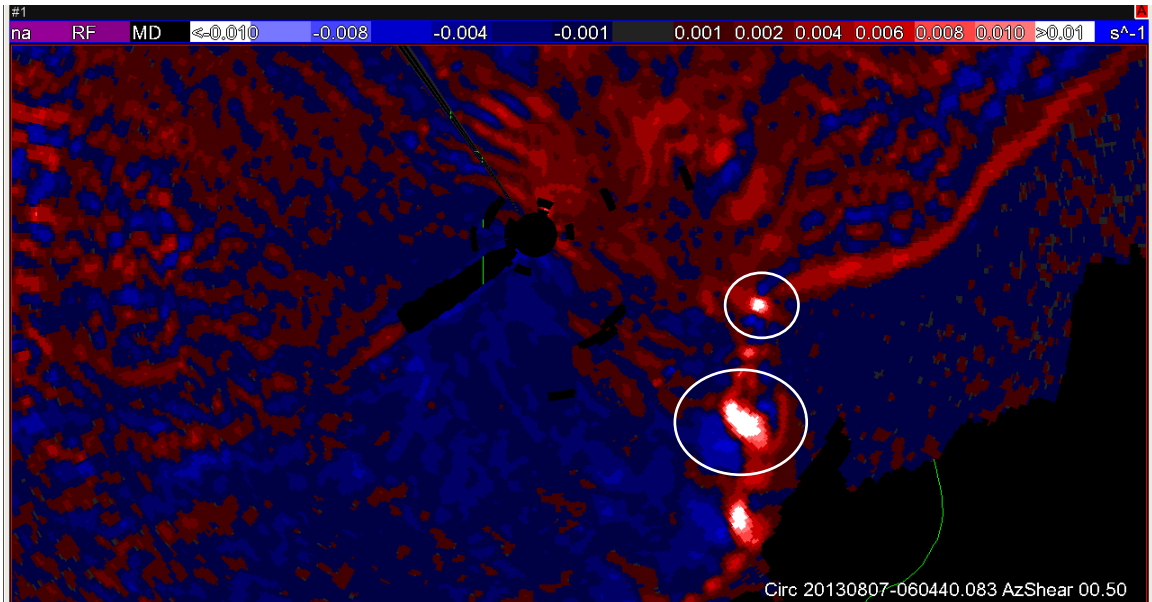


Figure 4.23. Same as Figure 4.13 but at 0604 UTC on 07 August 2013.

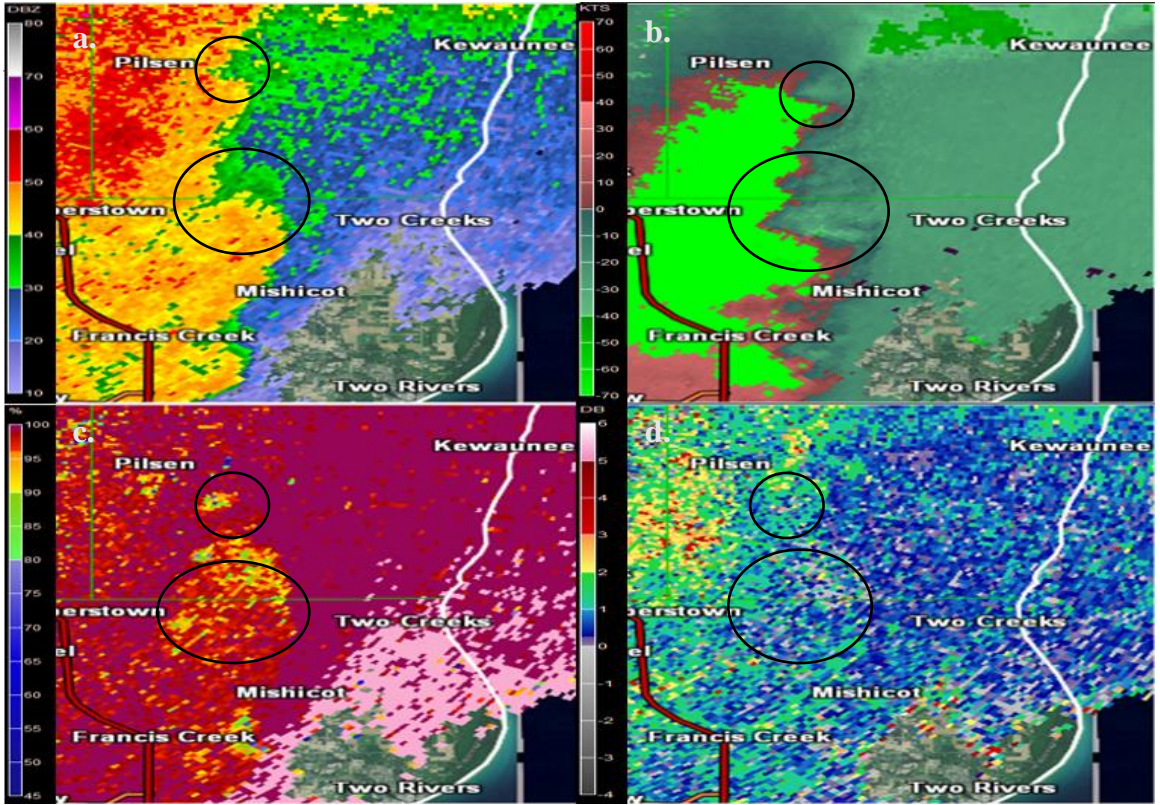


Figure 4.24. Same as Figure 4.9 but at 0609 UTC on 07 August 2013.

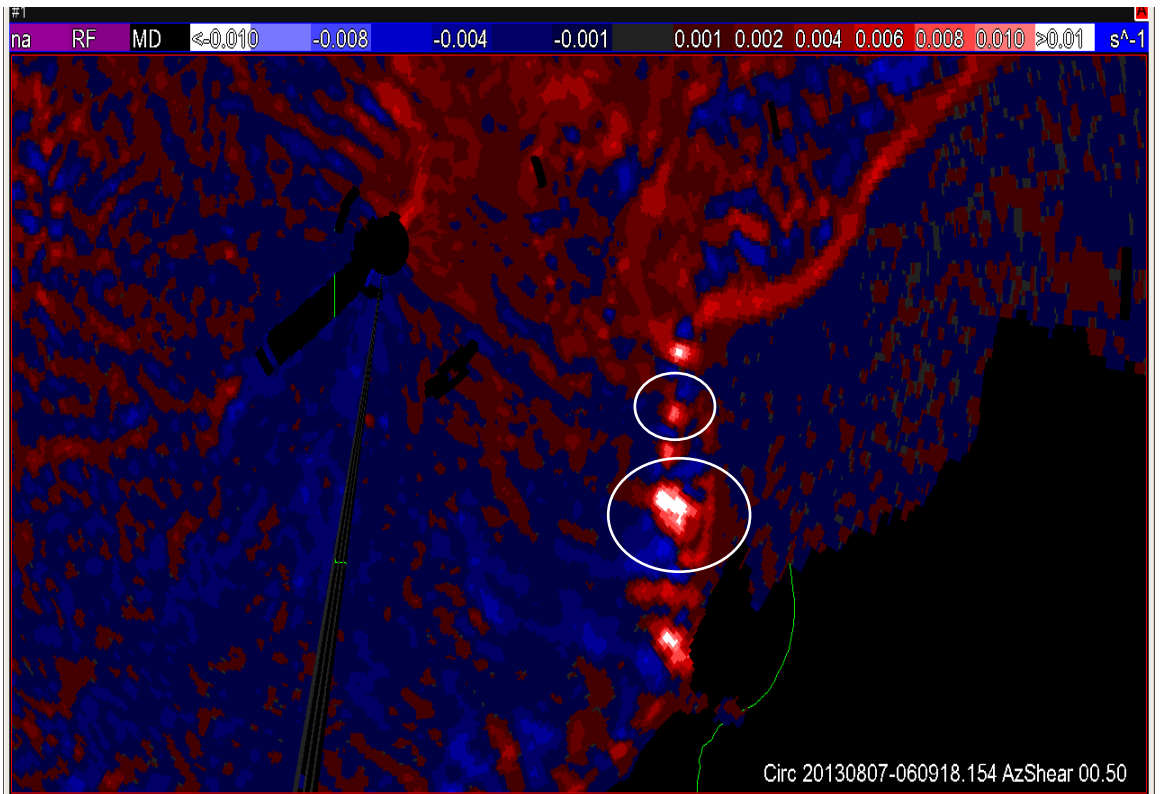


Figure 4.25. Same as Figure 4.13 but at 0609 UTC on 07 August 2013.

## Chapter 5 Results and Discussion

### 5.1 Subjective Evaluation of NSTP

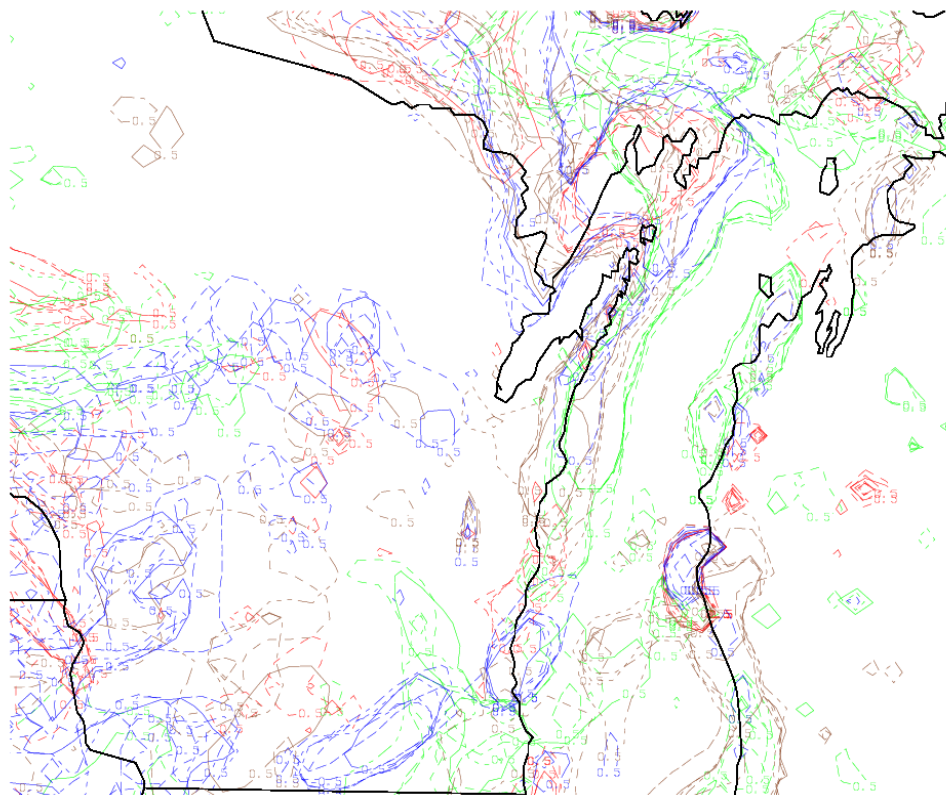
The evaluation of the non-supercell tornado parameter was computed with confidence in the results since the 24 different model runs were run on an identical grid, with only the cumulus and/or microphysical scheme changed. In addition, when comparing to the RUC, the 0000 UTC 07 August 2013 RUC was translated onto the same grid as the WRF models through the use of the GEMPAK command GDMOD. This grid transfer introduced interpolation errors, but to compute statistics, the model solutions being on an identical grid was necessary.

Originally, NSTP values over 1 are considered conditions indicative of regions that are more favorable for NST development, but when basic hit/miss values were calculated, there were less than 10 hits for the entire time analyzed, 0400-0600 UTC, at 13-km out of the 216 potential tornado hit locations. However, SPC on their mesoanalysis page starts to contour the variable when values are more than 0.5. This is most likely done by SPC to raise awareness to the potential of NSTs as any indication for development is better than being caught off guard. Since the preferred threshold was not successful at predicting this event at the standard value, it was lowered to the 0.5 threshold. These results can still be considered valid since SPC uses a lower threshold as well. In addition, the model output does not highlight every area but helps to focus on an area for NST development for forecasters.

In order to establish viability of initial results, a visual analysis of the model simulations was conducted for the times of interest, namely 16-18 hours from the start of the model run on 06 August 2013 at 1200 UTC which corresponds to 0400-0600 UTC on

7 August 2013. This helped keep a short-term focus on the evaluation and coincided with the time that the event moved through the Green Bay CWA. The observational approach was done by breaking the 4 different cumulus schemes in to 4 different colors while the microphysical schemes were broken into 6 different patterns as depicted in Figure 5.1. The microphysical schemes are harder to differentiate between in the figures than the cumulus scheme but the general pattern was observed.

Ensemble solutions at 16 hours out (Figure 5.1), indicated there are not many areas contoured areas within the main region of activity, but this is still before it approached the area with the confirmed tornadoes. It does however show values since some areas contoured are collocated with the location of the convection at the time, west and central Wisconsin. The goal of the ensemble is to determine the pattern based on the individual members. Overall, the Arakawa is the one at this time step that shows the most linear appearance compared to the rest. The Betts-Miller-Janjic, Kain Fritsch, and Grell 3D schemes also depict a similar situation but there are a bit displaced behind the Simplified Arakawa-Schubert CPS.



130807/0400V016 10 M NSTP (X10MM5)

**Figure 5.1. Ensemble of WRF output model solutions at 16 hours out from the model run initialized on 06 August 2013 at 1200 UTC, which relates to 07 August 2013 at 0400 UTC. Values of 0.5 NSTP are contoured. The cumulus parameterization scheme are broken down as followed: red is Kain-Fritsch scheme, green is Betts-Miller-Janjic scheme, blue is Simplified Arakawa-Schubert scheme, and brown is Grell 3d scheme. The microphysical schemes are: solid line is Lin scheme, short dash is WRF Single Moment 5 Class, medium dashed are Ferrier scheme, a long dash and 3 short dashes is WRF Single Moment 6 Class scheme, long dash dot is the Goddard scheme, and long dash three dots is Milbrandt and Yau scheme.**

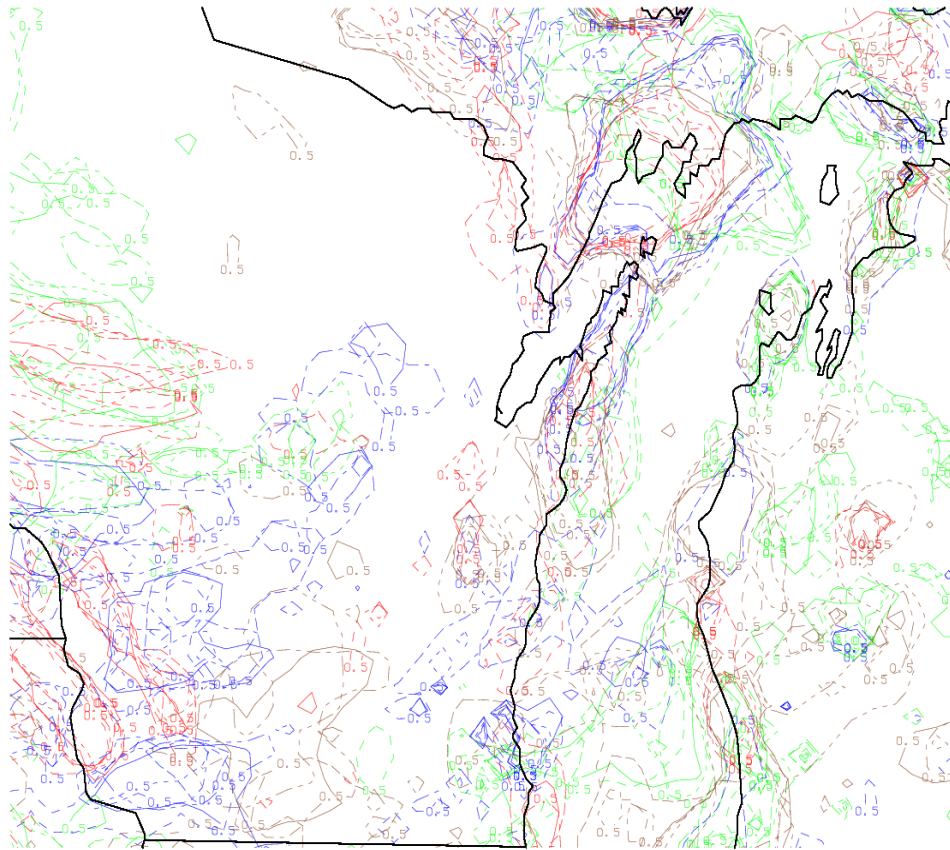


**Figure 5.2.** Same as 5.1 but at 17 hours out from the model run initialized on 06 August 2013 at 1200 UTC.

For the next time evaluated (Figure 5.2), the system began to progress further eastward and the model picks this up. Interestingly, the model ensemble presented two concentrated areas that are of interest for the event. The larger area is the area around the southern edge of the Wisconsin state border. This may be spin up from smaller individual discrete cells that were developing in Iowa at the time and the model is depicting this as a potential region for development. The area is outside the focus of this event, but the ensemble models still showed this as an area of potential NST development. There is a noticeable line of NSTP values of 0.5 along what resembles a leading edge of a QLCS, which further exemplifies that the leading edge is a favorable

region for NST development (Przybylinski 1995; Atkins et al 2005). The Simplified Arakawa-Schubert scheme appears to be the one that is the most consistent between the model configurations to capture this area. Interestingly, there are multiple small contours from a many model configuration just south of Green Bay in roughly the area of the actual recorded tornadoes.

A further evaluation of the geography of the region shows that Lake Winnebago is in that area. As shown in Figure 5.1-5.3, there are large areas of values over 0.5 along the edges of the state and Lake Michigan, in addition to the area around Lake Winnebago. These values most likely occur due to a land/sea breeze that would affect shear within the region, and thus effect vorticity (Springer 2012). Lake Winnebago is 50 km north and south and 10 km east and west. With a grid scale of 13 km, the lake most likely influences the model overall and as a result, can generate values of NSTP when the system is near a lake that is captured on a grid, similar to Lake Michigan (Theeuwes et al. 2010). Forecasters would have to keep in mind where the system is and the local geography to know that these locations can be ignored until it reaches that area.

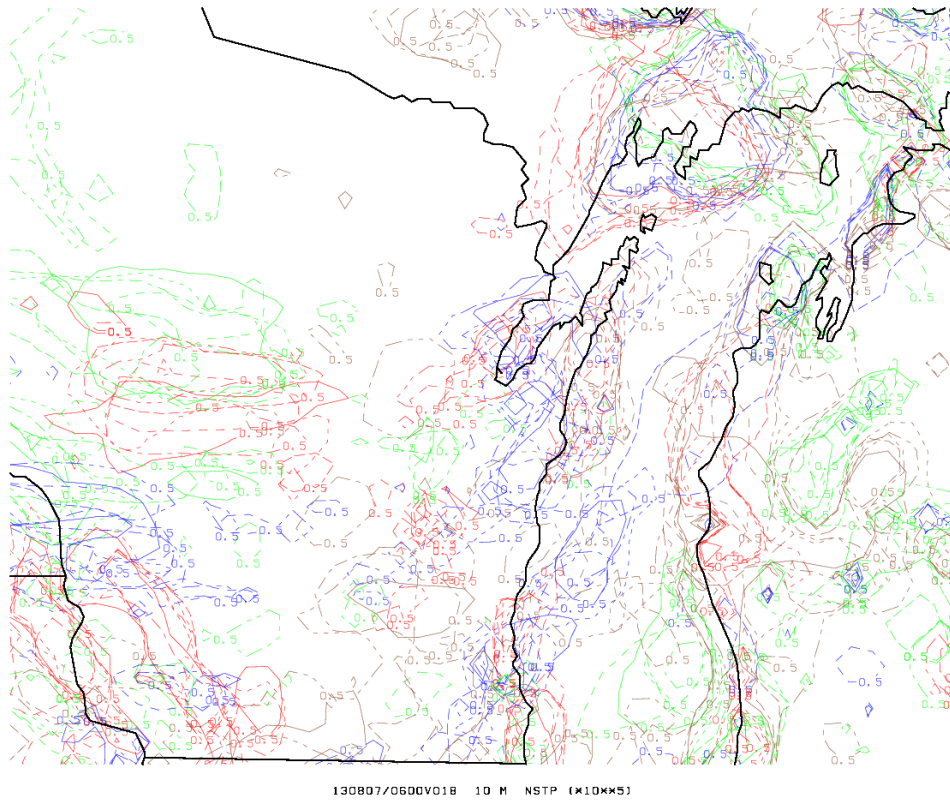


**Figure 5.3.** Same as 5.1 but at 18 hours out from the model run initialized on 06 August 2013 at 1200 UTC.

By 18 hours out, the system should be just south of the peninsula in Wisconsin and more WRF model solutions showed this solution (Figure 5.3). The Simplified Arakawa-Schubert configuration continues to be the one that has the most consistent placement with where the event should be at this time. The Kain-Fritsch and Betts-Miller-Janjic schemes do contour similar areas, but these two microphysical schemes are just now over the point of the first tornadic area indicating that these solutions were moving slower than the actual event. Throughout the 3-hour time window, the Grell 3D schemes seems to have performed with the least skill as it either did not highlight the correct portions or was not highlighted at all.

In addition to the general ensemble model created, the locations of the tornadoes were plotted in three clusters. As shown in the radar analysis, there are three main

locations, which we plotted in Figure 5.4 and 5.5. The 3 locations used, in latitude and longitude, were: 44.34, -88.84 for the farthest west tornado, 44.34, -88.41 for the central tornado, and 44.43, -87.75 for the furthest east tornado. Between the 1<sup>st</sup> and 2<sup>nd</sup> and 2<sup>nd</sup> and 3<sup>rd</sup> points, there is a total of 2 grid point separation and between the 1<sup>st</sup> and 3<sup>rd</sup> point, there is 4 grid points in the distance between them. This means that the spacing between the points does not fully capture a wavelength, but was still able to capture most of the model wave.

With the three tornadoes plotted, the 0.5 NSTP value was used to determine if the tornado occurred within the NSTP value or outside of it. An example of how hit/miss was calculated is now discussed. A hit was counted as when a tornado “point” was within the NSTP contour while a miss had the tornado “point” outside the contour. For each of the 24 configurations, there was a max potential of three hits per configuration, per time step. There were a total of 432 data points. Figure 5.4 shows a hit on the western and eastern tornado location while the central tornado was just outside of the contour. This was done from 15 hours out to 20 hours out from the 06 August 2013 model run at 1200 UTC for the three tornado locations plotted mentioned previously. This time frame was selected for analysis, as 6 hours is a length of a typical watch. If a forecaster had used the parameter, it would update every hour.

A majority of the WRF model solutions were misses, but what Table 5.1 does not show is how close some of the events were. Figure 5.5 shows three areas of the expected value at 18 hours out for the Betts-Miller-Janjic cumulus parameterization scheme and WRF Single Moment 6 Class microphysical scheme. This WRF solution is very close to where NST verification point, but the contoured areas were located too far south to count

as a hit. Overall, during the time frame, only 32 hits were recorded and 400 were misses. This lead to a probability of detection (POD) of 7.41%. Not all misses were as seen in Figure 5.5, as shown in the ensemble product, but the results do not necessarily represent that as well as the ensemble figures, which highlighted the general patterns. Point verification showed very little skill.

**Table 5.1. Total number of hits and misses from 15 hours out to 20 hour from the 1200 UTC 06 August 2013.**

	Forecasts	
	Hit	Miss
Observations	32	400

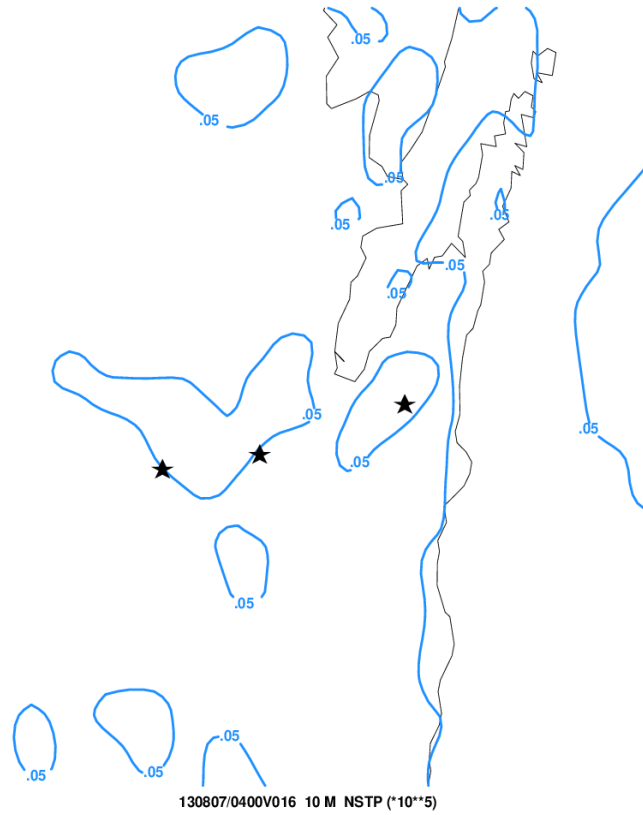


**Figure 5.4. WRF output for the Betts-Miller-Janjic cumulus parameterization scheme and Goddard microphysical scheme combination at 16 hours from the model run on 06 August 2013 at 1200 UTC, which relates to 07 August 2013 at 0400 UTC with NSTP values of 0.5 contoured. This is an example of a hit for one model solution.**

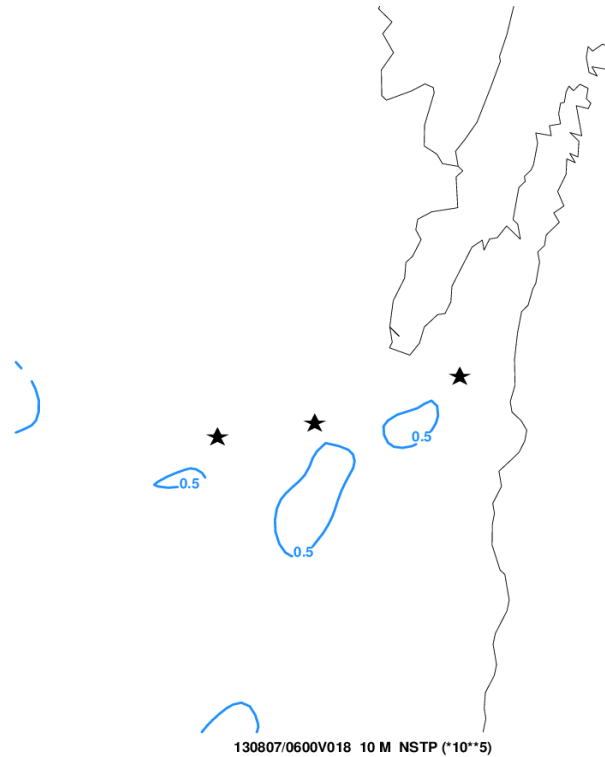


**Figure 5.5. WRF output for the Betts-Miller-Janjic cumulus parameterization scheme and WRF Single Moment 6 Class combination microphysical scheme at 16 hours from the model run on 06 August 2013 at 1200 UTC, which relates to 07 August 2013 at 0600 UTC with NSTP values of 0.5 contoured. This is an example of a miss for one model solution.**

## 5.2 Statistical Verification of NSTP

While the ensemble approached showed some skill, a GEMPAK script was compiled that would allow for each model run to be compared to RUC model. Since the RUC was converted to be on the same grid as the model solutions, this allows for an easy comparison. If an event occurred on the RUC initial field, a good WRF solution would also have it occurring at the same location, leading to strong statistical evidence. A GEMPAK script was written to find correlation, hits, POD, FAR, CSI, and bias and was compared to the RUC initial field which was treated as truth. The results presented here are grouped by the cumulus scheme used with the results for the microphysics shown

**Table 5.2a. Kain Fritsch cumulus scheme results categorized into the 6 microphysical schemes at 0400 UTC on 07 August 2013 from the 1200 UTC 06 August 2013 model run 16 hours out.**

	<b>Correlation</b>	<b>Hit</b>	<b>POD</b>	<b>FAR</b>	<b>CSI</b>	<b>Bias</b>
<b>Lin</b>	-0.14	34	0.09	0.76	0.07	0.37
<b>WSM 5</b>	-0.29	35	0.09	0.73	0.08	0.33
<b>Ferrier</b>	-0.17	33	0.09	0.74	0.07	0.33
<b>WRF 6</b>	-0.01	41	0.11	0.63	0.09	0.29
<b>Goddard</b>	-0.23	43	0.11	0.66	0.09	0.33
<b>MY</b>	-0.23	32	0.08	0.66	0.07	0.24

**Table 5.2b. Betts-Miller-Janjic cumulus scheme results categorized into the 6 microphysical schemes at 0400 UTC on 07 August 2013 from the 1200 UTC 06 August 2013 model run 16 hours out.**

	<b>Correlation</b>	<b>Hit</b>	<b>POD</b>	<b>FAR</b>	<b>CSI</b>	<b>Bias</b>
<b>Lin</b>	0.03	64	0.17	0.76	0.11	0.70
<b>WSM 5</b>	0.09	46	0.12	0.79	0.08	0.57
<b>Ferrier</b>	0.05	58	0.15	0.80	0.09	0.74
<b>WRF 6</b>	0.09	33	0.09	0.84	0.06	0.55
<b>Goddard</b>	0.09	49	0.13	0.78	0.09	0.58
<b>MY</b>	0.05	37	0.10	0.82	0.07	0.52

**Table 5.2c. Simplified Arakawa-Schubert cumulus scheme results categorized into the 6 microphysical schemes at 0400 UTC on 07 August 2013 from the 1200 UTC 06 August 2013 model run 16 hours out.**

	<b>Correlation</b>	<b>Hit</b>	<b>POD</b>	<b>FAR</b>	<b>CSI</b>	<b>Bias</b>
<b>Lin</b>	0.01	56	0.14	0.77	0.10	0.62
<b>WSM 5</b>	-0.03	63	0.16	0.74	0.11	0.64
<b>Ferrier</b>	-0.10	77	0.20	0.73	0.13	0.74
<b>WRF 6</b>	0.01	67	0.17	0.75	0.11	0.68
<b>Goddard</b>	-0.06	67	0.17	0.77	0.11	0.76
<b>MY</b>	0.06	66	0.17	0.74	0.11	0.67

**Table 5.2d. Grell 3D cumulus scheme results categorized into the 6 microphysical schemes at 0400 UTC on 07 August 2013 from the 1200 UTC 06 August 2013 model run 16 hours out.**

	<b>Correlation</b>	<b>Hit</b>	<b>POD</b>	<b>FAR</b>	<b>CSI</b>	<b>Bias</b>
<b>Lin</b>	-0.10	34	0.09	0.84	0.06	0.54
<b>WSM 5</b>	0.03	32	0.08	0.86	0.05	0.60
<b>Ferrier</b>	0.10	62	0.16	0.71	0.11	0.54
<b>WRF 6</b>	-0.09	32	0.08	0.84	0.06	0.52
<b>Goddard</b>	-0.03	30	0.08	0.84	0.05	0.50
<b>MY</b>	-0.15	26	0.07	0.88	0.04	0.57

individually. However, each microphysical scheme is in the same location on each table allow for analysis of the cumulus scheme performance results as well.

The results of the model run statistics analyzed are shown in Table 5.2 a-d for the 16 hour WRF solutions. This time step is from the 1200 UTC model run on 06 August 2013 at 04 UTC when the QLCS was still on the border of the CWA. The results show a low correlation between all 24 members with most values near zero. The solutions do however show that there are some values to hit but with the current analysis, there is no way to know the location of the hits that correspond. As shown in the ensemble region, this could potentially be the areas located on the coast. The major take away from this time step is that POD and CSI are low with a high FAR for all the model configurations. The bias values are low which indicate that the event is under forecasting, which is confirmed in the ensemble figures. The greatest number of hits occurred in the Simplified Arakawa-Schubert cumulus scheme which was also noted as consistently being the solution that matches what the actual event reproduced. There was no microphysical scheme that seemed to perform better than any other.

**Table 5.3a. Kain Fritsch cumulus scheme results categorized into the 6 microphysical schemes at 0500 UTC on 07 August 2013 from the 1200 UTC 06 August 2013 model run 17 hours out**

	<b>Correlation</b>	<b>Hit</b>	<b>POD</b>	<b>FAR</b>	<b>CSI</b>	<b>Bias</b>
<b>Lin</b>	0.16	39	0.10	0.72	0.08	0.38
<b>WSM 5</b>	0.19	40	0.11	0.73	0.08	0.40
<b>Ferrier</b>	-0.08	27	0.07	0.78	0.06	0.33
<b>WRF 6</b>	-0.05	34	0.09	0.71	0.07	0.31
<b>Goddard</b>	0.01	52	0.14	0.68	0.11	0.44
<b>MY</b>	-0.05	38	0.10	0.66	0.09	0.30

**Table 5.3b. Betts-Miller-Janjic cumulus scheme results categorized into the 6 microphysical schemes at 0500 UTC on 07 August 2013 from the 1200 UTC 06 August 2013 model run 17 hours out.**

	<b>Correlation</b>	<b>Hit</b>	<b>POD</b>	<b>FAR</b>	<b>CSI</b>	<b>Bias</b>
<b>Lin</b>	0.13	53	0.14	0.78	0.09	0.66
<b>WSM 5</b>	0.19	64	0.17	0.73	0.12	0.63
<b>Ferrier</b>	-0.00	41	0.11	0.83	0.07	0.63
<b>WRF 6</b>	0.28	56	0.15	0.76	0.10	0.62
<b>Goddard</b>	0.29	45	0.12	0.81	0.08	0.63
<b>MY</b>	0.15	27	0.07	0.86	0.05	0.53

**Table 5.3c. Simplified Arakawa-Schubert cumulus scheme results categorized into the 6 microphysical schemes at 0500 UTC on 07 August 2013 from the 1200 UTC 06 August 2013 model run 17 hours out.**

	<b>Correlation</b>	<b>Hit</b>	<b>POD</b>	<b>FAR</b>	<b>CSI</b>	<b>Bias</b>
<b>Lin</b>	0.11	50	0.13	0.75	0.1	0.53
<b>WSM 5</b>	0.02	33	0.09	0.79	0.07	0.42
<b>Ferrier</b>	0.07	62	0.17	0.76	0.11	0.69
<b>WRF 6</b>	-0.02	51	0.14	0.77	0.09	0.61
<b>Goddard</b>	-0.03	55	0.15	0.77	0.10	0.64
<b>MY</b>	0.26	48	0.13	0.73	0.10	0.48

**Table 5.3d. Grell 3D cumulus scheme results categorized into the 6 microphysical schemes at 0500 UTC on 07 August 2013 from the 1200 UTC 06 August 2013 model run 17 hours out.**

	<b>Correlation</b>	<b>Hit</b>	<b>POD</b>	<b>FAR</b>	<b>CSI</b>	<b>Bias</b>
<b>Lin</b>	0.04	14	0.04	0.94	0.02	0.59
<b>WSM 5</b>	0.04	6	0.02	0.98	0.01	0.67
<b>Ferrier</b>	0.08	44	0.11	0.76	0.08	0.49
<b>WRF 6</b>	-0.00	18	0.05	0.93	0.03	0.65
<b>Goddard</b>	0.03	27	0.07	0.89	0.05	0.67
<b>MY</b>	0.01	37	0.10	0.87	0.06	0.77

The expectation in Tables 5.3 a-d is that they will correspond with higher values since this the time that the event has started, but that is not entirely true. While there are more hits in some of the schemes, the POD does not get above 0.34 in all but one case, the Kain Fritsch/Milbrandt and Yau combination, and this configuration is only has 34

hits, a low correlation, bias and CSI meaning that the results could be better. In the BMJ and Grell 3d cumulus schemes, the results are some of the least skilled. There is no distinct pattern of which microphysical scheme was the most skilled at predicting the results, as it would perform well in one cumulus scheme and perform poorly in another one. The cumulus parameterization scheme also show no improvement from the last time step but both the Kain Fritsch and Simplified Arakawa-Schubert cumulus parameterization schemes have PODs above .2 which shows some skill in detecting areas of NST of 0.5 or greater. However, the CSI is still very low, with no value greater than 0.12, indicating little skill in the forecast. Since NSTs are a low predictability event, the low scores reflect that, especially when dealing with point forecast verification.

The final time frame of interest of the event that was analyzed was at 0600 UTC on 07 August 2013 which was 18 hours out from the start of the model run initialized on 06 August 2013 at 1200 UTC. This time yielded similar results when compared to the other two time steps as shown in Table 5.4 a-d. Throughout the entire time analyzed, the Grell 3D cumulus parameterization scheme and Milbrandt and Yau microphysical scheme showed the least skill of the 4 cumulus schemes and 6 microphysical schemes respectively. However, at this time step, Table 5.4 a, the Kain Fritsch cumulus parameterization scheme showed an improvement of skill as correlations start to reach a higher positive value, POD is increased, and CSI got as high as .15. This is the highest value of CSI that was found for all time steps. Even though the event is better forecasted at this point, the bias is still low and is still under-forecasting.

**Table 5.4a. Kain Fritsch cumulus scheme results categorized into the 6 microphysical schemes at 0600 UTC on 07 August 2013 from the 1200 UTC 06 August 2013 model run 18 hours out.**

	<b>Correlation</b>	<b>Hit</b>	<b>POD</b>	<b>FAR</b>	<b>CSI</b>	<b>Bias</b>
<b>Lin</b>	0.32	59	0.18	0.64	0.14	0.52
<b>WSM 5</b>	0.25	60	0.19	0.69	0.13	0.60
<b>Ferrier</b>	0.22	51	0.16	0.68	0.12	0.50
<b>WRF 6</b>	0.25	46	0.14	0.73	0.10	0.52
<b>Goddard</b>	0.29	68	0.21	0.67	0.15	0.64
<b>MY</b>	0.03	40	0.12	0.76	0.09	0.52

**Table 5.4b. Betts-Miller-Janjic cumulus scheme results categorized into the 6 microphysical schemes at 0600 UTC on 07 August 2013 from the 1200 UTC 06 August 2013 model run 18 hours out.**

	<b>Correlation</b>	<b>Hit</b>	<b>POD</b>	<b>FAR</b>	<b>CSI</b>	<b>Bias</b>
<b>Lin</b>	-0.05	43	0.13	0.81	0.09	0.69
<b>WSM 5</b>	-0.07	55	0.17	0.75	0.11	0.68
<b>Ferrier</b>	-0.07	57	0.18	0.75	0.11	0.72
<b>WRF 6</b>	-0.05	57	0.18	0.75	0.12	0.70
<b>Goddard</b>	-0.01	43	0.13	0.81	0.08	0.72
<b>MY</b>	-0.00	36	0.11	0.83	0.07	0.64

**Table 5.4c. Simplified Arakawa cumulus scheme results categorized into the 6 microphysical schemes at 0600 UTC on 07 August 2013 from the 1200 UTC 06 August 2013 model run 18 hours out.**

	<b>Correlation</b>	<b>Hit</b>	<b>POD</b>	<b>FAR</b>	<b>CSI</b>	<b>Bias</b>
<b>Lin</b>	-0.05	34	0.11	0.80	0.07	0.52
<b>WSM 5</b>	-0.05	24	0.07	0.84	0.05	0.47
<b>Ferrier</b>	-0.14	32	0.10	0.83	0.07	0.59
<b>WRF 6</b>	-0.05	30	0.09	0.84	0.06	0.57
<b>Goddard</b>	-0.09	14	0.04	0.93	0.02	0.59
<b>MY</b>	0.02	35	0.11	0.77	0.08	0.48

**Table 5.4d. Grell 3D cumulus scheme results categorized into the 6 microphysical schemes at 0600 UTC on 07 August 2013 from the 1200 UTC 06 August 2013 model run 18 hours out.**

	<b>Correlation</b>	<b>Hit</b>	<b>POD</b>	<b>FAR</b>	<b>CSI</b>	<b>Bias</b>
<b>Lin</b>	0.11	27	0.08	0.90	0.04	0.80
<b>WSM 5</b>	-0.09	15	0.05	0.94	0.05	0.74
<b>Ferrier</b>	0.01	7	0.02	0.94	0.01	0.38
<b>WRF 6</b>	0.07	31	0.10	0.88	0.06	0.83
<b>Goddard</b>	-0.06	14	0.04	0.94	0.03	0.75
<b>MY</b>	0.09	50	0.16	0.85	0.08	1.05

If the research conducted here was based solely on statistics, it would support the idea that the nonsupercell tornado parameter is not a good tool for a forecaster to use due to the statistical evidence that it accurately handled the event. In addition, the value had to be lower to 0.5 and did not match with Baumgardt and Cook (2006) value of 1.

However, SPC uses the parameter and does start to denote values at 0.5 and above

allowing for this research to still hold validity. In addition, outside of the initial research discussed by Caruso and Davies (2005) and Baumgardt and Cook (2006), little research has been conducted on this parameter. When all the WRF model runs are placed into an ensemble image, as in Figure 5.1-3, there does appear to be some pattern and areas of concern are highlighted for forecasters. As with most parameter, the NSTP is simply another method to allow for a conditional diagnosis of the potential for non-supercell tornadic activity. These results however are limited in scope as the research only deals with one event. The ensemble approach may look like this on other QLCS event, so more research is needed to further the understanding of the NSTP on a variety of QLCSs.

## Chapter 6 Conclusions

### 6.1 Summary

The main objective for this study was to evaluate the usefulness of the Nonsupercell Tornado Parameter established by Baumgardt and Cook (2006). The parameter does not have much research associated with it but is currently in use by the Storm Prediction Center. The effort here was to add more literature to the community and show a new way that the parameter could be used in forecasting.

An extensive case analysis was conducted for a tornadic event in Green Bay, Wisconsin on 07 August 2013 that produced 6 NST tornadoes along with straight line wind damage. The system that moved through at 0500 UTC was a part of a QLCS that had formed and produced wind, hail and tornado damage in the Dakotas and Minnesota prior to reaching the area of interest. A synoptic analysis showed an environment capable of producing severe weather as there was sufficient omega, enough CAPE to provide energy, and enough shear to support straight line winds along a leading edge. An analysis of the RUC with the NST parameter showed values over 0.5, which is the minimum threshold set forth by SPC, by 0600 UTC. This was a bit slower than the actual time of the event by 40 minutes, but still highlighted the region of concern.

Evaluation of the event using WSR-88D radar and subsequent derived products showed that tornadoes were detectable and could have been warned more efficiently. Radar analysis showed the NSTs developed along the leading edge, which is consistent with prior research (Pryzblynski 1995; Funk et al. 1999; Atkins et al. 2005). There were weak but distinct couplets that formed in the lowest elevation scan, which was consistent

with Atkins et al. (2004; 2005) as NST tend not to extend high into the atmosphere. The use of dual-pol products helped to further confirm the NST existence and location.

In addition to the basic dual-polarization products, azimuthal shear was another tool that proved useful for detecting tornadic signatures. Azimuthal shear was shown by Davis and Parker (2014) to identify features in supercell tornadoes and differentiate between tornado and nontornado producing vortices. The findings presented here show that there is viability for the use of azimuthal shear in this situation as values were above the  $0.01 \text{ s}^{-1}$  threshold, which is an indicator of strong rotation. For the times that data existed, it was useful in further confirming the location of the tornadoes. The usefulness of azimuthal shear was evident as the product helped identify the three tornadoes when they were occurring simultaneously. The azimuthal shear showed skill in assessing NSTs and findings here are one of the first to use the product in a NST environment.

When evaluating the NST parameter after establishing an ensemble model approach with 24 varied cumulus parameterizations and/or microphysical scheme, the subjective approach shows areas of interest in relation to the actual event when compared to the RUC initial fields. While not all the models performed well from a visual aspect, the fact remains that some models did highlight areas of NST values greater than 0.5. Even though the WRF model solution output was somewhat displaced from the actual event, the knowledge that the model could predict an environment favorable for NST is still useful to forecasters.

To achieve workable results from a statistical standpoint, the NSTP value was lowered. In a statistical evaluation, all WRF model solutions at the three primary time steps performed poorly. There appeared to be little skill associated with the actual results

when compared to the RUC initialized field in the section 5.2. At the spatial scale of 13 km, the cumulus parameterization scheme was better at representing the event than the microphysical schemes, which tend to work better at scales less than 9 km. Overall, statistically, the results do not suggest that the parameter is useful while a subjective, visual approach is more supportive of the parameter's usefulness. In this case study, values of higher NSTP appeared near lake shore edges. This could have led to false positives in the data, but a skilled forecaster would ignore the shore of Lake Michigan and instead focus on the line of storms approaching.

The nonsupercell tornado parameter is simply another tool that exists to aid forecasters and research from Baumgardt and Cook (2006) and the parameter's implementation at SPC, shows that it is perceived to have value in the forecasting community. The results presented here is one of the first, to the author's knowledge, to extensively look at and evaluate the parameter not only in a model setting, but also as an assessment to the parameter beyond what Baumgardt and Cook (2006) proposed. The results here show a potential usefulness for the parameter as it did highlight area of concern even if it did not have pinpoint accuracy. Knowing that the potential for a nonsupercell tornado to form is useful for a forecaster. The statistics however support that the parameter has little skill as an objective forecasting tool. While tornadogenesis in a supercell is better understood than the nonsupercell tornadogenesis, any tool that might prove useful to help alert a forecaster in advance and the parameter may have simply not performed well with this case, but there is not enough evidence to dismiss the NSTP from the forecasting community.

## 6.2 Future Work

There are few areas that the research presented here could be further expanded upon. One area that of possible improvement is the use of more cases. While the use of 24 cases creates an ensemble, the use of more events would allow for a better understanding of the mechanisms of the event and perhaps create improved results. One event that would be of use would be the idealistic event that Caruso and Davies (2005) establish, which is a slow moving stationary front compared to the faster moving cold front presented here. More events could also be used to create another ensemble approach to more accurately establish and depict which variables within the equation are the strongest factor dependent on season and region. By taking this approach, forecasters could have a more elaborate and refined parameter that works best for them and their needs.

Another area could be improved is model resolution. By working on a smaller scale that more accurately represents the size of a nonsupercell tornado, the forecasting skill might be improved. The suggested size would be less than 1 km. With this small size, the small scales features that affect nonsupercell tornado development could be better captured such as shear, vorticity, and the inflow/outflow relationship. Based on the literature analyzed here, these appear to be the biggest influences in NST development and research coupled with the NST parameter could help further improve the usefulness of the parameter.

## References

- Atkins, N. T., J. M. Arnott, R. W. Przybylinski, R. A. Wolf, and B. D. Ketcham, 2004: Vortex structure and evolution within bow echoes. Part I: Single-Doppler and damage analysis of the 29 June 1998 derecho. *Mon. Wea. Rev.*, **132**, 2224–2242.
- Atkins, N. T., C. S. Bouchard, R. W. Przybylinski, R. J. Trapp, and G. Schmocker, 2005: Damaging surface wind mechanism within the 10 June 2003 Saint Louis bow echo during BAMEX. *Mon. Wea. Rev.*, **133**, 2275–2296.
- Atkins, N. T., and M. St. Laurent, 2009: Bow echo mesovortices. Part I: Processes that influence their damaging potential. *Mon. Wea. Rev.*, **137**, 1497–1513.
- Atkins, N. T., and M. St. Laurent, 2009: Bow echo mesovortices. Part II: Their Genesis. *Mon. Wea. Rev.*, **137**, 1514–1532.
- Baumgardt, D. A., and K. Cook, 2006: Preliminary evaluation of a parameter to forecast environments conducive to non-mesocyclone tornadogenesis. *23rd Conf. of Severe Local Storms*, St. Louis, MO, Amer. Meteor. Soc., 12.1. [Available online at <http://www.wdtb.noaa.gov/courses/MRMS/ProductGuide/SevereWeather/azimuthal-shear.php>]
- Caruso, J. M., and J. M. Davies, 2005: Tornadoes in nonmesocyclone environments with pre-existing vertical vorticity along convergence boundaries. *Electron. J. Oper. Meteor.*, **6** (4), 1–36. [Available online at <http://www.nwas.org/ej/pdf/2005-EJ4.pdf>.]
- Davis, J. M and M. D. Parker, 2014: Radar Climatology of Tornadic and Nontornadic Vortices in High-Shear, Low-CAPE Environments in the Mid-Atlantic and Southeastern United States. *Wea. and Forecasting*, **29**, 828-853.
- Dulière, V., Zhang, Y., and E. P. Salathé Jr, 2011: Extreme precipitation and temperature over the US pacific northwest: a comparison between observations, reanalysis data, and regional models. *J. of Clim.*, **24**, 1950-1964.
- Fujita, T. T., 1978: Manual of downburst identification for project Nimrod. Satellite and Mesometeorology Research Paper 156, Dept. of Geophysical Sciences, University of Chicago, 104 pp. [NTIS PB-286048.].
- Funk, T. W., K. E. Darmofal, J. D. Kirkpatrick, V. L. DeWald, R. W. Przybylinski, G. K. Schmocker, and Y-J. Lin, 1999: Storm reflectivity and mesocyclone evolution associated with the 15 April 1994 squall line over Kentucky and southern Indiana. *Wea. Forecasting*, **14**, 976–993.
- Johns, R. H., and W. D. Hirt, 1987: Derechos: Widespread convectively induced windstorms. *Wea. Forecasting*, **2**, 32–49.

- Kis, A. K., and J. M. Straka, 2009: Nocturnal tornado climatology. *Wea. Forecasting*, **25**, 545–561.
- Kong, F., K. K. Droegemeier, and N. L. Hickmon, 2006: Multiresolution ensemble forecasts of an observed tornadic thunderstorm system. Part I: Comparison of coarse and fine-grid experiments. *Mon. Wea. Rev.*, **134**, 807–833.
- Lee, B. D., and R. B. Wilhelmson. 2000: The Numerical Simulation of Nonsupercell Tornadogenesis. Part III: parameter tests investigating the role of CAPE, vortex sheet strength and boundary layer vertical shear. *J. Atmos. Sci.*, **57**, 2246–2261.
- Lorenz, E. N., 1969: Atmospheric predictability as revealed by naturally occurring analogues. *J. Atmos. Sci.*, **26**, 636–646.
- Markowski, P. M., and Y. P. Richardson, 2014: The influence of environmental low-level shear and cold pools on tornadogenesis: Insights from idealized simulations. *J. Atmos. Sci.*, **71**, 243–275.
- McCormack, P. D., 2012: *Vortex, molecular spin and nanovorticity: an introduction*. Springer Verlag, New York.
- Przybylinski, R. W., 1995: The bow echo: Observations, numerical simulations, and severe weather detection methods. *Wea. Forecasting*, **10**, 203–218.
- Przybylinski, R. W., J. Sieveking, and G. Schmocker, 2013: Classification of Quasi Linear Convective Systems (QLCS) (Including embedded Bow Echoes within QLCSs) and mesovortex characteristics across WFO St. Louis County Warning Area (CWA) and surrounding CWAs. Accessed 4 October 2016. [Available online at <https://www.weather.gov/lx/qlcslatest>.]
- Rasmussen, E. N., 2003: Refined supercell and tornado forecast parameters. *Wea. Forecasting*, **18**, 530–535.
- Romine, G. S., Burgess, D. W., and Wilhelmson, R. B. 2008: A dual-polarization-radar-based assessment of the 8 May 2003 Oklahoma City area tornadic supercell. *Mon. Wea. Rev.*, **136**, 2849–2870.
- Rotunno, R. J., B. Klemp, and M. L. Weisman, 1988: A theory for strong, long-lived squall lines. *J. Atmos. Sci.*, **45**, 463–485.
- Smull, B.F., and R. A. Houze Jr., 1987: Rear inflow in squall lines with trailing stratiform precipitation. *Mon. Wea. Rev.*, **115**, 2869–2889.

- Stensrud, D. J., J. W. Bao, and T. T. Warner, 2000: Using initial condition and model physics perturbations in short-range ensemble simulations of mesoscale convective systems. *Mon. Wea. Rev.*, **128**, 2077–2107.
- Tapiador, F. J., 2010: A joint estimate of the precipitation climate signal in Europe using eight regional models and five observational datasets. *J. Climate*, **23**, 1719–1738.
- Theeuwes, N. E., G. J. Steeneveld, F. Krikken, and A. A. M. Holtslag, 2010: Mesoscale modeling of lake effect snow over Lake Erie – sensitivity to convection, microphysics and the water temperature. *Advances in Science and Research*, **4**, 15–22.
- Thompson, R. L., R. Edwards, and J. A. Hart, 2002: Evaluation and interpretation of the supercell composite and significant tornado parameters at the Storm Prediction Center. Preprints, 21st Conf. on Severe Local Storms/19th Conf. on Weather Analysis and Forecasting/15th Conf. on Numerical Weather Prediction, San Antonio, TX, Amer. Meteor. Soc., J3.2. [Available online at <https://ams.confex.com/ams/pdfpapers/46942.pdf>.]
- Trapp, R. J., and M. L. Weisman, 2003: Low-level mesovortices within squall lines and bow echoes. Part II: Their genesis and implications. *Mon. Wea. Rev.*, **131**, 2804–2823.
- Trapp, R. J., S. A. Tessendorf, E. S. Godfrey, and H. E. Brooks. 2005: Tornadoes from squall Lines and bow Echoes part I: climatological distribution. *Wea. Forecasting*, **20**, 23–34.
- Trapp, R. J., E. D. Mitchell, G. A. Tipton, D. W. Effertz, A. I. Watson, D. L. Andra Jr., and M. A. Magsig, 1999: Descending and non-descending tornadic vortex signatures detected by WSR-88Ds. *Wea. Forecasting*, **14**, 625–639.
- Wakimoto, R. M., and J. W. Wilson, 1989: Non-supercell tornadoes. *Mon. Wea. Rev.*, **117**, 1113–1140.
- Wakimoto, R. M., H. V. Murphey, C. A. Davis, and N. T. Atkins, 2006b: High winds generated by bow echoes. Part II: The relationship between the mesovortices and damaging straight-line winds. *Mon. Wea. Rev.*, **134**, 2813–2829.
- WDTB, 2016: Azimuthal Shear. Accessed 15 September 2016. [Available online at <http://www.wdtb.noaa.gov/courses/MRMS/ProductGuide/SevereWeather/azimuthal-shear.php>]
- Weisman, M.L., 1992: The role of convectively generated rear-inflow jets in the evolution of long-lived mesoconvective systems. *J. Atmos. Sci.*, **49**, 1826–1847.
- Weisman, M. L., 1993: The genesis of severe, long-lived bow echoes. *J. Atmos. Sci.*, **50**, 645–670.

- Weisman, M.L. and C.A. Davis, 1998: Mechanisms for the generation of mesoscale vortices within quasi-linear convective systems. *J. Atmos. Sci.*, **55**, 2603–2622.
- Weisman, M. L., and R. J. Trapp, 2003: Low-level mesovortices within squall lines and bow echoes. Part I: Overview and dependence on environmental shear. *Mon. Wea. Rev.*, **131**, 2779–2803.
- Wheatley, D. M., D. J. Stensrud, D. C. Dowell, and N. Yussouf, 2012: Application of a WRF mesoscale data assimilation system to springtime severe weather events 2007–09. *Mon. Wea. Rev.*, **140**, 1539–1557.
- Xu, X., Xue, M., and Wang, Y., 2015b. The genesis of mesovortices within a real-data simulation of a bow echo system. *J. Atmos. Sci.*, **72**, 1963–1986.